QUANTUM ADVANCES IN IMAGING SYSTEMS

A Dissertation

by

Hashir Puthiyapurayil Kuniyil

Submitted to the
Graduate School of Sciences and Engineering
In Partial Fulfillment of the Requirements for
the Degree of

Doctor of Philosophy

in the
Department of Electrical and Electronics Engineering

Özyeğin University
March 2023

QUANTUM ADVANCES IN IMAGING SYSTEMS

Approved by:

Asst. Professor Kadir Durak, Advisor
Department of Electrical and
Electronics Engineering
Özyeğin University

Professor Özgür Müstecaplıoğlu
Department of Physics
Koç University

Asst. Professor Ahmed Akgiray
Department of Electrical and
Electronics Engineering
Özyeğin University

Asst. Professor Mehmet Parlak
Department of Electrical and
Electronics Engineering
Özyeğin University

Date Approved: 06 March 2023

Professor Alper Kiraz
Department of Physics, Department of
Electrical and Electronics Engineering
Koç University

This thesis is devoted to my beloved late grandmother, Ummachu.

ABSTRACT

Quantum mechanics-based systems are increasingly used for advancing existing technologies. One of the technological frontiers where features of quantum mechanics are shown to have high potential is the imaging industry. Quantum imaging, a quantum version of the conventional imaging system, is becoming increasingly explored for imaging applications. This method of imaging involves taking advantage of unique spatial and temporal quantum correlations to enhance its figure of merit, including modulation transfer function. This thesis discusses the implementation procedure of the photonic quantum imaging scheme with the principal aim of achieving an improved imaging system. In this direction, the efficient generation of quantum sources, as well as their distribution and accurate analysis, are of paramount importance, particularly regarding the practicability of many quantum imaging applications. A quantum source based on the nonlinear process of spontaneous parametric down-conversion (SPDC) is well-known and increasingly used for this task. We theoretically study the suitability of the critically phasematched SPDC process and a detailed analysis of it is given in this thesis that will help in engineering a quantum source that is fit for quantum imaging applications. From our theoretical studies and basic experiments, it is well understood that the photon pairs called signal and idler from an SPDC process are capable of showing entanglement time and position correlation-suitable parameters for quantum imaging. These temporal and spatial correlations are used for quantum imaging where spatial correlation supports the extraction of the complete 2D features of the sample under study and the temporal correlation allows us to enhance the SNR of the system, a parameter that affects the modulation transfer function. To learn the temporal correlation's capability to suppress the noise, hence

enhanced SNR, a separate work that is based on the quantum illumination experiment driven by continuous wave laser pumped SPDC is conducted. Our results show that a quantum correlation in the time domain has increased resilience to noise. In a novel method, we demonstrate that with the assistance of polarisation correlation, we can further improve the performance metric of SNR of a quantum illumination system. As we use temporal correlation in the imaging scheme in addition to the spatial correlation, this result has implications for suppressing noise from a quantum imaging system.

The advancement of camera technologies offered ample room for experimenting with quantum spatial features, especially in SPDC-based spatial correlation-based imaging. The spatial correlation in SPDC stands out from classical systems- as this showed EPR-type correlations. The task of achieving reconstruction of the spatial feature of an object sample with the assistance of SPDC's spatial quantum correlation has been shown in this thesis. Our study exploited the transverse spatial correlation in the continuous basis of the SPDC mode to the realization of 2D quantum imaging. Our proof of concept experimental result proves that spatial correlation can be used for reconstructing an image. As this imaging scheme is based on the quantum-correlation behavior of signal and idler photons of the SPDC process, we could suppress the noise in the system by employing the coincidence imaging technique. The demonstrated experimental imaging method is diffraction limited, thus the resolution of the system, at best, is equal to the classical counterparts. Our simulation work shows the performance of the quantum imaging scheme can be affected by input parameters such as the pump beam waist, crystal length, and location of the sample object and the imaging instrument. Therefore, carefully selecting the input parameter values is critical for the system's performance. The study concludes that quantum-based imaging schemes, like the one presented in this thesis, have high resilience to noise.

ÖZETÇE

Kuantum mekaniği temelli sistemler, mevcut teknolojilerin ilerletilmesinde giderek daha fazla kullanılmaktadır. Kuantum mekaniği özelliklerinin yüksek potansiyele sahip olduğu teknolojik sınırlardan biri de görüntüleme endüstrisidir. Görüntüleme uygulamaları için giderek daha fazla araştırılan kuantum görüntüleme, geleneksel görüntüleme sistemlerinin bir kuantum versiyonudur. Bu görüntüleme yöntemi, benzersiz uzamsal ve zamansal kuantum korelasyonlarından faydalanarak, modülasyon transfer fonksiyonu dahil olmak üzere parametrelerini geliştirmek için kullanılır. Bu tez, geliştirilmiş bir görüntüleme sistemi elde etmek için fotonik kuantum görüntüleme düzeninin uygulanma prosedürünü tartışmaktadır. Bu yönde, kuantum görüntüleme uygulamalarının pratikliği bakımından özellikle kuantum kaynaklarının verimli bir şekilde oluşturulması, dağıtımı ve doğru bir şekilde analiz edilmesi büyük önem taşımaktadır. Kendiliğinden parametrik aşağı dönüşüm (KPAD) oluşumunun kritik faz eşleşmesine dayalı bir kuantum kaynağı, bu görev için iyi bilinen ve giderek daha fazla kullanılan bir kaynaktır. Bu tezde, kritik faz eşleşmesi KPAD işleminin uygunluğunu teorik olarak inceledik ve bir kuantum kaynağı mühendisliği için ayrıntılı bir analiz sunduk. Teorik çalışmalarımız ve temel deneylerimizden, KPAD işleminden elde edilen sinyal ve aylak adlı foton çiftlerinin, kuantum görüntüleme için uygun olan zamansal ve mekansal korelasyonları gösterebildiği iyi anlaşılmaktadır. Bu zamansal ve mekansal korelasyonlar, örnek üzerindeki tam iki boyutlu özelliklerinin çıkarılmasını destekleyen uzamsal korelasyonları ve sistemdeki SNR'yi artırmamıza izin veren zamansal korelasyonları içerir. Gürültüyü bastırmak için zamansal korelasyonun yeteneğini öğrenmek, böylelikle SNR artışı, sürekli dalga lazerle pompalanan KPAD tarafından yönlendirilen kuantum aydınlatma deneyine dayanan ayrı

bir çalışma yürütülmüştür. Sonuçlarımız, zamansal korelasyonun gürültüye karşı artan dayanıklılığının olduğunu göstermektedir.

Kamera teknolojilerinin gelişimi, özellikle KPAD temelli mekansal korelasyon tabanlı görüntüleme alanında kuantum mekaniği mekansal özellikleriyle deney yapmak için bol fırsat sunmuştur. KPAD'deki mekansal korelasyon klasik sistemlerden ayrılır - çünkü EPR tipi korelasyonlar gösterir. KPAD'nin mekansal kuantum korelasyonunun yardımıyla bir nesne örneğinin mekansal özelliğinin yeniden oluşturulması görevi bu tezde gösterilmiştir. Çalışmamız, KPAD modunun sürekli bazında popüler bir çapraz mekansal korelasyon özelliğini kullanarak iki boyutlu kuantum görüntüleme gerçekleştirmeye yöneliktir. Kavram kanıtı olarak deneysel sonuçlarımız, mekansal korelasyonun bir görüntüyü yeniden oluşturmak için kullanılabileceğini göstermektedir. Bu görüntüleme şeması, KPAD sürecinin sinyal ve aylak fotonlarının kuantum korelasyon davranışına dayandığı için, rastlantısal görüntüleme tekniğini kullanarak sistemdeki gürültüyü bastırabildik. Gösterilen deneysel görüntüleme yöntemi kırınım ile sınırlıdır, bu nedenle sistem çözünürlüğü en iyi durumda klasik karşıt parçalarıyla eşittir. Simülasyon çalışmamız, kuantum görüntüleme şemasının pompa ışını bel genişliği, kristal uzunluğu, örnek nesnenin konumu ve görüntüleme aracının konumu gibi girdi parametreleri tarafından etkilenebileceğini göstermektedir. Bu nedenle, giriş parametre değerlerinin dikkatli seçimi sistem performansı için kritiktir. Çalışma, bu tezde sunulan gibi kuantum tabanlı görüntüleme şemalarının gürültüye karşı yüksek direnç gösterdiğini sonuçlandırmaktadır.

ACKNOWLEDGEMENTS

I am deeply indebted to my supervisor Prof. Dr. Kadir Durak for the energy and time he spend on the progress of my research and without that I could not have carried out this work. His ability to explain complex scientific concepts in a simple manner is admirable, and it has helped me to work on the research of giants in the field. Moreover, his unrelenting encouragement during difficult times is a quality that I aspire to emulate in my future endeavors.

I feel fortunate to have had the opportunity to interact with each member of the lab and engage in discussions on life and science. I want to acknowledge Alper Ozulker, Helin Ozal, Mehmet Oncu, Melis Pahali, Muhammet Demirkıran, and Muhammed Yamin. I have been fortunate to work with Helin Özel. She has helped me to conduct the quantum illumination experiment. Our mutual hard work during the Covid-19 peak time was instrumental to publish my second paper. I had been enjoying discussing science with Mehmet Oncu. The productive discussions with Mehmet helped solidify complex physics concepts. Additionally, I am grateful for Mehmet's emotional and physical support during the Covid-19 period in my life. I met my closest friend, Shewit Tesfay, while studying at Özyeğin University. Our conversations have spanned a wide range of topics, and his insights have had a significant impact on my decisions throughout my Ph.D. studies. I would like to take this opportunity to express my appreciation for the insightful discussions I had with Alper Ozulker regarding electronics-related work. His knowledge and expertise in the field have been instrumental in guiding my understanding and approach towards this subject.

I extend my heartfelt appreciation to my Ph.D. jury members, Prof. Dr. Kadir Durak, Prof. Dr. Alper Kiraz, Prof. Dr. Ahmet Akgiray, Prof. Dr. Özgür Müstecaplıoğlu, and Prof. Dr. Mehmet Parlak, for unconditionally giving their energy and time for the sake of science. Prof. Dr. Kadir Durak, Prof. Dr. Alper Kiraz, and Prof. Dr. Ahmet Akgiray, as members of my thesis monitoring committee, have always been supportive.

I would like to express my love and gratitude to my parents, Muhammed and Rabiya, and siblings, Jasir, Yasira, and Fasir, for showing compassion during this difficult time in my life. Finally, I thank my wife Raslath for her support and love and for being on my side always and understanding. I thank my son Zain for showing me a different life that I am unfamiliar with.

During my Ph.D. journey, there were many individuals who played a role in shaping who I am today, and I am grateful to them all.

The research work presented in this thesis was backed by the Scientific and Technological Research Council of Turkey (TUBITAK) through project numbers 118E156 and 118E991.

0.1 Auther's published works

1. **Kuniyil H**, Ozel H, Yılmaz H, Durak K. Noise-tolerant object detection and ranging using quantum correlations. Journal of Optics. 2022 Aug 15.

2. **Kuniyil H**, Durak K. Efficient coupling of down-converted photon pairs into single mode fiber. Optics Communications. 2021 Aug 15;493:127038.

3. **Kuniyil H**, Durak K. Effect of phase and spatial distinguishability of photon pairs on the entanglement fidelity. In Photonics for Quantum 2021 2021 Jul 11 (Vol. 11844, p. 118440W). SPIE.

4. **Kuniyil H**, Jam N, Durak K. Object ranging and sensing by temporal cross-correlation measurement. In SPIE Future Sensing Technologies 2020 Nov 8 (Vol. 11525, pp. 150-156). SPIE.

5. **Kuniyil H**, Durak K. Down-Conversion Emission Profile characterisation via Camera. In Laser Science 2020 Sep 14 (pp. JM6A-21). Optical Society of America.

0.2 Author's works under preparation

1. **Kuniyil H**, Durak K. Optimization of coincidence window for QKD in a noisy environment

2. Mohsen Izadyari, **Kuniyil H**, Kadir Durak, and Özgür E. Müstecaplıoğlu. Atom-field interaction in a sub-diffraction hollow shape trap

3. Kadir Durak, Alper Özülker, **Kuniyil H**, Mehmet parlak. Improving Count Rate Linearity of Geiger Mode Avalanche Photodiodes

TABLE OF CONTENTS

DEDICATION . . . . **iii**

ABSTRACT . . . . **iv**

ÖZETÇE . . . . **vi**

ACKNOWLEDGEMENTS . . . . **viii**

0.1 Auther's published works x

0.2 Author's works under preparation x

LIST OF TABLES . . . . **xiv**

LIST OF FIGURES . . . . **xv**

I INTRODUCTION **1**

1.1 Quantum imaging 3

1.2 Resolution and signal to noise ratio 3

1.3 2D reconstruction of the image 7

II LITERATURE ON QUANTUM IMAGING SYSTEM **11**

III THEORY OF SPONTANEOUS PARAMETRIC DOWNCONVERSION **18**

3.1 Spontaneous parametric down conversion 18

3.2 Engineering the SPDC parameters 20

3.2.1 Determining wavelength values 22

3.2.2 Phasematching angle calculation 22

3.3 Spatial profile of the downconverted photons 25

3.3.1 SPDC beam profile in a collinear geometry 27

3.3.2 Crystal length on emission profile 28

3.3.3 Beam walk-off in spatial profile due to birefringence 29

3.3.4 Experiment for beam profiling 31

3.3.5 Quantification of the Asymmetry 34

3.4 Quantum mechanical description 35

3.4.1 Single Mode Description 35
3.4.2 Multi Mode Description 41
3.5 Spectral properties of SPDC 44
IV SIGNAL TO NOISE RATIO IN A QUANTUM SYSTEM 47
4.1 Shot-noise 47
4.1.1 Shot-noise in a classical system 47
4.1.2 Shot-noise in a quantum system 49
4.2 SNR calculation in the presence of environmental noise 50
4.2.1 Theory of SNR calculation 50
4.2.2 Experimental comparison of classical and quantum SNR . . . 52
4.3 Polarization correlation for SNR enhancement 56
4.3.1 Experimental setup 56
4.3.2 Second order correlation function 58
4.3.3 SNR comparison for TC and TPC systems 60
4.4 Detector characteristics 62
4.4.1 Count rate dependent detector efficiency 62
4.4.2 Correcting detector deficiency 64
V CORRELATION BASED 2D QUANTUM IMAGING 69
5.1 Experimental setup and data processing 69
5.2 Analytical discussion of quantum imaging experiment 75
5.2.1 Simulating an object 76
5.2.2 Spatio-temporal correlation 79
5.2.3 Input parameters on spatio-temporal correlation 83
5.2.3.1 Effect of the Pump beam waist on spatial correlation 83
5.2.3.2 Effect of the axial position on spatial correlation . . 86
5.2.4 Image system's resolution 90
5.2.5 Camera resolution and image quality 94
5.2.6 Modulation Transfer Function analysis 96

VI CONCLUSIONS AND OUTLOOK **99**

VII ANCILLARY MATERIALS **102**

7.1 Python codes 102

7.1.1 Crystal cut angle calculation 102

7.1.2 SPDC mode and object creation 104

7.1.3 Processing ICCD data 107

7.2 Photographs 109

REFERENCES **112**

VITA **123**

LIST OF TABLES

1 Specifications of popular camera technologies used for quantum imaging. 10

2 SPDC classification by birefringence and state of polarization of each field. 22

3 Characteristic detector parameters of two detectors used in this study. 54

4 Features of Pi-Max3 camera. 72

LIST OF FIGURES

1.1 A typical near-field and diffraction-limited transmission imaging experiment close to the experimental quantum scheme explored in the paper. 4

1.2 Sketch of SPDC process where (a) pump laser enters into a specially designed nonlinear crystal (NLC) and generates the two lower frequency signal and idler photons (downconversion) (b) vector field diagram of interacting light fields when momentum conservation is satisfied (c) the vectors are distributed in components form to realize the transverse momentum elements. 7

1.3 Single vector field direction of signal and idler photons in a near field imaging configuration. The signal and idler photons pass through identical but opposite transverse directions and interact at a single point on the object that is under study. The object is marked with 'O' and L1, L2, L3, and L4 are lenses the scaling of the figure assumed focal lengths of L1 = L4 and L2 = L3. Dashed vertical lines indicate an image or Fourier planes. 9

3.1 A light beam having both ordinarily (o-polarized) and extraordinarily (e-polarized) polarization components propagates through a birefringence medium and experiences a split inside a nonlinear medium. The optic axis (O.A), angle of O.A with respect to o-beam propagation (θ_c), and walk-off angle, ρ, are indicated. (b) index ellipsoid showing the axis of refractive indices (ordinary refractive index-n_o, and extraordinary refractive index - n_e). (c) electric field 3D components. The propagation direction of the light beam is parallel to E_z, n_e is parallel to E_y and n_o is parallel with E_x. 20

3.2 Signal idler photons wavelengths dependence graph in a laser light of wavelength 405 nm pumped SPDC process. 23

3.3 Phasematching angle values for a type-I SPDC configuration versus various signal wavelengths. 24

3.4 Propagation direction of pump, signal, and idler photons in a (a) collinear geometry and (b) noncollinear geometry. 25

3.5 Quantification of phase mismatch (Δk) in different crystal cut angle for 405 nm $\Longrightarrow$ 780 nm + 842 nm pump signal and idler wavelengths combination. Phasematching angle 28.80° and their corresponding $\Delta k = 0$ are indicated. 26

3.6 Emission profile of the SPDC in a Type - I BBO crystal of length $L = 1$ mm. The emission angle ϕ distributed between $-0.01°$ to $0.01°$. . . . 27

3.7 Emission profile of the downconverted modes for a Type-I SPDC configuration seen 3 mm away from the nonlinear crystal of $L = 1$ mm (left) when the crystal cut angle is 28.80°, that is collinear, and (right) $28.8 + 0.05°$; noncollinear. 28

3.8 Crystal length dependence of emission profile of the SPDC. As the phase match decreases the efficiency also decreases and touched the efficiency value of zero when the Δk reaches $2/L$. 29

3.9 Schematic of the propagation direction of the pump, signal, and idler beam with various source characteristics indicated, (a) where k_p^o and k_p^e are ordinarily polarised and extraordinarily polarised pump wave vectors, respectively. The optic axis of the crystal is marked with 'c'. (b) The generated SPDC modes in three dimensions show SPDC annular mode. 32

3.10 Experimental scheme used for SPDC beam profiling. 32

3.11 Experimental (left) and the corresponding simulated (right) images of SPDC modes. Panel (a), (b) and (c) are the typical asymmetrical profile of the SPDC emission for crystal length values of 10 mm, 6 mm, and 4 mm, respectively. Given SPDC modes have 1.5° emission angle. 33

3.12 (a) Asymmetry value for crystal length as a varying SPDC parameter. The error value is ±0.1 in the y-axis. (b) Asymmetry of SPDC photons for different pump beam waist. The data points with triangle, diamond, and circle shapes correspond to the pump beam waist of 118 μm, 78.6 μm, and 47.2 μm, respectively. The solid line is the theoretical fit using equations 3.18 and 3.19. The propagation of error is calculated to be 0.046 on the y-axis. 34

3.13 Spectral distribution for signal and idler photons when the length of the crystals are 1 mm, 4 mm, and 10 mm. FWHM values are 30 nm, 10nm, and 4 nm. The central frequency of the signal and idler are 780 nm and 842 nm when the pump wavelength is 405 nm at crystal phasematching angle 28.80°. 44

3.14 Emission angle and wavelength spectrum of signal and idler. Central wavelengths of signal and idler are indicated by the dashed vertical line. The highest intensity of signal and idler are seen when the emission angle is 0°. 45

4.1 Photons' Poisson statistics 49

4.2 Photon fluctuation in different time realization. 51

4.3 The theoretical SNR comparison for coincidence measurement (red solid line) and direct classical system. 53

4.4 Schematic of the experimental setup for comparing classical and quantum SNRs. . . . 54

4.5 Experimental SNR values of classical direct detection and quantum coincidence detection schemes in various noise values. 55

4.6 The experimental arrangement used for testing the detection schemes that use (a) time and polarization correlations and (b) only time correlations. BBO: beta barium borate, LF: long-pass filter, DM: dichroic mirror, PBS: polarizing beam splitter, QWP: quarter wave plate, BS: beam splitter, APD1-2: avalanche photo-detector 1-2. 56

4.7 The $g^{(2)}$ distribution over a range of temporal displacement for 63 ms data for each with no noise scenario. 59

4.8 The measured signal-to-noise ratio (SNR) versus the injected noise N_b is plotted for time correlation (TC) (blue dots) and time and polarization correlation (TPC) (red dots) schemes. The theoretical fit (solid lines) is made by using equation 2. The $g^{(2)}$ trend for different noise conditions for both TPC and TC are shown in the inset. 61

4.9 Photon count rate versus the input photon rate. Red dots are experimentally-obtained photon count rate at the detector. A power meter value converted into photon number gives rise to the input photons count. . . 63

4.10 The correction factor versus the incident photon rate. 64

4.11 (a) Coincidence value showing a sinusoidal trend while rotating the quarter wave plate, which effectively controls the amount of detected signal that is reflected from the object. This behavior is observed only from the polarized signal photons (since the noise is unpolarized). The increased level of noise rises the floor height of the sinusoidal plots (minimum coincidence value is not zero). Therefore, floor height gives rise to the estimation of accidental coincidence. The error bars are obtained by assuming the photon fluctuates by $\sqrt{N}$. Solid lines represent theoretical fit. (b) Derivative of (a) with respect to ϕ. . . . 65

4.12 Demonstrating the variation of visibility with respect to the average noise (red). The accidental coincidence increases linearly with the external noise (blue). Points represent the experimental data and the solid lines represent the theoretical fit using the equation 4.11. Error bars in the accidental coincidence are the order of $\sqrt{N}$. The error in the visibility is calculated by following the standard error propagation method. 67

5.1 Experimental setup used for correlation-based quantum imaging. . . . 70

5.2 Quantum efficiency of the ICCD camera used for this study. The ICCD camera is designed for RB fast gated operation. 73

5.3 The image of the sample under (a) noise-free classical imaging (b) noisy classical imaging (c) noisy imaging with quantum correlation method for the same sample. 74

5.4 (a) SPDC profile at the object location the width and height are equal and (b) the Gaussian profile of the SPDC with $1/e^2$ value of 0.540 mm. 76

5.5 Negative evenly spaced 3-slit target. The width of the dark line and the bright line is 25 um. 79

5.6 Longitudinal and transverse propagation vectors of signal and idler photons. 80

5.7 Spectral correlation of signal and idler photons in the transverse plane. 81

5.8 Nonnormalized spatio-temporal first-order correlation (left) and non-normalized spatio-temporal second-order correlation (right). 83

5.9 The temporal (left) and spatial (right) correlations profile of signal and idler photons. The 1/e width of each are indicated on the plot. 84

5.10 Conditional probability of finding the signal photons provided $\rho_i = 0$. Two sets of pump beam values are used in plotting equation 5.17. . . 86

5.11 Position correlation of the signal and idler at the y coordinate. The left to right takes different z values in increasing order as indicated in each figure. The dotted circle indicates the region where SPDC photons will fall on. The horizontal and vertical intersecting point is the center of the circle. 87

5.12 The position uncertainty as z goes from 0 $\rightarrow\infty$. 88

5.13 The signal and idler field at the momentum anticorrelation (which means when the signal is at (x_s, y_s) idler is at $(-x_i, -y_i)$ in a complex plane) positions seen at the image plane (z = 0) when crystal length is 4 mm and corresponding $\sigma_0 = 10.8\ \mu m$ at a single event. 89

5.14 2D coincidence plot where the heat map shows high density for maximum signal idler coincidence. This depicts the fact that observing the idler photons at the anti-momentum correlation location of the signal photons. This plot is referred to as the intensity correlation matrix. 90

5.15 The direct detection classical image appeared on the imaging system when the resolution is 11.6 um and noise is null(b) the image of classical noise system seen on the camera. analytically we can think SNR = 1. (c) The direct detection classical image appeared on the imaging system when the resolution is 0.5 um and noise is null. 92

5.16 Images from the microscopy system where the camera resolutions are (a) 13 um and (b) 26 um. Again, the width of bright and dark lines is 25 um each. Therefore, the camera with 26 um spatial resolution cannot resolve the 25 um samples according to the Nysguist theorem (see text). 95

5.17 The contrast comparison at object and image planes. 97

5.18 MTF of the classical and quantum imaging systems in a noisy environment. 98

7.1 Negative and positive evenly spaced objects 107

7.2 A 405 nm pump photon illuminating two BBO crystals. 109

7.3 Experimental setup for noise to investigate the noise-embedded object detection. 110

7.4 Experimental setup for quantum imaging. 110

7.5 Image of a tweezer object seen under the microscope. 111

CHAPTER I

INTRODUCTION

The 20th century witnessed a scientific revolution in quantum mechanics. The first quantum revolution involved solving fundamental phenomena, mainly blackbody radiation and the photoelectric effect that classical mechanics failed to address. This led to redefining atomic theories and other subnanometer scale phenomena through the use of quantum mechanical building blocks. Quantum mechanics assumes the subnanometer scale systems have physical parameters that are fundamentally discrete in nature. That directs us to assume a light has a minimum energy value scale, later called photons. This creates a dilemma on how we should treat light- should we treat light as a particle or a wave? From Young's double slit experiment, it is well understood that light exhibits wave properties. Interestingly, it is found that light even at a single photon level shows Young's double slit diffraction pattern that is understood otherwise only by wave properties [1, 2, 3], then after called wave-particle duality [4]. In 1926 Schrodinger put forward mathematical formulations, called Schrodinger wave equations, that can describe the quantum principles by statistical probabilities [5]. Inspired by Schrodinger's work Max Born formulated the statistical picture of quantum mechanics, with that, we understand that a quantum particle has no reality described as quantum nonreality until a measurement is performed [6]. This unique property of the quantum system is called quantum superposition.

Another quantum mechanical surprise came in 1935 when Einstein, Podolsky, and Rosen (EPR) published a seminal work that suggested a counter-intuitive phenomenon called quantum entanglement [7]. Quantum entanglement is an exceptional correlation between two quantum particles that, in principle, show a space-independent correlation, referred to as nonlocality. The entanglement correlation is strong enough that a measurement done on one of the entangled twins can immediately influence the other to have a corresponding change. This breaks one of the principles of the special theory of relativity which says nothing can travel faster than the speed of light. Therefore, EPR concluded that quantum mechanics is incomplete and they contemplated there is a hidden variable that dictates how to behave in entanglement systems. In this wake, in 1964, John Bell proposed a theoretical method that can show if a hidden variable is playing in entangled systems [8]. Bell's results were not favorable to the hidden variable model and it rejected the EPR model. Later in 1969 experimental evidence by John Clauser, Michael Horne, Abner Shimony, and Richard Holt (shortly CHSH) [9] confirmed there is no hidden variable underplay for quantum entanglement and inspired to think quantum mechanics is complete and quantum particles behave differently than classical systems. However, the experimental nonidealities of the CHSH's principle are insufficient to conclude if EPR was wrong. In 1976 Alain Aspect proposed a loophole-free experimental setup to test the EPR paradox [10]- finalizing EPR's claim is actually not true.

Presently, Copenhagen's interpretation [11] of quantum mechanics is widely accepted by many due to its experimentally supportive results. The experimental works on foundational quantum theories open up new frontiers that can be beneficial in technological advancement that includes quantum computing [12, 13], quantum cryptography [14, 15, 16, 17, 18, 19, 20], quantum sensing [21, 22], quantum imaging [23, 22, 24, 25, 26, 27, 28, 29, 30, 31, 32, 33], and quantum mechanics based LIDAR/RADAR [34, 35, 36, 37, 38]. The advancement of quantum imaging technology is the basis of the work presented here.

1.1 Quantum imaging

Quantum imaging is a broad term that encompasses a wide range of imaging techniques including quantum ghost imaging, intensity correlation-based imaging, biphoton imaging for deviating Raleigh limit [39], quantum distillation [31], and quantum imaging with undetected photons [32, 33]. These systems, in some cases, aim to beat the limitation imposed by the classical systems such as the shot-noise and diffraction limits. In other schemes, the quantum imaging scheme proposes a new way of imaging that benefits from low photon number detection and efficiently eliminate environmental noise from the system [25, 26] by exploiting quantum principles.

The concept of imaging can be broadly divided into two. Firstly, imaging of an object that is far from the detection systems such as telescope-based imaging of an object. In the second type, the test subject is placed close to the illumination and detection systems, called the microscopic study of a sample (this instrument is called the microscope). For the latter one, the research is mostly carried out hoping to improve the resolving power of the microscope thereby smaller information about the test subject can be obtained. Also, in the microscope, the highest SNR is desirable. These two factors encompass the contrast of the image. In this work, we look at imaging a sample that is placed close to the objective lens. Therefore, the system discussed in this work falls under the microscopy imaging scheme. The work exploited the spontaneous parametric downconversion(SPDC) process [40, 41, 42, 43, 44, 45] for achieving a quantum source of light.

1.2 Resolution and signal to noise ratio

The diffraction limit is a fundamental constraint that sets the maximum resolving power achievable by an imaging system. The factors that impact the resolving power of such a system are well-known- primarily the optical properties of the imaging apparatus and wavelength of the illuminating source influence the resolving power of the system. The resolving power of a coherent source-driven and diffraction-limited classical imaging system can be defined as

$$\text{Resolving Power} = \frac{1.66\lambda}{2NA} \tag{1.1}$$

where λ is the wavelength of the illuminating light source, and NA stands for the numerical aperture of the objective and condenser lenses used in the microscope. Mostly, the optical properties of the condenser and objective lenses are identical. A simple microscope imaging experimental setup is shown in figure 1.1. In the figure, the NA can be computed by $NA = n \times sin(\theta)$ where n is the refractive index of the medium (in figure 1.1 "n" is the refractive index of the region between the condenser and objective lenses), following the geometry the NA can be modified into $NA = n \times sin(tan^{-1}D/2f) \sim D/2f$. Clearly, the focal length and light beam aperture are defining the resolving power: smaller focal lengths and large light beam aperture, and short wavelength light sources are recommended for high resolving capability.

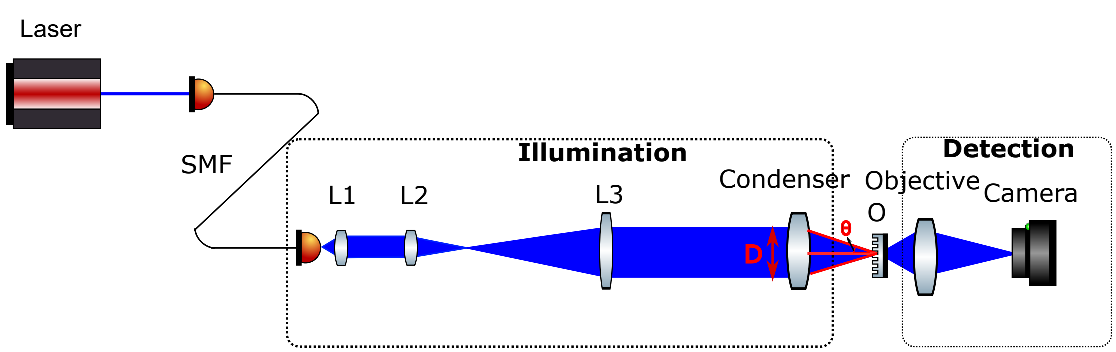

Figure 1.1: A typical near-field and diffraction-limited transmission imaging experiment close to the experimental quantum scheme explored in the paper.

An image is formed by etching off the light field's spatial region by the test subject depending upon its transmission/absorption properties. The object sample forms an intensity gradient of the light at the imaging sensor to reconstruct the shape of the object. If the axial component of light is not involved, the formed image will be the

2D structure of the object. In that case, only the transverse vector field of light is used. Equation 1.1 gives the resolution in the transverse field. Two pinholes of small diameter as a test sample which is placed in the object plane of the microscope as in figure 1.1 can efficiently model for understanding resolving power in an imaging system. When the light rays pass through these two pin-holes, depending upon the size of the pinhole an interference pattern will be formed on the image plane (in figure 1.1, the image plane is the camera sensor plane). If two holes are far apart we can easily resolve the two holes at the image plane. However, if the two holes are close to each other such that the radius of the diffraction pattern formed by pinhole-1 and pinhole-2 are less than the resolving power of the imaging system, we cannot resolve the pinholes. If two diffraction pattern is separated by the radius of the diffraction pattern we can just resolve two pinholes. This point where we can just resolve two pinholes at the imaging plane is defined by the Raleigh criterion. The radius of the diffraction pattern formed by pinholes is again defined by equation 1.1. Thus, equation 1.1 gives the Raleigh limit of the system. The imaging system discussed in this work is diffraction limited, thus following the Raleigh formulation. We will see that the resolving power of the quantum imaging presented here at best can achieve Raleigh's resolution and this is only when the quantum system operates in a special regime defined by the transverse spatial correlation of the quantum correlation.

The noise from the illuminating source and environment (background noise) can affect the performance of the imaging system, the performance of the system can be learned by the metric of signal-to-noise ratio (SNR). As a matter of fact, any light source has a fluctuation of photons about its mean value called shot noise. The shot noise is inherent in any system which has a quantum mechanical origin: quantum vacuum fluctuation. In classical methods, the smallest achievable value of shot noise is defined by the variance of the noise fluctuation of the source, which can be quantified by the shot noise performance metric $\sigma =< \delta^2 S > / < S >$ where $< \delta^2 S >$ is the variance of the source S and $< S >$ is the average photon number. Classical systems can show $\sigma = 1$ at best and, is achieved by correlation measurement method of the coherent source-based detection. In a typical case, σ is very high which is of the order of a few hundred. The EPR-type correlation found in the spatio-temporal domain produced by the parametric process can demonstrate sub-SNL imaging. This system is very efficient that, in theory, we can achieve a zero SNL value (ideal case) that will show high-contrast images [24]. Achieving experimental sub-SNL imaging is difficult in experimental settings as it requires zero environmental noise and a very low dark count in the detection instrument used. Furthermore, the same contrast can be achieved by simply increasing the intensity of the illuminating beam in a classical system. From a practical point of view, the temporal correlation present in the parametric process can be used as an efficient way to suppress environmental noise. In a quantum-based imaging scheme, the noise can be reduced by signal and idler photons (entangled pair photons) high temporal correlation and therefore achieve a high SNR that is defined as

$$SNR = \frac{C(\tau)}{\sqrt{N_s(N_i + N_{env})\Delta t T}} \tag{1.2}$$

where $C(\tau)$ is the magnitude of the signal and idler coincidence, N_s is the singles of signal photons and idler photons, respectively, N_{env} is the number of environmental noise photons entered in the detection system, τ is the resolution of the coincidence detection, Δt is the coincidence window and T is the integration time. Although a pulsed laser-involved imaging scheme can provide a temporal correlation of this kind the simultaneous time and spatial correlation, called Spatio-temporal correlation makes the quantum imaging method a more robust system. In this work, I will separately test the temporal correlation of the entangled pairs generated in a parametric down-conversion process by using a single-pixel camera (single photon detector) and verify the equation 1.2.

1.3 2D reconstruction of the image

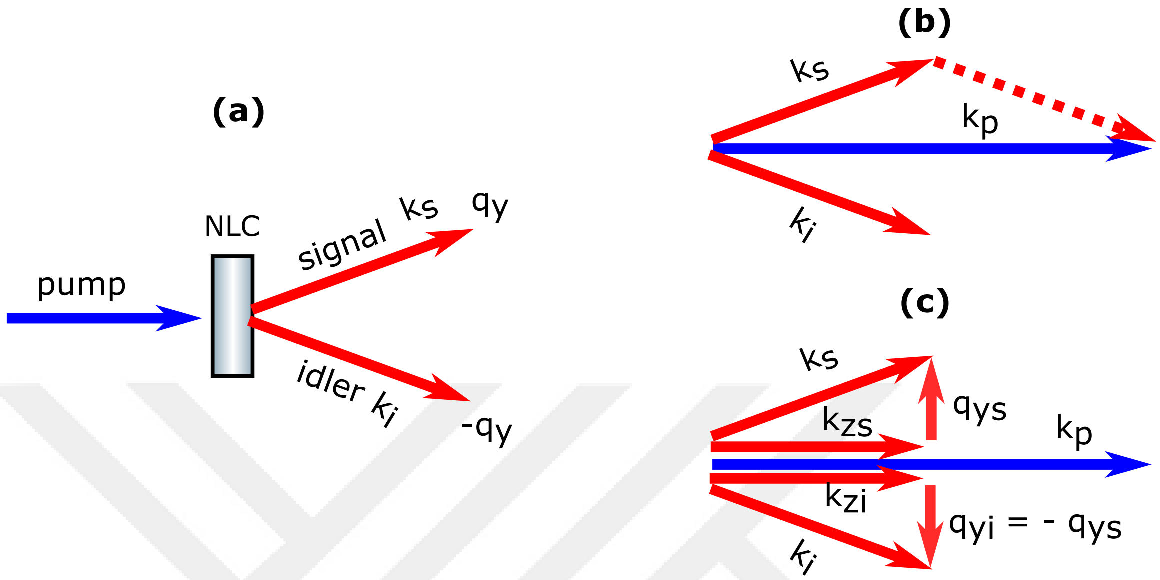

Figure 1.2: Sketch of SPDC process where (a) pump laser enters into a specially designed nonlinear crystal (NLC) and generates the two lower frequency signal and idler photons (downconversion) (b) vector field diagram of interacting light fields when momentum conservation is satisfied (c) the vectors are distributed in components form to realize the transverse momentum elements.

The momentum conservation of the SPDC fields translates into a phase-matching wave vector (denoted by k) which possesses a definite path. In figure 1.2, the k-vectors of three interacting fields have been shown. In the SPDC, a pump beam having high-frequency light converts into two lower frequency light signals arbitrarily called signal and idler photons after passing it through a specially designated nonlinear crystal. One of the basic criteria for the SPDC is the momentum conservation and that can be mathematically written in the momentum balanced form as $\hbar k_p = \hbar k_s + \hbar k_i \rightarrow k_p = k_s + k_i$. Figure 1.2 (b) shows the k-vector field directions of the pump signal and idler fields respecting momentum conservation. In this work, a 2D reconstruction of the object is sought, therefore I utilized only transverse momentum components. To make it a suitable form, the k-vectors of downconverted photons can be written into transverse momentum components as $k_{s(i)} = \sqrt{k^2_{s(i)z} + q^2_{s(i)x} + q^2_{s(i)y}}$.

The letter 'q' represents the transverse wave vectors. Figure 1.2 (c) shows the 3D coordinate components of the downconverted fields (the figure does not show transverse x-components for simplicity). As shown in the figure, when a transverse momentum experienced is q_{sy} we can expect its twin pair's (idler photons) momentum as $-q_{sy}$. This is called momentum anti-correlation as the sign of the signal and idler transverse momentum are opposite. Since we are interested in position correlation (due to near-field setup) rather than momentum one, the transverse momentum vectors should be converted into position variables. As the momentum and the positions are canonically conjugated pairs, mathematically, applying a Fourier transformation on the momentum variable, $\hbar k$, will yield the position vector information ie. $\hat{f}(q) \rightarrow f(x)$. Incidentally, the plane where momentum anti-correlation is observed is called the Fourier plane, and the plane where position correlation is observed is called the image plane. This summarises that when a signal is observed at the position location 'r' the idler photon must be at 'r' itself, where $r = \{x, y\}$. In Optics, the Fourier transformation can be performed by using lenses. Figure 1.3 shows the image ($f(x)$)and Fourier planes ($\hat{f}(x)$). Lenses are used to switch the image and Fourier planes. Therefore, the NLC's plane projected on the object plane by using a lens system (refer to figure 1.3) will have the position correlation. That means the signal and its twin idler will interact at a single space point on the object. Effectively, we have two identical light rays coming out of a single point. This gives an opportunity to separate one of the twin pairs to copy the image field by intensity correlation, and achieve a full image via photon number correlation measurement. As all signal photons have a reference idler photon even if the noise is high, with the help of reference photons, we can obtain a noise-reduced (high SNR)image. This is done by incorporating temporal correlation in addition to spatial correlation (commonly called spatiotemporal correlation).

As the spatiotemporal correlation of the signal and idler photons generated in the

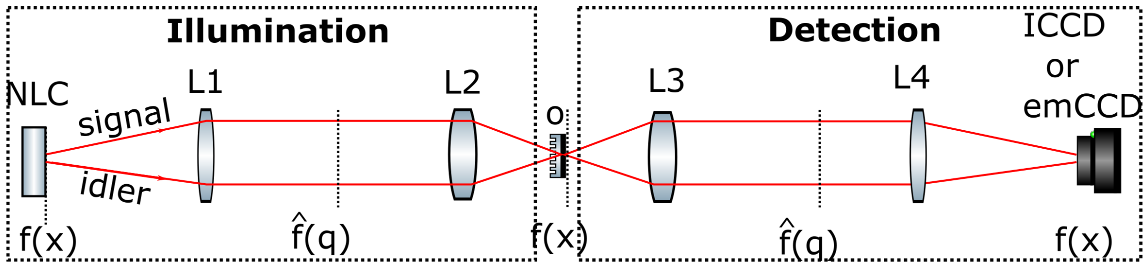

Figure 1.3: Single vector field direction of signal and idler photons in a near field imaging configuration. The signal and idler photons pass through identical but opposite transverse directions and interact at a single point on the object that is under study. The object is marked with 'O' and L1, L2, L3, and L4 are lenses the scaling of the figure assumed focal lengths of L1 = L4 and L2 = L3. Dashed vertical lines indicate an image or Fourier planes.

SPDC process is a source of the quantum imaging scheme presented here a single photon-sensitive spatial and time-resolving system is inevitable for the experimental demonstration. The spatial correlation of this kind was historically learned by scanning a single-pixel camera over a transverse spatial region of the field [23]. This is an inefficient method that yields only 3% quantum efficiency or lower. Plus, the method involves a long experimental duration. An advanced version of this kind is using a bundle of single photon sensors to collect spatial features, but that method has limited spatial mode [46]. After the advancement of camera technologies, presently, most of the quantum imaging research is carried out by using single photon sensitive spatial and temporal resolving cameras. Mostly used camera technology for quantum imaging are charge-coupled devices (CCD) and their modified versions such as intensified CCD (ICCD), electron multiplied CCD (EMCCD), and very recently, combined versions of both ICCD and EMCCD called EMICCD.

Since the CCDs are not single photon efficient, one needs to use the ICCD or EMCCD version of it for quantum imaging applications. Depending upon the type of imaging scheme we explore one can decide if EMCCD or ICCD is the best choice.

Table 1: Specifications of popular camera technologies used for quantum imaging.

Feature	**Ideal value**	**CCD**	**EMCCD**	**ICCD**
Quantum efficiency	100 %	95%	95%	50%
Readout noise	0	10	60	20
Gain	1	1	1000	1000
Spurious noise	0	0.05	0.005	0
Dark noise	0	0.001	0.001	0.001
Frame rate	-	-	26 fps (1024×1024 pixels)	26 fps (1024×1024 pixels)
Noise factor	1	1	1.41	1.6
pixel size	-	13 um	13 um	12.8 um

While EMCCDs can achieve near-ideal quantum efficiency the ICCD lacks good quantum efficiency; which shows only ~50% quantum efficiency even with an advanced Gen III intensifier installed model. Table 1 lists out important specifications of three versions of CCD cameras. As seen in the table, ICCD has limited quantum efficiency. However, the ICCD can operate in a fast external triggering mode and achieve picosecond timing resolution- a very promising feature. Therefore, ICCD is the best choice in synchronized operations-based quantum imaging such as quantum ghost imaging and sub-SNL imaging with the quantum source of light. Also, the spurious noise is very low for ICCD cameras as compared to the EMCCDs where impact ionization can boost the noise. Therefore, with ICCD we can increase the gain without much problem. On the other hand, in our kind of detection scheme where individual photon-photon correlation is estimated independently, the EMCCDs are recommended. It is because the quantum efficiencies of EMCCDs are high and the total noise factor is less compared to the ICCD camera. However, this work has used the ICCD camera for experimental demonstration of quantum imaging as it is available in the lab.

CHAPTER II

LITERATURE ON QUANTUM IMAGING SYSTEM

This letter is formatted in three major sections. Firstly, a chapter (third chapter) gives the details of the preparation of the SPDC-based quantum source and gives the details of important properties of the source such as phase matching angle, spectral and spatial properties of the signal, and idler photons and phase matching efficiency. Chapter IV discusses the behavior of signal and idler correlation in environmental noise, and gives a detailed description of SNR's characteristics of the non-spatially resolvable systems and detectors' behaviors in the noise events. Chapter V gives theoretical and experimental details of the full-field 2D quantum imaging system. The introduced system tested for behavior in the noise background and an analytical discussion has been given. As these three titles of work have their own research directions, the details of the previous work have been described in three sections.

The underlying principle we exploited to investigate the quantum imaging system is the spontaneous parametric down-conversion (SPDC) [40, 41, 42, 43]. SPDC is an uncontrolled and randomly occurring weak process thus it is "spontaneous". As the energy is conserved in the SPDC, it is a parametric process. In the process, a high-frequency input signal is responsible for generating lower-frequency output photons so it has downconverted the frequency. A high-intensity version of the SPDC is the high gain PDC [47, 48]. Since the SPDC is a nonlinear optical process the medium should exhibit nonlinear properties. Some of the examples of the nonlinear medium used in the SPDC applications are Potassium titanyl phosphate (KTP) [49], LiNb03 [50], and beta-Barium Borate (BBO) [51] crystals. The medium of choice highly depends upon the application. For instance, for quantum imaging settings, the broad bandwidth of the signal and idler frequencies are desirable. As the spectrum of SPDC modes generated in BBO crystal display high bandwidth BBO is preferred over many in quantum imaging applications. BBO is an example of a critically phase-matched bulk crystal. There are non-critically phasematched (quasi-phase-matched) examples where the bulk nonlinear crystals (for example KTP crystal) are sandwiched (periodically polled structure)to achieve high brightness and narrow spectral bandwidth entanglement source [52, 53, 54, 55, 56]. Periodically poled nonlinear crystal is suitable in applications where brightness is very important that include quantum key distribution [57, 58], quantum teleportation [59, 60], quantum computation [61].

The experimental demonstration of SPDC is well established in a lab environment [62]. Recently, the SPDC-based systems have been deployed in rough conditions like space, underwater, and in various types of moving vehicles [60, 63, 64, 65]. Furthermore, a robust and compact SPDC source that survived even a rocket explosion has been reported [66, 67]. Such studies often point out the strict considerations on the size, weight, and power (SWaP) while aiming to keep the brightness, collection efficiency, and high entanglement fidelity [68]. As the BBO is very stable in temperature it became the best choice of medium in the satellite-based communications[66, 67]. However, to use the photon pairs at distant locations for quantum communications, they are required to be transported either in free space or through optical fibers. For both cases, the transverse modes of the down-converted photons need to be single (fundamental) Gaussian for their efficient manipulation and use. Collecting the photons to a single-mode fiber (SMF) can guarantee the single-mode profile [69], and therefore easy manipulation of the photons. However, this spatial filtering reduces the brightness, which is very critical for the design process of the pair sources. A solution to this problem is to use long crystals. But, in long crystals, the pump walk-off causes asymmetries in the down-conversion emission profile due to the birefringence of the material. This results in a reduced coupling of the down-converted photons into an SMF. Aiming to improve the brightness in a BBO-driven SPDC, there has been a wide attempt seen in the literature [70, 71, 72, 73, 74, 75, 76, 77]. The brightness requirement is not crucial in producing a quantum image. As its main application lies in the specimen studied in the lab. However, the brightness of the source is a highly important parameter in LIDAR-like imaging where the target subject is far from the detection systems.

Detection of an object which is embedded in a noisy background is a fundamental problem in sensing and imaging. Conventional techniques explore the properties of the electromagnetic field to reconstruct the structure of an object under investigation. This type of detection scheme is limited by the classical bounds [78] in some parameters including signal-to-noise ratio (SNR). These limitations are fundamental in the classical realm, and therefore overcoming its limitations requires non-classical detection methods [79]. Non-classical correlation measurement has been recognized as a candidate to surpass classical limits offering advancements in many technological frontiers such as quantum cryptography [17, 80], quantum computing [81, 82], quantum imaging [25, 83], quantum ranging [84, 85], and quantum microscopy [86]. We are specifically looking into the scope of quantum correlations in the detection and ranging of an object under a noisy background, which is of interest in LIDAR applications.

A quantum-entangled source-based detection scheme called quantum illumination (QI) suggested an exponential improvement in the SNR of detecting a sample compared to an unentangled single-photon source based detection scheme within a noisy environment [34]. Soon after, it is realized that the performance of such a system is, at best, equal to that of a coherent-state transmitter of the same average photon number, and could be substantially worse. However, as shown by Tan et al. [35], QI can offer a significant performance gain when the operation is not limited to the single-photon regime. A proof of principle experimental demonstration of QI showed a performance improvement when compared to the classical counterpart [36]. They have used the spontaneous parametric down-conversion process (SPDC) to demonstrate the QI's advantage, where signal and idler beams are generated that have maximally entangled field quadratures. However, the practical implementation of QI is restricted by limitations imposed by the random phase and random fading incurred after scattering by diffusive surfaces in realistic scenarios [87]. Thus, this system is only appropriate to use for an object that has an optically smooth surface. To overcome these problems, only non-classical temporal correlation (phase insensitive quantum system) of the pairs are often employed in QI detection scheme [88, 89, 90, 91]. Although phase-insensitive scheme does not completely offer the QI's advantages, it benefits from simple experimental settings, high response time compared to classical phase-insensitive target detection protocol based on intensity detection [89], the possibility to tune the signal and idler photons' wavelengths that enables illuminating with one wavelength and detection by another- which is applicable in covert and ghost imaging [25, 30]. In phase-insensitive systems, a test for the value of the second order correlation function ($g^{(2)}$) can be a determining parameter to test if the source is operating in the quantum or classical regime [88, 92]. If the $g^{(2)}$ value is above 2, it is an indication that the source is operating in the quantum regime, since only a quantum source can show $g^{(2)}$ above 2 in a zero-mean, statistically stationary, jointly-Gaussian state such as SPDC signal and idler.

There exists a plethora of studies that explore the quantum nature of light to improve the performance of classical Raleigh and shot noise-limited imaging techniques. Among them, most of the quantum imaging work exploits spatial correlation of the SPDC-produced signal and idler photons. In quantum imaging, the fact that the knowledge of the transverse spatial location of the signal photons allows us to know the exact spatial location of idler one enables us to reconstruct the image of a target sample/object by following reference-assisted or intensity-correlated imaging. The advantage of transverse correlation exhibiting EPR-type correlations both in continuous and discrete basis [93, 23, 94, 95] can be used to beat many classical bounds. The transverse momentum conservation is the basis of most of the quantum 2D imaging techniques and some type of work shows the quantum system beating the Rayleigh limit while others do so via beating SNL bound.

In 2004, the first demonstration of the parametric process beating classical shot noise limit has been reported by Jedrkiewicz et.al [96]. They used a high-gain PDC process and a CCD array as an imaging instrument to demonstrate a sub-SNL correlation in a specific gain regime. As the SPDC requires a single sensitive imaging technology it was a difficult task back then and more logical to use the high gain regime of the PDC. The primitive way to observe the spatial correlations in the SPDC was to scan the single photon detectors over a 2D spatial region and collectively observe the transverse momentum/ position correlations after the post-processing. Later, the sub-SNL capability of SPDC has been reported [24]. After the advancement of CCD (especially ICCD and EMCCD cameras) cameras, researchers have shifted towards using these instruments for quantum imaging applications. There exists a class of quantum imaging experiments where we use ICCD and others use EMCCD. The ICCD camera is more apt to the quantum ghost imaging techniques [97] where the reference photons trigger the camera gate leading to efficient ghost imaging [25, 26, 27, 29]. Quantum ghost imaging showed a way to use a minimum number of photons to achieve full-field 2D imaging, and therefore, the best choice for imaging sensitive samples. Edgar et.al was the first to use an EMCCD camera to demonstrate transverse momentum correlation in the SPDC [98]. The EMCCDs' >90% quantum efficiency became very suitable to show direct signal and idler one-to-one correlation without the assistance of an external triggering mechanism [99, 31].

Apart from sub-SNL imaging with the quantum source of light, beating the Raleigh limit is another area where quantum mechanical intervention showed some improvement. Given a fixed number of photons, the amount of information one can gain from an image about the separation between two sources falls to zero as the separation drops below the Raleigh limit. There are several high-profile classical techniques that show immunity to the Rayleigh limit including Fluorescence microscopy [100, 101, 102], spatial mode demultiplexing [103] and other [104, 105]. In the wake of the second quantum revolution, the field of quantum meteorology emerged [106, 107, 108]. This shows a quantum mechanical way to improve many performance metrics in an unprecedented way. That showed a dragging of the Raleigh limit to the quantum mechanical fundamental limit, the Heisenberg limit [109]. Compared to the standard quantum limit (SQL), the Heisenberg limit can down the resolution by a factor of 1/N where N is the number of photon modes. A two-fold quantum resolution enhancement in a quantum imaging scheme has been reported in different experimental schemes by employing the optical centroid measurement (OCM) [110, 39]. In ref. [39], two spatially correlated signal and idler photons which produced in an SPDC process are exploited. These pairs are strictly prepared to illuminate a single point on the sample under study. Consequently, two copies of the diffraction-limited image on the near-field plane have been observed. In a machine learning algorithm, that is efficiently trained to pick the center point on the image plane every photon pair fall on the EMCCD camera; showing a two-fold quantum improvement in a modulation transfer function (MTF) estimation performance parameter. In another experimental work, Defienne et.al [31] demonstrated a quantum imaging system called quantum image distillation that is capable of showing anti-spoofing via quantum features of light. They used SPDC-generated signal and idler photons that pass through an object directly detected by an EMCCD camera that is sensitive to single photon level and has high quantum efficiency. The object used here is a transmissive structure of a cat. To test the spoofing capability of the system an identical object that should be imaged is projected on the camera via led light exposure. The fact that SPDC photons have both time and space correlation simultaneously differentiates this imaging scheme from classical methods. If the illuminating light is a classical source the observed image would look like the overlap of noise and object; not recognizable in a classical scheme. The quantum imaging scheme uses spatial and time correlation for obtaining intensity correlation. As this process takes only photons that arrive together with a correlated pixel index of the ICCD camera, classical light will be removed, hence the final image would be the intended object. Defienne et.al's work is an efficient noise-removing method that can be ideal for imaging an object in an extreme noise background. The work presented here is closely related to Defienne et.al's work, especially the intensity correlation algorithm implementation side which recovers the image in post-processing.

CHAPTER III

THEORY OF SPONTANEOUS PARAMETRIC DOWNCONVERSION

In this chapter, a theoretical background of SPDC process is discussed. For the SPDC, critical phasematching is the basic condition to be satisfied. This cannot be achieved in any medium but a nonlinear optical one. Therefore, I have used a suitable BBO crystal for satisfying phasematching conditions. The mathematical background of the phasematching condition and the design of the nonlinear medium is discussed. Also, the spectral properties of signal and idler photons along with the momentum correlation of SPDC in a transverse position discussed. Finally, an experimental scheme showing the SPDC on a CMOS camera with various crystal lengths is demonstrated. I introduce a mathematical consideration that is critical when a long nonlinear medium is used.

3.1 Spontaneous parametric down conversion

The SPDC is probably the most used nonlinear phenomenon to explore the quantum nature of light. In the field of quantum optics, this is widely used in an experimental demonstration of quantum imaging and quantum communications. Ranging from the study of fundamental quantum phenomena to the implementation of quantum communication protocols realized by this process. The SPDC was first theoretically brought forward by Klyshko [40]and the experimental demonstration was demonstrated by Burnham and Weinberg [41]. Subsequently, this phenomenon became a test-bed for the realization of many quantum phenomena such as, relevant to this study, entangled spatiotemporal coherence, polarization entanglement [111], and non-classical photon number statistics [112]. Moreover, due to a strong time correlation of the generated fields [113] and output powers in the sub-picowatt range, the first applications in the field of meteorology were recognized soon [114]

In the SPDC process, higher frequency pump photon produces two lower frequency photons called signal and idler photons. For this to be realized, Energy and momentum conservation are the basic requirements. The energy and momentum conservation of these three fields can be written as

$$\hbar\omega_p = \hbar\omega_s + \hbar\omega_i \tag{3.1}$$

$$\hbar\mathbf{k}_p = \hbar\mathbf{k}_s + \hbar\mathbf{k}_i \tag{3.2}$$

where $\hbar$ is the reduced Plancks constant, ω is the angular frequency and k is the propagation vector of the field. The indices p, s, and i indicate the pump, signal, and idler, respectively. Equation 3.1 and 3.2 turn into a frequency and phase relations as

$$\omega_p = \omega_s + \omega_i \tag{3.3}$$

$$\mathbf{k}_p = \mathbf{k}_s + \mathbf{k}_i \tag{3.4}$$

the propagation vector can be written as $k = |\mathbf{k}| = \omega n/c$, where n is the index of refraction of the medium and c is the speed of light. Substituting this in the equation. 3.4, we get

$$\omega_p n_p = \omega_s n_s + \omega_i n_i \tag{3.5}$$

Since the wavelength of each field is different, the index of refraction is different for the pump, signal, and idler. Assuming the case, a case I explored for this study, $\omega_p > \omega_s > \omega_i$, leads to inequality condition $n_p > n_s > n_i$. Rearranging equation 3.5, we arrive a condition

$$n_p - n_s = \frac{\omega_s n_s + \omega_i n_i}{\omega_p} - n_s = \frac{(\omega_s - \omega_p)n_s + \omega_i n_i}{\omega_p} = (n_i - n_i)\frac{\omega_i}{\omega_p} \tag{3.6}$$

equation. 3.6 has no solution because $(n_p - n_s) > 0$ and $(n_i - n_i) < 0$ cannot be simultaneously satisfied in a linear optical medium. Therefore, we turned to a nonlinear medium with which the index of refraction can be tuned to satisfy the equation. 3.5.

3.2 Engineering the SPDC parameters

A birefringent medium offers to tune the index of refraction determined by the propagation direction of light. This property is beneficial in satisfying the phasematching condition as one in the equation. 3.5. Analysis of a direction vector-dependent refractive index can be simplified by following the abstract diagram as in the figure 3.1 When a light beam with a state of polarization 45° with respect to the ordinary

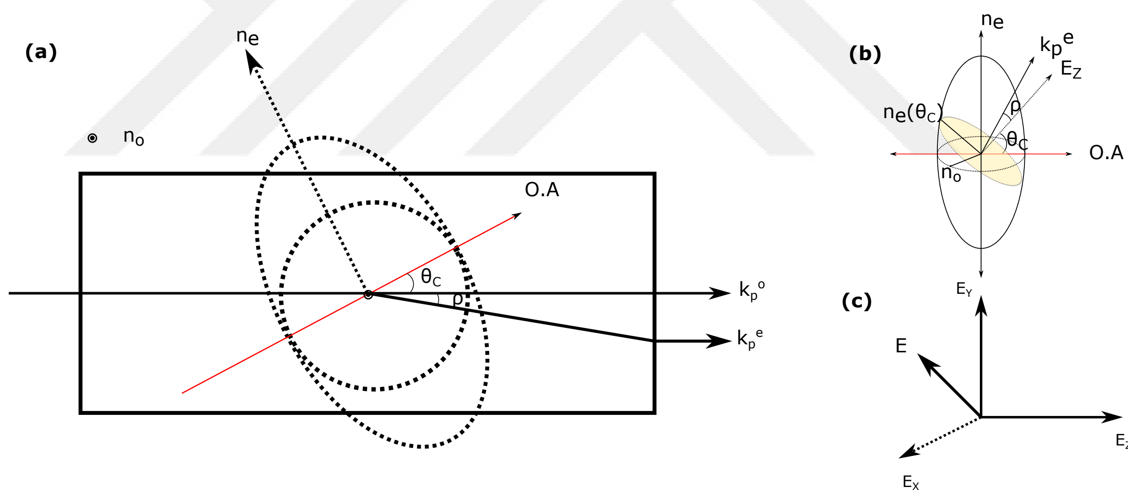

Figure 3.1: A light beam having both ordinarily (o-polarized) and extraordinarily (e-polarized) polarization components propagates through a birefringence medium and experiences a split inside a nonlinear medium. The optic axis (O.A), angle of O.A with respect to o-beam propagation (θ_c), and walk-off angle, ρ, are indicated. (b) index ellipsoid showing the axis of refractive indices (ordinary refractive index- n_o, and extraordinary refractive index - n_e). (c) electric field 3D components. The propagation direction of the light beam is parallel to E_z, n_e is parallel to E_y and n_o is parallel with E_x.

and extraordinary refractive indices propagates through a uniaxial and anisotropic medium as in figure 3.1, the light beam split up into two components called ordinarily polarized and extraordinarily polarized beams. It is noteworthy to understand if we send a light beam having a parallel linear polarization state with respect to either n_e- axis or n_o-axis, the beam after the medium will contain only the respective part. Thus, no two light rays will not be observed. The separation angle between the e-ray and o- ray is called the walk-off angle (indicated ρ in figure 3.1). This walk-off is due to the energy Poynting vector deviation in a system where asymmetric (change in refractive index due to propagation direction) refractive index of the n_e causes nonorthogonal propagation of light field E and propagation vector k [115]. By following figure 3.1(b), one can get an intuition that n_o is independent of propagation direction as it has a spherical coordinate geometry. However, the value of n_e is highly dependent on the angle plus polarization (the ellipsoid shape is symmetric only around n_e-axis while the spherical shape of n_o is symmetric in all directions). If there is an angle change either by crystal or by propagation direction of the light in the E_z and E_y plane, the effective refractive index experienced by the e-ray changes while the refractive index is always constant for the o-ray. Therefore, we get a provision to vary the refractive index by either changing the direction of the light pulse or rotating the crystal axis in the plane where the optic axis lies. However, in this study, I have played with only crystal angles for alignment simplicity.

The crystal geometry of an anisotropic medium (in this case birefringence medium) allows the classification of the SPDC by the birefringence and state of polarization of interacting fields. The birefringence is quantified by $\Delta n = n_e - n_o$, Δ gives the information of the strength of birefringence. If $n_e > n_o$ the crystal is called a positive crystal otherwise it is called a negative crystal. By polarization of pump, signal, and idler fields categorize SPDC into three types. The details of the classification of the SPDC are summarized in the table. 2. I have used type-I SPDC with negative uniaxial configuration.

Table 2: SPDC classification by birefringence and state of polarization of each field.

	Positive uniaxial $n_e > n_o$	Negative uniaxial $n_e < n_o$
Type- 0	o $\longrightarrow$ o + o	e $\longrightarrow$ e + e
Type- I	o $\longrightarrow$ o + e	e $\longrightarrow$ o + e
Type- II	o $\longrightarrow$ o + e	e $\longrightarrow$ o + e

3.2.1 Determining wavelength values

Designing a desirable SPDC configuration requires finding suitable wavelength values. I have used a continuous wave (CW) laser with a central wavelength of 405 nm and bandwidth 160 MHz as a pump field for this study. Though the degenerate wavelength is desirable for quantum imaging applications, the type-I phasematching makes it impossible to separate the signal and idler photons. To suit it, I fixed the signal wavelength to be 782 nm and by following the balance wavelength equation derived from energy conservation conditions such as the equation. 3.7 to find the idler wavelength.

$$\frac{1}{\lambda_p} = \frac{1}{\lambda_s} + \frac{1}{\lambda_i} \tag{3.7}$$

Equation. 3.7 helps to compute idler wavelengths with reference to fixed pump and signal. We have a balancing wavelength as 405 nm$\longrightarrow$ 782 nm+ 842 nm. Figure 3.2 shows the idler wavelengths correspond to various signal wavelengths.

3.2.2 Phasematching angle calculation

In the negative uniaxial with type-I SPDC configuration, an extraordinarily polarized pump converts two ordinarily polarized light fields. From the extraordinarily polarized ellipsoid geometry (refer figure 3.1) (b), the resultant refractive index experience by the pump beam can be computed by

$$\frac{1}{n_e(\theta_c)^2} = \frac{sin^2(\theta_c)}{n_e^2} + \frac{cos^2(\theta_c)}{n_o^2} \tag{3.8}$$

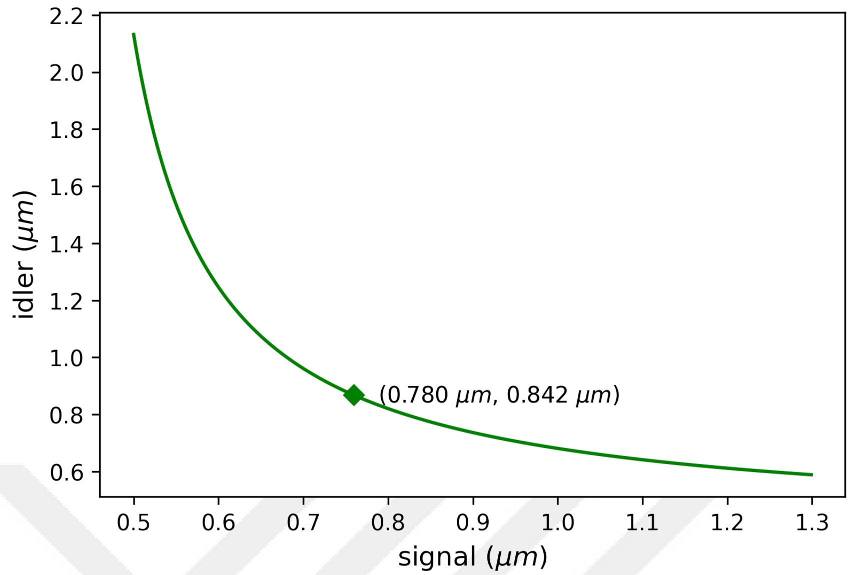

Figure 3.2: Signal idler photons wavelengths dependence graph in a laser light of wavelength 405 nm pumped SPDC process.

where θ_c phasematching angle is also called crystal cut angle because in customization of nonlinear crystal for best suit the experiment alignment this is the angle crystal is cut. After substituting $n_e(\theta_c)$ in equation. 3.5, we can learn the crystal cut angle suitable for the balanced wavelengths. Derivation of this is achieved by following

$$\omega_p \sqrt{\frac{1}{\frac{sin^2(\theta_c)}{n_e^2} + \frac{cos^2(\theta_c)}{n_o^2}}} = \omega_s n_s + \omega_i n_i \tag{3.9}$$

Also, momentum conservation (therefore frequency conservation) formula 3.5, can be written as

$$\frac{n_p}{\lambda_p} = \frac{n_s}{\lambda_s} + \frac{n_i}{\lambda_i} \tag{3.10}$$

combining equation. 3.10 and and polarizations of pump, signal and idler, we can write

$$\sqrt{\frac{1}{\frac{sin^2(\theta_c)}{(n_p^e)^2} + \frac{cos^2(\theta_c)}{(n_p^o)^2}}} = \left(\frac{\lambda_s n_i^o + \lambda_i n_s^o}{\lambda_s \lambda_i} \right) \lambda_p \tag{3.11}$$

rearranging equation.3.12 for θ_c, we get

$$\theta_c = Cos^{-1} \left(\sqrt{\left(\frac{\lambda_s^2 \lambda_i^2}{\lambda_p^2 (\lambda_s n_i + \lambda_i n_s)^2} - \frac{1}{(n_p^e)^2} \right) \left(\frac{(n_p^o n_p^e)^2}{(n_p^e)^2 - (n_p^o)^2} \right)} \right) \tag{3.12}$$

For a BBO crystal polarization and wavelength-dependent refractive indices can be calculated by Sellmier equation. The refractive indices for ordinarily and extraordinarily polarized beams can be found by

$$n^o(\lambda) = \sqrt{2.7359 + \frac{0.01878}{(\lambda^2 - 0.01822)} - (0.01354\lambda^2)} \tag{3.13}$$

$$n^e(\lambda) = \sqrt{2.3753 + \frac{0.01224}{(\lambda^2 - 0.01667)} - (0.01516\lambda^2)} \tag{3.14}$$

After learning refractive indices for pump, signal, and idler by using equations. 3.13 and 3.14 we can find the phasematching angle for the SPDC configuration by using the equation. 3.12. Figure 3.3 shows the different cut angle by varying the signal wavelength. For our configuration, it gives the crystal phasematching angle of 28.80° as marked in figure 3.3. Now, we have the information about the best phasematching angle by which we can obtain an efficient SPDC. Another factor to be considered while

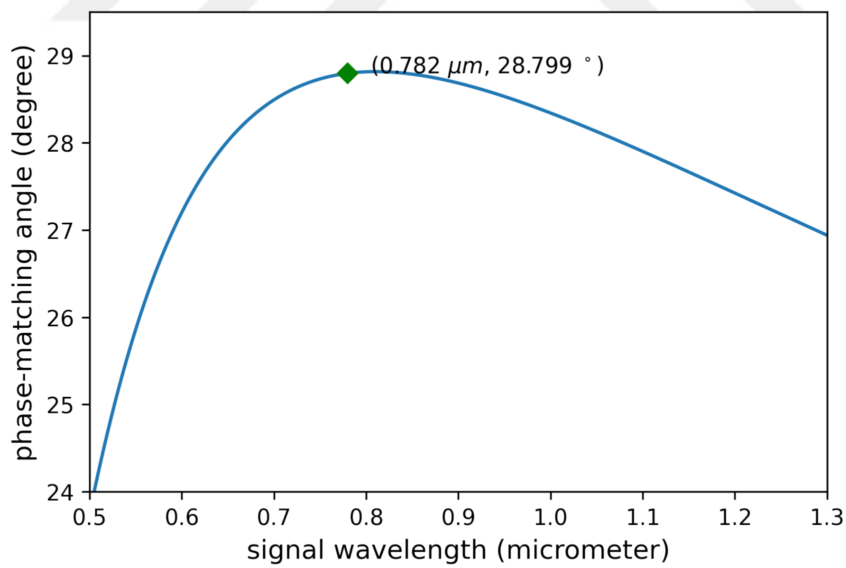

Figure 3.3: Phasematching angle values for a type-I SPDC configuration versus various signal wavelengths.

designing a nonlinear medium for SPDC is the second-order susceptibility, denoted by $\chi^{(2)}$, of the medium. It is because the SPDC is a second-order nonlinear process that requires us to have an accelerating charge for time-varying nonlinear polarization, a fundamental requirement for the new field generation[44]. The medium with a higher $\chi^{(2)}$ values is recommended for second-order nonlinear processes like SPDC. For BBO type-I $\chi^{(2)} = 4.4pm/V$

3.3 Spatial profile of the downconverted photons

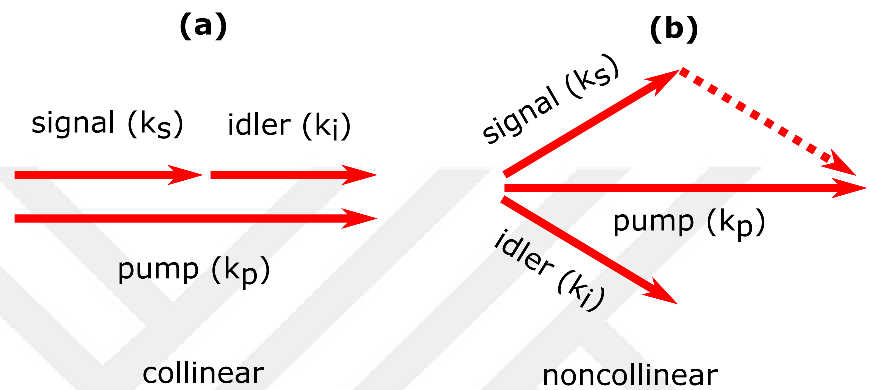

Figure 3.4: Propagation direction of pump, signal, and idler photons in a (a) collinear geometry and (b) noncollinear geometry.

With the present parameter settings, we are interested in studying phasematching in a BBO crystal. To understand the degree of phasematching, equation. 3.4 can be rewritten in a convenient form as

$$\Delta k_z = k_p - k_s \cos\phi_s - k_i \cos\phi_i \tag{3.15a}$$

$$\Delta k_x = k_s \sin\phi_s - k_i \sin\phi_i \tag{3.15b}$$

$$\Delta k_y = k_s \sin\phi_s - k_i \sin\phi_i \tag{3.15c}$$

where Δk_z is the longitudinal phase mismatch, Δk_x and Δk_y are the transverse phase mismatch, and ϕ_s and ϕ_i are the emission angles of signal and idler photons, respectively, with respect to the pump beam. The above three equations give complete information about the downconverted field distribution due to the momentum conservation of SPDC and in chapter V we will see how this momentum correlation contributes to the spatial and temporal correlation of signal idler fields. The momentum conservation dictates how the field of SPDC is distributed in a spatial area.

There are two vector configurations in which momentum conservation is satisfied. Firstly, three fields can be propagated parallel to each other. This configuration is called collinear geometry. Secondly, the pump beam, signal, and idler are propagated in different directions. This configuration is called noncollinear geometry. Figure 3.4 shows the collinear and noncollinear geometry of the SPDC modes. Analytically, the collinear geometry is a case when emission angle $\phi = 0$ as in the equation. 3.15. In the equations 3.15 , best condition would be $\Delta k_z = \Delta k_x = \Delta k_y = 0$. As we have designed the nonlinear medium appropriate to satisfy the phasematching condition, we expect $\Delta k_z = \Delta k_x = \Delta k_y = 0$ in balanced wavelengths with crystal cut angle $\theta_c = 28.80°$. Figure 3.5 shows the amount of phase mismatch in different crystal angles. As can be seen, a $\Delta k_z = 0$ is achieved when the crystal cut angle is $\theta_c = 28.80°$ and $\theta_c = \pi - 28.80°$. The latter case is just a manifestation of the case when the nonlinear crystal is rotated 180° about the plane where the optic axis and extraordinarily polarized pump lies.

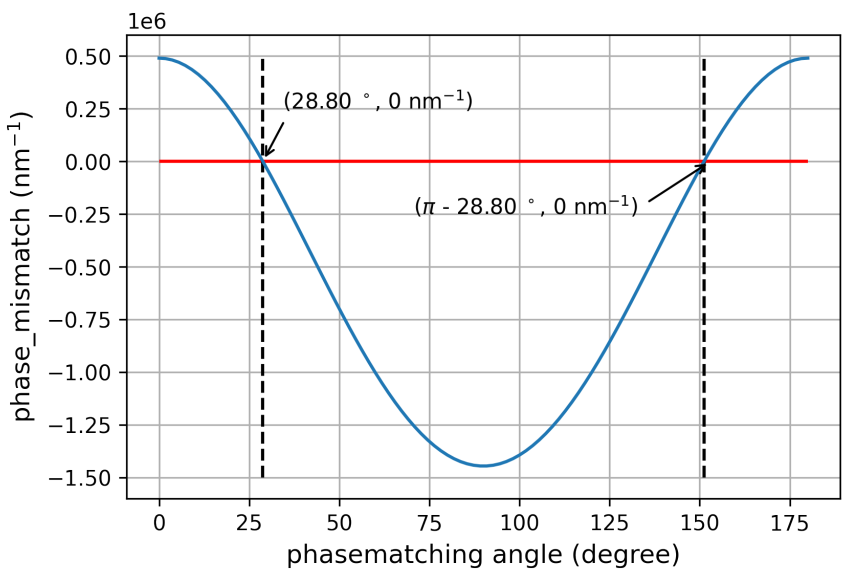

Figure 3.5: Quantification of phase mismatch (Δk) in different crystal cut angle for 405 nm $\Longrightarrow$ 780 nm + 842 nm pump signal and idler wavelengths combination. Phasematching angle 28.80° and their corresponding $\Delta k = 0$ are indicated.

3.3.1 SPDC beam profile in a collinear geometry

The phasematching condition can be used to understand the SPDC efficiency and from there we can learn the spectral distribution of the signal and idler field. The SPDC efficiency can be quantified by

$$\kappa \propto d_{eff} L Sinc\left(\frac{\Delta k L}{2}\right)^2 \tag{3.16}$$

where d_{eff} is the effective efficiency factor which is defined as $d_{eff} = \chi^{(2)}/2$ and

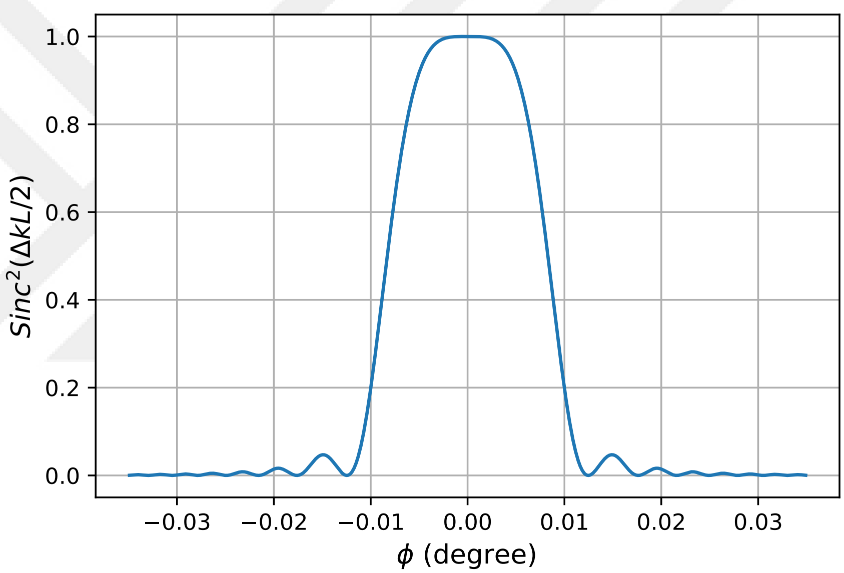

Figure 3.6: Emission profile of the SPDC in a Type - I BBO crystal of length $L = 1$ mm. The emission angle ϕ distributed between $-0.01°$ to $0.01°$.

L is the length of nonlinear crystal. The detailed derivation for the equation. 3.16 and calculation for d_{eff} can be found in reference. [44]. Equations 3.15 indicate that $\Delta k = 0$ is achieved when $\phi = 0$. However, the efficiency parameter 3.16 allows photon creation greater than $\Delta k = 0$. That leads to the spreading of downconverted photons in later space areas even in a collinear configuration. As a result, with fixed crystal cut angle 28.80° we can observe a distribution of signal and idler field as shown in the figure 3.6. The emission profile is observed when the crystal length is chosen to be 1 mm. As seen in the figure 3.6 the signal-idler photons are emitted from the nonlinear crystal in a span of around $-0.01°$ to $0.01°$ even when a collinear SPDC configuration is set. This span of emission angle distribution of the SPDC when seen in a plane parallel to the crystal surface will show a Gaussian field distribution. In figure 3.7, an SPDC beam profile in a collinear geometry is seen. This profile of SPDC later field originated by the transverse momentum conservation can be used for quantum imaging applications as we will see in chapter V.

In a noncollinear geometry, a circular ring of SPDC field is observed as expected from momentum conservation. The right figure in the figure 3.7 shows the simulated result of a noncollinear SPDC when the phase matching angle is $28.85°$,i.e when a phasematching angle offset of $0.05°$ in an SPDC configuration designed for the phasematching angle $28.80°$.

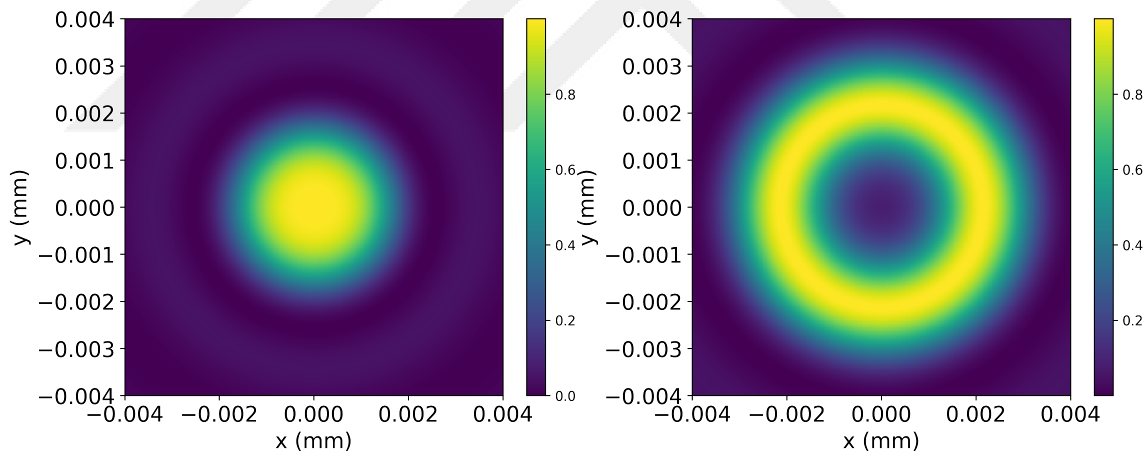

Figure 3.7: Emission profile of the downconverted modes for a Type-I SPDC configuration seen 3 mm away from the nonlinear crystal of $L = 1$ mm (left) when the crystal cut angle is $28.80°$, that is collinear, and (right) $28.8 + 0.05°$; noncollinear.

3.3.2 Crystal length on emission profile

In equation. 3.16 it is clear that the efficiency of SPDC process is linearly inversely proportional to the crystal length. The sinc function in the equation. 3.16 manifest a scenario that coherent of the crystal is $L = 2/\Delta k$. That when plotted against the phase mismatch we can observe a figure 3.8. From the figure, we can conclude that the efficiency comes to a zero when Δk span to $2/L$. Therefore, the emission beam profile is narrowed when a longer crystal is used. for instance, if the crystal length is 1 mm long then the emission distribution is around 20 times broader compared to the case where the crystal used is 10 mm. The broader emission field is desirable when it comes to quantum imaging applications as it can increase the area of the field of illumination on an imaging sample. when a long crystal is used, the sight of the cross-section can be small therefore there is a high chance of momentum conservation being lost as multiple cross-section creates the SPDC modes.

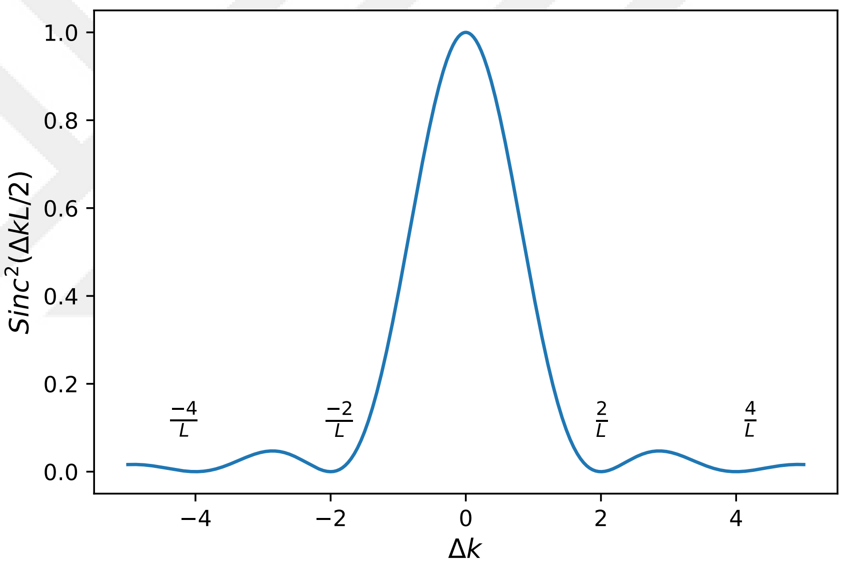

Figure 3.8: Crystal length dependence of emission profile of the SPDC. As the phase match decreases the efficiency also decreases and touched the efficiency value of zero when the Δk reaches $2/L$.

3.3.3 Beam walk-off in spatial profile due to birefringence

The birefringence nature of the anisotropic media used for the SPDC creation causes an unwanted spatial profile. As only an extraordinarily polarized pump beam can satisfy critical phasematching conditions so there can be walk-off affected beam profile.

The amount of walk-off in a nonlinear medium can be quantified using

$$\rho = Tan^{-1}\left(\left(\frac{n_p^o}{n_p^e}\right)^2 Tan(\theta_c) - \theta_c\right) \tag{3.17}$$

The SPDC signal and idler are created above or below the extraordinarily polarized (if the signal beam is created above the above extraordinarily polarized pump vector,k_p^e, then the idler will be created below the k_p^e and vice versa) pump beam. The down-converted beam created above k_p^e (refer figure 3.9) travels a greater distance inside the crystal compared to the one below. Also, between SPDC photons created above the pump vector k_p^e at the starting edge of the crystal and the ending edge of the crystal shows a greater offset due to transverse width due to walk-off. As a result, the beam profile seen in the plane parallel and away from the nonlinear crystal will show a broader ring, in a noncollinear geometry, compared to the lower edge as depicted in the figure 3.9. The figure 3.9 shows annular asymmetry in the noncollinear SPDC geometry. The figure shows only noncollinear geometry because the SPDC beam profile change is more evident in this case. Collinear SPDC also has the spatial profile misshape, but it would not be evident as in the noncollinear case. As one can relate, even though the walk-off angle is the same for any crystal length the later amount of shift that is quantified by $LTan(\rho)$ is higher as the length of the crystal enlarged. Therefore, this effect is ignored in short crystals. As we will see in the upcoming section, this asymmetric beam profile is evident starting from $L = 4mm$.

I have created a mathematical model that can be useful for spatial profile analysis. The developed model uses the geometry of three wave vectors shown in figure 3.9 (a) to form the spatial distribution of SPDC modes. The developed model can be expressed as:

$$x = \sin\phi_\mu(L - a + d)\tan\theta_\mu \tag{3.18}$$

$$y = \cos\phi_\mu(L - a + d)\tan\theta_\mu - a\tan\rho \tag{3.19}$$

Here x and y are the coordinates in the x-y plane, ϕ_μ is the azimuth angle of the down-converted photons' propagation direction, a is the variable which takes values between 0 and L, and d is the distance between the end of the crystal and image plane. Therefore, in a specific emission angle, equations 3.18 and 3.19 form an annular SPDC mode shape as shown in figure 3.9 (b). The contribution of the pump waist in the formation of the asymmetry due to walk-off is very small compared to the effect of the crystal length. Therefore, the effect of the pump waist is not included in the model. For non-collinear geometry, down-converted photons are distributed circularly around the pump respecting the law of momentum conservation. As a result, a conical solid shape of SPDC modes is formed. The annular distribution of down-converted photons, that are observed in the x-y plane, is shown in figure 3.9 (a). Due to the walk-off effect, photons born above the pump beam have a greater angle compared to below ones with respect to the pump and consequently, the asymmetrical annular shape is formed. However, the angles of the photons born at the right and left of the pump in the x-z plane are equal with respect to the pump propagation direction.

3.3.4 Experiment for beam profiling

The experimental scheme to study the characteristic beam profile is shown in figure 3.10. A pump ray of central wavelength 405 nm and bandwidth of 160 MHz passes through a BBO crystal. A bandpass filter with $\Delta\lambda = \pm 5$ is placed before the BBO to clean fluorescence noise that is indicated $F1$ in the figure. Here, BBO is the SPDC photon-creating sight. The signal and idler are parallelly propagated as the BBO is configured for Type I SPDC. The BBO is cut at 28.80° so that a normal pump ray incidence on the crystal is a condition for phase matching in our settings. After the BBO crystal, a long pass filter with cut-on wavelength 750 nm (indicated F2 in the figure 3.10)is placed. This will cutoff the pump beam from imaging on the camera. Finally, the beam profile is studied by imaging the SPDC beam on a CMOS

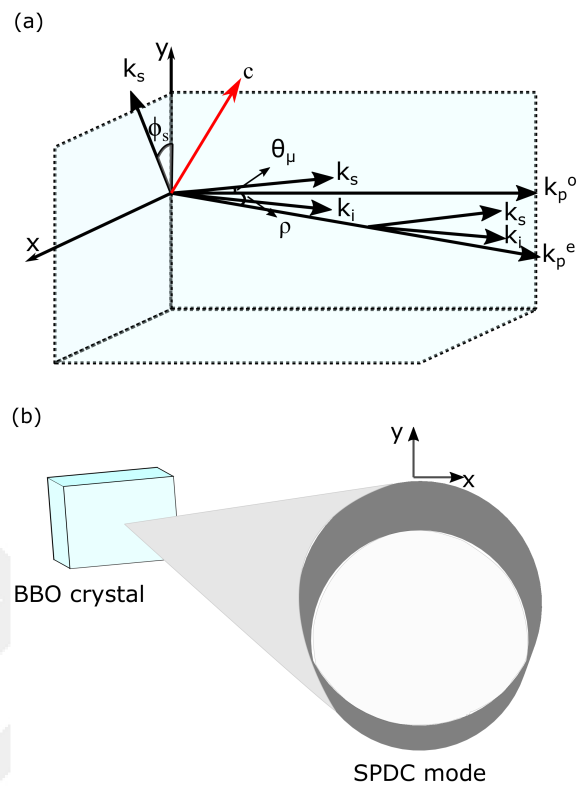

Figure 3.9: Schematic of the propagation direction of the pump, signal, and idler beam with various source characteristics indicated, (a) where k_p^o and k_p^e are ordinarily polarised and extraordinarily polarised pump wave vectors, respectively. The optic axis of the crystal is marked with 'c'. (b) The generated SPDC modes in three dimensions show SPDC annular mode.

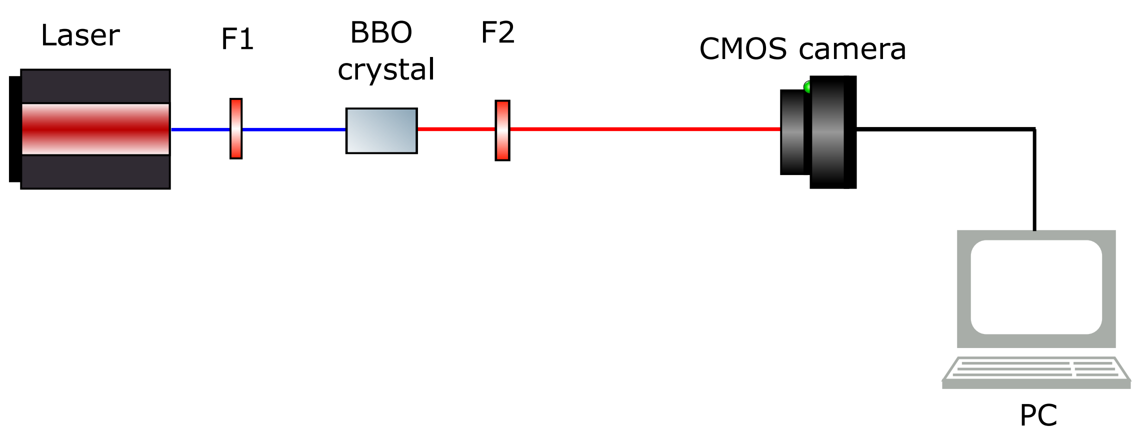

Figure 3.10: Experimental scheme used for SPDC beam profiling.

camera (Thorlabs DCC1645C-HQ). A CMOS camera obtained images of SPDC beam

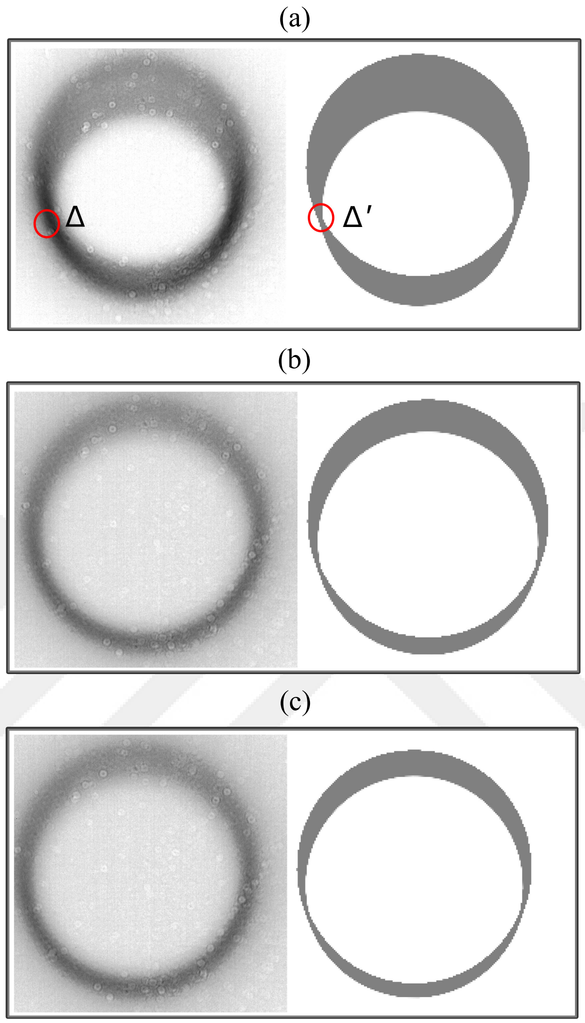

Figure 3.11: Experimental (left) and the corresponding simulated (right) images of SPDC modes. Panel (a), (b) and (c) are the typical asymmetrical profile of the SPDC emission for crystal length values of 10 mm, 6 mm, and 4 mm, respectively. Given SPDC modes have 1.5° emission angle.

for three lengths are shown in figure 3.11. The results confirm the theoretical model developed and the asymmetry is more evident in a 10 mm long nonlinear crystal compared to shorter crystals. Asymmetry is cannot be differentiated when the $L < 4mm$. The observed SPDC modes are seen with annular asymmetry which supports the theoretical prediction. I have used equations. 3.18 and 3.19 to simulate the SPDC mode shapes. Compared to the simulated images, the experimentally captured images have small difference in the region indicated with "Δ" and "Δ'". Because, the phase mismatch (Δk) arises from finite pump beam waist, which is not included as it is not significant compared to the effect of the crystal length.

3.3.5 Quantification of the Asymmetry

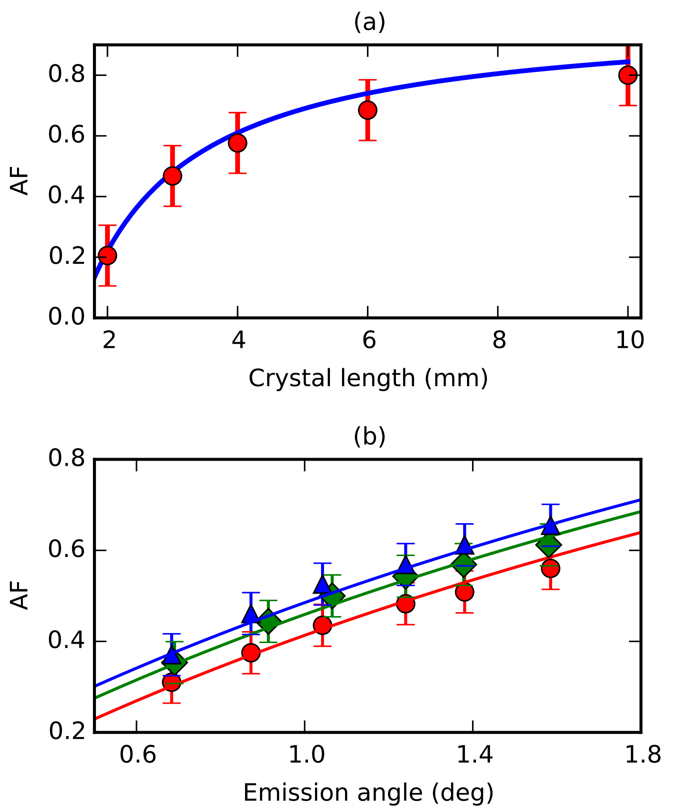

Figure 3.12: (a) Asymmetry value for crystal length as a varying SPDC parameter. The error value is ± 0.1 in the y-axis. (b) Asymmetry of SPDC photons for different pump beam waist. The data points with triangle, diamond, and circle shapes correspond to the pump beam waist of 118 μm, 78.6 μm, and 47.2 μm, respectively. The solid line is the theoretical fit using equations 3.18 and 3.19. The propagation of error is calculated to be 0.046 on the y-axis.

A parameter called asymmetry factor (AF) is introduced to quantify the asymmetry in the SPDC mode profile. It is defined as $AF = 1 - a/b$, where a is the thickness of the annulus in x axis, and b is that of the y-axis. We study the effect of crystal length, pump beam waist, and the phase matching angle on AF separately by varying one input parameter and fixing the other two. The experimental results show that AF increases with $L^{0.5}$ as shown in figure 3.12 (a). The theoretical plot (solid line) in the figure is plotted by using equations. 3.18 and 3.19. The error plot in the figure is made by considering the phase mismatch value which is not considered in the equation, along with propagated instrumental errors. Since the SPDC photons are generated throughout the length of the crystal, the width of the SPDC annulus is larger for long crystals. This effect, combined with the walk-off effect, explained in the previous section leads to greater asymmetry in the long crystals compared to short ones. To know the asymmetry due to the alignment of the crystal, we fix the crystal length and pump beam waist and rotate the BBO crystal, which effectively changes the emission angle. We observed that AF is almost linearly increasing with emission angle as seen in figure 3.12 (b). Because the walk-off angle for the extraordinarily polarised pump beam with respect to the crystal optic axis increases with the emission angle. As a result, asymmetry due to the walk-off effect is proportional to the emission angle. The blue, green, and red curves in figure 3.12 (b) are plotted for pump waist values of 118 μm, 78.6 μm, and 47.2 μm, respectively.

3.4 Quantum mechanical description

3.4.1 Single Mode Description

Until now we have discussed the basic requirement for the SPDC process to happen and analyzed the SPDC output characteristics accordingly. The dynamics of the spontaneous down conversion process follow the description of quantum mechanics. We know that, according to Larmor's theorem, the accelerated charges in the interacting medium are responsible for the generation of the new EM fields [44]. Therefore, we can model the SPDC modes by following the treatment of the quantum Harmonic oscillator. The discrete allowed energy states in a harmonic oscillator are given by the quantum Hamiltonian. Hamiltonian operator of the form suitable for our study is given by

$$\hat{H}_0 = \hbar\omega(\hat{a}\hat{a}^\dagger + \frac{1}{2}) \tag{3.20}$$

where $\hat{a}$ and $\hat{a}^\dagger$ are the well-known quantum annihilation and creation operators, respectively. As the words suggest, the annihilation operation is the process associated with absorbing the input EM field (pump in our case)by the medium and the creation operation is the process of creating a new EM field via satisfying energy and momentum conservation. As we can think in the case of the SPDC process, the signal and idler are not present before the interaction with the external field and therefore we need to add interaction Hamiltonian and its evolution process. The interaction of the external pump with a nonlinear crystal provokes a field generation (two-field generation in the case of SPDC). The SPDC process has a background of the nonlinear wave equation, therefore, we can formulate the interaction Hamiltonian with:

$$\begin{aligned}\hat{H}(t)_I &= \int_v P^{NL} E_i d^3r \\ &= \int_v \chi^{(2)}_{i,j,k} \epsilon_0 E_i E_j E_k d^3r \end{aligned} \tag{3.21}$$

By quantum treatment, we know that electric field vector E can be written into components form by following

$$E(z,t) = C_0(\hat{a}e^{i(kz-\omega t)} + \hat{a}^\dagger e^{-i(kz-\omega t)}) \tag{3.22}$$

$$= E^{(+)} + E^{(-)} \tag{3.23}$$

where C_0 is the strength of the vacuum field that equals $(\hbar\omega/2\epsilon_0 V)^{1/2}$. In the SPDC process, the pump photons are annihilated and signal and idler ones are created. Therefore, the pump electric field takes only $E^{(+)}$ and both signal and idler are $E^{(-)}$

in equation. 3.21 and now we reach a new interaction Hamiltonian of the form

$$\hat{H}(t)_I = \int_v \epsilon_0 \chi_{i,j,k} \hat{E^{(+)}}_p \hat{E^{(-)}}_s \hat{E^{(-)}}_i d^3r \tag{3.24}$$

$$\hat{H}(t)_I = \epsilon_0 \chi_{i,j,k} E_{p0} E_{s0} E_{i0} \int_0^L a_p e^{i(k_p z - \omega_p t)} \hat{a_s}^{\dagger} e^{-i(k_s z - \omega_s t)} \hat{a_s}^{\dagger} e^{-i(k_s z - \omega_s t)} dz + h.c., \tag{3.25}$$

where h.c stands for Hermitian conjugate. Notice the electric field vectors turn to $\hat{E}$ from E. Because in quantum mechanics we treat the physical operations by applying corresponding parameter operators. We have taken two approximations here. Firstly, the SPDC is a very weak process, and therefore pump field is extremely high compared to the signal and idler. Therefore, we can treat the pump beam as a classical field i.e., $\hat{a_p} \rightarrow a_p$. Secondly, compared to transverse field vector magnitude the axial ones are very larger (paraxial approximation) thus we can take $d^3r \rightarrow dz$. The interaction Hamiltonian and interaction-free vacuum state of the signal and idler photons give the total Hamiltonian of the system which is given by

$$\begin{aligned} \hat{H} = & \sum_{m=s,i} \hbar\omega(\hat{a_m}\hat{a_m}^{\dagger} + \frac{1}{2}) \\ & + \epsilon_0 \chi_{i,j,k} E_{p0} E_{s0} E_{i0} \int_0^L a_p e^{i(k_p z - \omega_p t)} \hat{a_s}^{\dagger} e^{-i(k_s z - \omega_s t)} \hat{a_s}^{\dagger} e^{-i(k_s z - \omega_s t)} dz + h.c., \end{aligned} \tag{3.26}$$

This Hamiltonian of the system gives us the vacuum and the generated signal and idler fields' energies. When a pump photon interacts with a nonlinear crystal that can satisfy the momentum and energy conservation as discussed in the previous sections there is a probability (defined by the efficiency of the SPDC) that the pump photon absorbed and equivalent energy converts into signal idler modes. This is a number-state operation and when it happens the energy of the particle is promoted to a higher state and returns by emitting photons. Before pump photons interaction there is no signal and idler photons present. However, signal and idler have vacuum energy even when the system is isolated from any interaction. When the pump interacts, quantum mechanically speaking, it is applying a creation operation to the vacuum state of the

SPDC modes. The creation operation applying on a vacuum state is described by the quantum Fock state (number state) operation given by

$$\hat{a}^{\dagger} \left| VAC \right\rangle_{s(i)} = \sqrt{0+1} \left| \omega_{s(i)} \right\rangle \tag{3.27}$$

where $|VAC\rangle$ stands for vacuum state. In a single conversion process (single cycle), the particle goes to a higher state by absorbing the pump and emits back to the ground state releasing a photon in this process. Therefore, $\hat{a}\hat{a}^{\dagger}$ applies to the vacuum state of signal or idler photons will give us the number of SPDC processes. The statistical representation of this number state operation is written as [116]

$$\hat{a}_s \hat{a}_s^{\dagger} \left| n \right\rangle = \hat{n} \left| n \right\rangle = n \left| n \right\rangle \tag{3.28}$$

In a single process ($n = 1$), equation 3.28 is $\hat{a}_s \hat{a}_s^{\dagger} \left| n \right\rangle = \left| n \right\rangle$. We can take that eigenvalue gives the number of SPDC and their state is the eigenstate in a linear operation. In Heisenberg's treatment of quantum mechanics, the time evolution of the field operators is described by the coupled equations of motion and their Hermitian conjugate [117], mathematically written as

$$\frac{d\hat{a}_{s(i)}}{dt} = \frac{1}{i\hbar}[\hat{a}_{s(i)}, \hat{H}] = -i(\omega_{s(i)}\hat{a}_{s(i)} + g\hat{a}_{i(s)}a_p) \tag{3.29}$$

where g is the gain factor proportional to the efficiency of the SPDC process (one can deduct g from equation 3.26). With Manley-Rowe relations [118] we know that when there is a signal photon there must be an idler photon present as momentum and energy conservation do not satisfy otherwise. Equation 3.29 has solution given by [119]

$$\hat{a}_s(t) = e^{-i\omega_s t} \left(\hat{a}_s(0) cosh(\kappa |a_p|) - i\hat{a}_i^{\dagger}(0) sinh(\kappa |a_p|) \right) \tag{3.30}$$

$$\hat{a}_i(t) = e^{-i\omega_i t} \left(\hat{a}_i(0) cosh(\kappa |a_p|) - i\hat{a}_s^{\dagger}(0) sinh(\kappa |a_p|) \right) \tag{3.31}$$

See equation 3.16 for the calculation of κ. For obtaining the number of signal and idler photons, we can perform $\hat{n_s}(t) = \hat{a}_s^{\dagger}(t)\hat{a}_s(t)$. We take that at t $= 0$ signal and idler are in the vacuum state therefore, $n(0) = \hat{a}_s^\dagger(0)\hat{a}_s(0) = 0$. We can write the average number of signal and idler photons produces as

$$\left\langle n(t)_{s(i)} \right\rangle = n_{s(i)}(0) cosh^2(\kappa|a_p|) + \left(1 + n_{i(s)}(0)\right) sinh^2(\kappa|a_p|) \tag{3.32}$$

It should be noted that equation 3.32 has a constant value of 1, which underlines in any initial conditions a nonzero contribution $sinh^2(\kappa|a_p|)$ to the average photon number will persist. Thus, even if the signal and idler modes are initially in vacuum states, i.e. $n_s(0) = n_i(0) = 0$, after a time period t (interaction time) long enough there will be photons in these modes. This purely quantum-mechanical effect suggests the possibility of spontaneous emission in parametric down-conversion, which emerges as an amplification of the vacuum fluctuations associated with the non-commutative of the field operators. We can get after taking $n_s(0) = n_i(0) = 0$, average signal-idler pairs in the SPDC with

$$\left\langle n(t)_{s(i)} \right\rangle = sinh^2(\kappa|a_p|) \sim (\kappa|a_p|)^2 \tag{3.33}$$

as $\kappa|a_p| << 1$ in a crystal length of a few mm order. The creation and annihilation operators of the signal and idler photons of the mathematical form given in equation 3.30 and 3.31 can be used to investigate the important statistical parameters such as variance (first-order moment) and signal and idler photons' cross-correlation. The normalized second-order moment of the signal and idler photons can be written as

$$\left\langle : \delta^2 n(t)_{s(i)} : \right\rangle = \langle 0,0| \, \hat{a}_{s(i)}^{\dagger 2}(t)\hat{a}_{s(i)}^2(t) \, |0,0\rangle \tag{3.34}$$

$$= 2sinh^4(\kappa|a_p|) \tag{3.35}$$

where $\langle : ... : \rangle$ indicates the second moment is taken in normalized photon statistics. From a practical viewpoint, this means that statistical parameters should be measured within the coherence time of the photon source. Similar to equation 3.35, we can compute the cross-correlation of the signal and idler field by following

$$\langle : n_s(t)n_i(t) : \rangle = \langle 0,0| \, \hat{a}_s^\dagger(t)\hat{a}_i^\dagger(t)\hat{a}_s(t)\hat{a}_i(t) \, |0,0\rangle \tag{3.36}$$

$$= 2sinh^2(\kappa|a_p|) + 2sinh^4(\kappa|a_p|) \tag{3.37}$$

This lead to a quantum inequality condition that holds

$$\langle : n_s(t)n_i(t) : \rangle > \frac{1}{2}\left(\langle : n^{(2)}(t)_s : \rangle + \langle : n^{(2)}(t)_i : \rangle\right) \tag{3.38}$$

equation 3.38 cannot hold in a classical system. This is a signature of the quantum state and therefore used to distinguish a quantum and classical system. Classical conditions holds $\langle : n_s(t)n_i(t) : \rangle \leq \frac{1}{2}\left(\langle : n^{(2)}(t)_s : \rangle + \langle : n^{(2)}(t)_i : \rangle\right)$. In an experimental scenario, this means that rate of signal and idler coincidence (R_{si})rate is greater than the sum of signal and idler photons' self-coincidence values halved ($1/2(R_{ss} + R_{ii})$) [120] i.e.,

$$R_{si} > \frac{1}{2}(R_{ss} + R_{ii}) \tag{3.39}$$

This inequality has been used in various forms to test the quantum nature of the SPDC. One such is the Cauchy-Schwarz inequality (ϵ) given by [36, 92, 121]:

$$\epsilon = \begin{cases} \frac{Covar(n_s,n_i)}{\sqrt{Var(n_s).Var(n_i)}} \leq 1 \;\; \textbf{standard definition} \\ \frac{\langle : \delta n_s \delta n_i : \rangle}{\sqrt{\delta^2 n_s \delta^2 n_i}} \leq 1 \;\; \textbf{statistical fluctuation formulation} \\ \frac{g_{si}^{(2)}}{\sqrt{g_{ss}^{(2)} g_{ii}^{(2)}}} \leq 1 \;\; \textbf{coincidence measurement formulation} \end{cases} \tag{3.40}$$

where $\langle : \delta n : \rangle = \langle n - \langle n \rangle \rangle$ and $\langle : \delta^2 n : \rangle = \langle (n - \langle n \rangle)^2 \rangle$. The third equation in equation 3.40 is used more often when two single-photon detectors are used to make a signal and idler temporal coincidence measurement. The second-order cross-correlation $g_{si}^{(2)}$ and self-correlation ($g_{ss}^{(2)}$ and $g_{ii}^{(2)}$) defines $g_{si}^{(2)} = \langle : n_s(t)n_i(t) : \rangle / (\langle n_s(t) \rangle . \langle n_i(t) \rangle)$. By substituting equations 3.33 and 3.37 we get

$$g_{si}^{(2)} = 2 + 2/sinh^2(k|a_p|) \tag{3.41}$$

Equation 3.42 suggests that $g_{si}^{(2)}$ can go beyond 2 and with small pump photon intensity I ($I \sim a_p^2$) the correlation can be stronger, a direct identifier of a quantum regime.

3.4.2 Multi Mode Description

In the previous section, we have assumed that all three interacting fields are monochromatic and each possesses a definite propagation vector (k- vector). In a practical setting, even if the input signal is monochromatic, the single frequency output cannot be expected as the phasematching allows certain wavelength combinations of the signal and idler (refer to section 3.5 for more details). For the multi mode description of the SPDC, we need to revisit equations 3.23 and 3.25 and modify them for the possible modes of SPDC. Firstly, the pump, signal, and idler fields can be written as[45]

$$\hat{E}_p^{(+)}(r,t) = \int d\omega_p \int d^2 q_p V(q_p, \omega_p) e^{i(q_p \rho + k_p z - \omega_p t)} \quad \textbf{pump} \tag{3.42}$$

$$\hat{E}_{s(i)}^{(-)}(r,t) = E_{s0(i)}^* \int d\omega_{s(i)} \int d^2 q_{s(i)} \hat{a}^\dagger(q_{s(i)}, \omega_{s(i)}) e^{-i(q_{s(i)} \cdot \rho + k_{s(i)z} z - \omega_{s(i)} t)} \quad \textbf{signal, idler}. \tag{3.43}$$

Since the pump field is treated as a classical spatial Gaussian, the annihilation $E_p^{(+)}$ lead to $V(q_p) = exp(-q_p^2 W_0^2/4) exp(-i.q_p^2 d/\omega_{p0})$. As we will see in chapter V, we are highly interested in the transverse field of the signal and idler fields. Therefore, it is more convenient to separate the transverse and longitudinal modes in equations 3.42 and 3.45, which is done by considering $k = (k_x, k_y, k_z) = (q, k_z)$ and $r = (x, y, z) = (\rho, z)$. With these, the new interaction Hamiltonian takes the form of:

$$\begin{aligned}\hat{H}_I(t) = \epsilon_0 \chi^{(2)} E_{p0} E_{s0} E_{i0} \int_v d^3 r \int\int\int d\omega_p d\omega_s d\omega_i \\ \times \int\int\int d^2 q_p d^2 q_s d^2 q_i V(q_p, \omega_p) e^{i(q_p \rho + k_p z - \omega_p t)} \hat{a}^\dagger(q_s, \omega_{s(i)}) \\ \times e^{-i(q_s \cdot \rho + k_{sz} z - \omega_s t)} \hat{a}^\dagger(q_i, \omega_i) e^{-i(q_i \cdot \rho + k_{iz} z - \omega_i t)} + h.c.,\end{aligned} \tag{3.44}$$

In the SPDC each pump photon passes through the nonlinear crystal for a certain time depending on the length of the crystal. Before the pump interacts with the nonlinear medium the signal and idler are in the vacuum energy state. Therefore, before the interaction, the state of signal-idler is given by $|\psi(0)_{tp}\rangle = |VAC\rangle_s |VAC\rangle_i$. Let us suppose at t = 0 the pump photon reaches the start surface of the crystal and at t = t this interaction ends. By the interaction, the vacuum state evolved by following the perturbation theory

$$|\psi(t)_{tp}\rangle = e^{-\frac{i}{\hbar}\int_0^t H_I(t)dt} |\psi(0)_{tp}\rangle \tag{3.45}$$

The Taylor expansion of the perturbation equation 3.45 and selecting only influencing terms lead equation 3.45 to turn

$$|\psi(t)_{tp}\rangle = -\frac{i}{\hbar}\int_0^t H_I(t)dt\, |\psi(0)_{tp}\rangle\,. \tag{3.46}$$

Since the SPDC is a very weak process only a second-order term is taken from the Taylor expansion. After substituting equation 3.45 to 3.46 and rearranging, we get a full SPDC multi mode equation given by:

$$\begin{aligned}|\psi(t)_{tp}\rangle = -\frac{i}{\hbar}\epsilon_0\chi^{(2)}E_{p0}E_{s0}E_{i0}\int_0^t e^{i(\omega_p-\omega_s-\omega_i)t}dt\int_{-\infty}^{-\infty} e^{i(q_p-q_s-q_i)\rho}d^2\rho\int_0^L e^{i(k_pz-k_sz-k_iz)z}dz\\ \int\int\int d\omega_p d\omega_s d\omega_i \times \int\int\int d^2q_p d^2q_s d^2q_i V(q_p,\omega_p)\\ \times\, \hat{a}^\dagger(q_s,\omega_{s(i)})\,|VAC\rangle_s\, \hat{a}^\dagger(q_i,\omega_i)\,|VAC\rangle_i + h.c., .. \end{aligned} \tag{3.47}$$

We have appropriately taken $\int_v d^3r \rightarrow \int d^2\rho \int dz$. Since the interaction time span of the pump photons through the crystal (t) is longer than the SPDC conversion time, we can assume time integral limits extend through $-\infty$ to ∞ [122] i.e.,

$$\int_{-\infty}^{\infty} e^{i(\omega_p-\omega_s-\omega_i)t}dt = \delta(\omega_s+\omega_i-\omega_p). \tag{3.48}$$

Also, the transverse area of the SPDC modes is much greater than the same mode of the pump. Therefore, the assumption we made for the time domain goes with the space one,which goes,

$$\int_{-\infty}^{\infty} e^{i(q_p - q_s - q_i)t} d^2\rho = \delta(q_p - q_s - q_i). \tag{3.49}$$

The phasematching term in the equation 3.47 can be conveniently written as

$$\begin{aligned}
\Phi &= \int_0^L e^{i(k_p z - k_s z - k_i z)z} dz \\
&= \int_0^L e^{i\Delta k z} dz \\
&= LSinc(\Delta k L/2) e^{i\Delta k L/2}
\end{aligned} \tag{3.50}$$

This is in line with what we expect and the phasematching function scales the conversion efficiency of the SPDC process. After substituting the above results we get a confined two-photon state given by:

$$\begin{aligned}
|\psi(t)_{tp}\rangle = -\frac{i}{\hbar}\epsilon_0 \chi^{(2)} E_{p0} E_{s0} E_{i0} \int\int\int d\omega_p d\omega_s d\omega_i \times \int\int\int d^2q_p d^2q_s d^2q_i V(q_p, \omega_p) \\
\delta(\omega_s + \omega_i - \omega_p)\delta(q_p - q_s - q_i)\Phi \\
\times \hat{a}^\dagger(q_s, \omega_{s(i)}) |VAC\rangle_s \hat{a}^\dagger(q_i, \omega_i) |VAC\rangle_i + h.c., ..
\end{aligned} \tag{3.51}$$

Applying a creation operation ($\hat{a}^\dagger$) to a vacuum state leads to a number state creation and this fact reflects in the equation 3.51 as $\hat{a}^\dagger(q_s, \omega_{s(i)}) |VAC\rangle_s \hat{a}^\dagger(q_i, \omega_i) |VAC\rangle_i = |q, \omega\rangle_s |q, \omega\rangle_i$. Also, the Hermitian conjugate (h.c) hides a process that conditions the conjugate operation of creation operation such as $\hat{a}(q_s, \omega_{s(i)}) |VAC\rangle_s \hat{a}(q_i, \omega_i) |VAC\rangle_i = 0$. Finally, we arrive

$$\begin{aligned}
|\psi(t)_{tp}\rangle = -\frac{i}{\hbar}\epsilon_0 \chi^{(2)} E_{p0} E_{s0} E_{i0} \int\int\int d\omega_p d\omega_s d\omega_i \times \int\int\int d^2q_p d^2q_s d^2q_i V(q_p, \omega_p) \\
\delta(\omega_s + \omega_i - \omega_p)\delta(q_p - q_s - q_i)\Phi |q, \omega\rangle_s |q, \omega\rangle_i .
\end{aligned} \tag{3.52}$$

Equation 3.52 gives a complete description of the two-photon state and this formulation of the SPDC allows us to learn the behavior of the imaging technique discussed in this work.

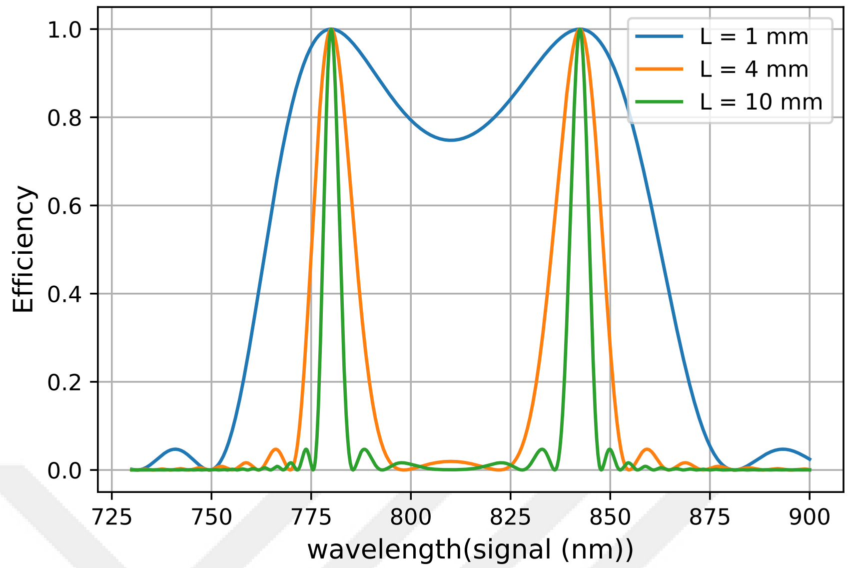

Figure 3.13: Spectral distribution for signal and idler photons when the length of the crystals are 1 mm, 4 mm, and 10 mm. FWHM values are 30 nm, 10nm, and 4 nm. The central frequency of the signal and idler are 780 nm and 842 nm when the pump wavelength is 405 nm at crystal phasematching angle 28.80°.

3.5 Spectral properties of SPDC

The wavelengths of generated signal and idler pairs are distributed with an amount of bandwidth due to phasematching conditions. I have noticed that with reference to the equation 3.16 and its simulation figure 3.6 some amount of mismatch, i.e., $\Delta k \neq 0$ is still allowed for SPDC generation. This allowed mismatch of Δk permit to have various signal-idler wavelength modes even when the pump wavelength has a perfect delta function. To investigate this, we need to scan the signal-idler wavelength in the equation. 3.16 with fixed pump wavelength phasematching angle. I have put the wavelength of the pump to be 405 nm and a phasematching angle of 28.80° in the equation. 3.15 and varied the signal and idler wavelength in an expected range of wavelength values. The result of this procedure is shown in the figure 3.14. In the figure, there are three crystal length values have been taken and studied signal and idler spectral properties. As expected when a long crystal (in this example L = 10 mm) is used the signal-idler spectrum showed narrow compared to the short crystal one. It is intuitive as the allowed Δk mismatch is small for long crystal SPDC setting as discussed in section 3.3.2. Also, note that the spectral width of the signal and idler photon cannot be reduced further to the linewidth of the pump even when the crystal length is long enough to be smaller than the linewidth of the pump. From figure 3.14 we find the full width at half maximum (FWHM) of the signal and the idler spectrum is 30 nm for L = 1 mm and 4 nm for L = 10 mm. The central wavelengths of signal and idler photons are shown to be following the balanced wavelength equation (refer. 3.7) such as $\lambda_s = 780\ nm$ and $\lambda_i = 842\ nm$. The spectral width (that is FWHM of the spectrum) has meaning in a quantum

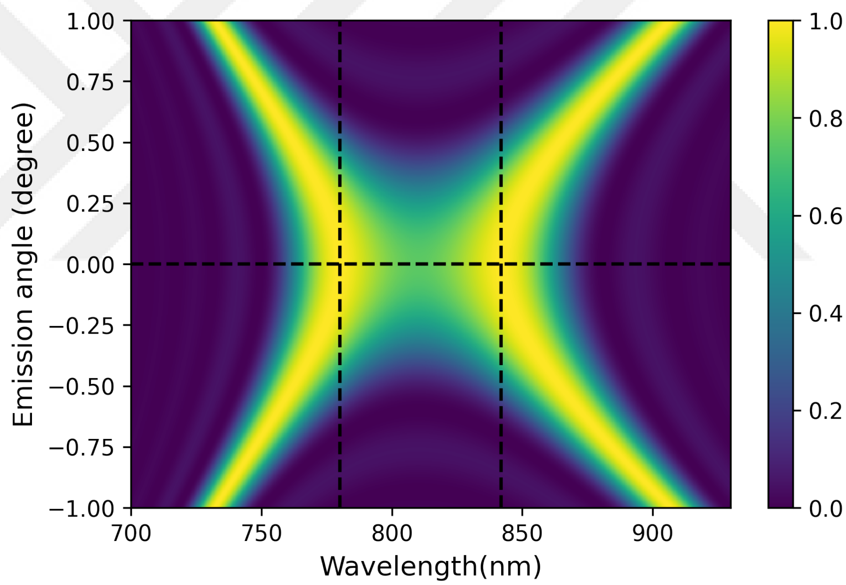

Figure 3.14: Emission angle and wavelength spectrum of signal and idler. Central wavelengths of signal and idler are indicated by the dashed vertical line. The highest intensity of signal and idler are seen when the emission angle is 0°.

imaging application. Although the signal and idler have certain spectral width, each wavelength field in the signal is entangled with its corresponding idler wavelength called frequency entanglement. In a time-resolved quantum imaging scheme, together with spatial correlation, this property can be converted to obtain a Spatio-temporal quantum imaging scheme. A detailed theoretical investigation of Spatio-temporal imaging is given in chapter V. As shown in the figure 3.14, Uniquely to the SPDC, each emission angle bears a different wavelength. This emission angle dependency of wavelength can be translated into a marker for each spatial point. The joint spectrum of the emission angle versus wavelength is useful for frequency entanglement imaging and with its canonically conjugated parameter such as time can be used for spatiotemporal imaging applications.

CHAPTER IV

SIGNAL TO NOISE RATIO IN A QUANTUM SYSTEM

For any classical imaging system, a fundamental limit is inherent that defines how small the noise can be reduced called shot-noise-limit (SNL). The source of this noise is the quantum vacuum fluctuation. This Vacuum fluctuation acts as a noise in the imaging system, affecting the image's quality. In the presence of environmental noise characterizing shot noise is a difficult task. Therefore, typically a source and detection instruments synchronized system is used to show an SNL. In real-world systems, the SNL is rather insignificant as the intensity of the source photon can be increased to improve the SNR of the system. However, in a problem of the detection of a sample in a large noise background is a highly difficult and tried problem. It is well understood that the quantum mechanical correlation can achieve higher SNR levels in a nosy-ridden sample. I show that even with high-noise classical noise, the SNR of quantum detection schemes can still surpass the SNR of classical detection schemes compared to a similar group of the classical method. This is, in general, achieved by incorporating the quantum temporal correlation. In addition, I show that using both temporal and polarization of the SPDC modes can further improve quantum enhancement.

4.1 Shot-noise

4.1.1 Shot-noise in a classical system

Shot noise is a random fluctuation of light photons or other radiation sources. If a photon is generated in the conventional way it has a minimum amount of fluctuation.

By following the statistical method, it is meaningful to quantify the shot-noise by

$$\sigma = \frac{\langle \delta^2 n \rangle}{\langle n \rangle} \tag{4.1}$$

where $\langle \delta^2 n \rangle$ is the variance of the light source with the number of photons 'n' and $\langle n \rangle$ represents the average number of photons generated within the coherence time of the source. Both variance and mean photon numbers are taken in the same unit of time (this time is less than coherence time). With its features such as variance and mean photon statistics, the light source is classified into three categories; Poissonian, super-Poissonian, and sub-Poissonian. Except for sub-Poissonian features, the other two can be explained by the semiclassical model. To explain the sub-Poissonian photon source a quantum mechanical description is needed. Therefore, we can say a light source that exhibits sub-Poissonian photon statics is a quantum light source. The classical light featured with $\langle \delta^2 n \rangle \geq \langle n \rangle$. Hence, the value of σ for any classical light source is bound by $\sigma \geq 1$. Therefore, it is the case that $\sigma = 1$ identifies the classically best possible. Reducing this further needs a quantum mechanical approach. For instance, a sub-Poissonian shows $\langle \delta^2 n \rangle < \langle n \rangle$. The shot noise present in the classical light source can be theoretically modeled using a Poissonian distribution given by

$$P(n) = \frac{\langle n \rangle^n e^{-\langle n \rangle}}{n!} \tag{4.2}$$

we can always see that variance is greater than the average number of photons (i.e, $\langle \delta^2 n \rangle \geq \langle n \rangle$) figure 4.1 shows three values of the average photon number and its corresponding Poissonian distribution. The plots are done assuming the measurement is taken within the coherent time of the light. From the figure and values of variance and average photon number, we can see that the variance $< \delta^2 n >$ is really larger compared to the mean photon number, $< n >$. for instance when the average photon number is 1, the $sigma = 331$. In the large average photon number that is $< n? = 20$ the shot noise is really large; i.e.,$< \delta^2 n >= 37163.36$. So if there is a large

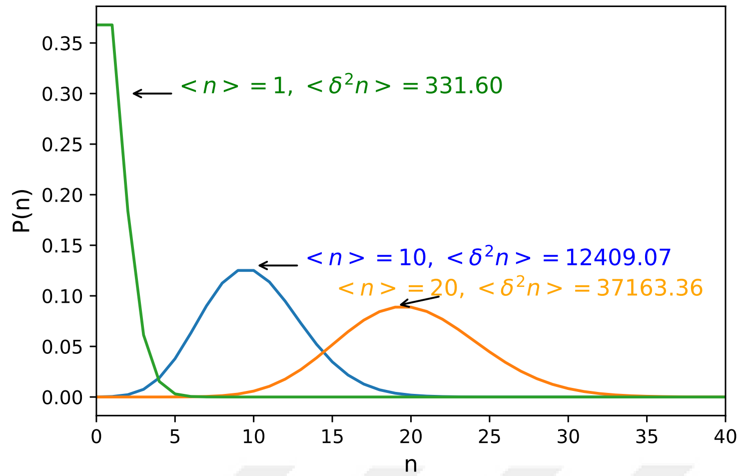

Figure 4.1: Photons' Poisson statistics

average photon number the shot-noise leads to infinity. However, many practical scenarios would not be degraded by the shot noise limit. Because the shot noise would be insignificant as we measured the average photon number and their variance in the different time duration. That case is equivalent to using a high-intensity light field; that is the case in most classical sensing systems such as LIDAR and RADAR. However, having an extremely small intensity light for sensing and imaging is beneficial in imaging a sensitive sample like the biological living sample.

4.1.2 Shot-noise in a quantum system

An experimental approach of sub-Shot noise-limited imaging was first put forward by Brida et al [X]. quantum spatial and temporal correlation in an SPDC source exploited to achieve sub-SNL imaging. Entangled pair photon generated in an SPDC shows a momentum anti-correlation (the detailed description of the momentum anticorrelation is given in chapter V). I.e., when a signal photon is observed at transverse momentum vector with transverse position function q(x, y), its correlated pair (idler) will be observed exactly in anti-position which, in a complex plane representation, can be given as -q(x, y). This implies that one can use idler photon number correlation (therefore intensity correlation) to effectively subtract the noise, and in principle, this can give zero noise objects. With this, equation. 4.1 can be modified into

$$\sigma = \frac{< \delta^2(N_i - N_s) >}{< N_i + N_s >} \tag{4.3}$$

Where N_s and N_i are the numbers of signal and idler photons, respectively. For any classical cases $\sigma \geq 1$ as we have seen in the previous sections. This classical bound is surpassed in quantum number correlation defined by 4.3. In an ideal condition, N_i must equal N_s. This means, with an SPDC source ideal value of $\sigma = 0$ (high correlation) can be achieved; a condition where there is no noise present in the system. However, transmission loss and nonideal efficiency of detectors bring to form a general definition i.e. $\sigma = 1 - \mu$, where μ is the combined transmission and quantum efficiencies of the detectors.

4.2 SNR calculation in the presence of environmental noise

4.2.1 Theory of SNR calculation

If we measure the average photon number in a large time interval (t_{avg}) and variance in a short time interval (t_{var}), ie. $t_{avg} >> t_{var}$, then we can improve the SNR of the system that is otherwise limited by the SNL. Therefore, SNL is not a problem in a high-intensity source-based detection system like LIDAR. To test the quantum benefit when dealing with an environmental-noise-ridden system, I performed an experiment where the source follows the Poissonian statistics. A schematic of the photon detection experiment is given in the figure 4.1. In the experiment, the Time-averaged at 100 ms while photon generation counted with a few microsecond duration. The experiment is carried out for a duration of 900 seconds. An average number of photons is found to be 170.59 for 9000 realizations for one set, shown in figure 4.2. In this scenario, the Poissonian statistics will be approximated to the normal distribution at a large mean number of photons. In such a case the signal-to-noise ratio (SNR) of the system is

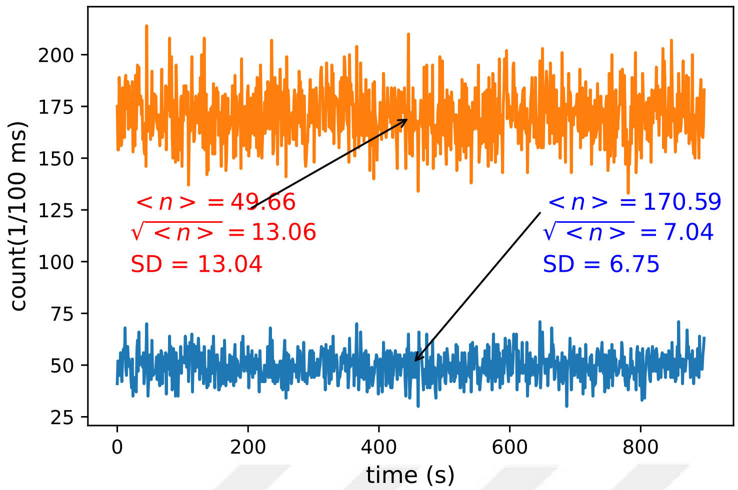

Figure 4.2: Photon fluctuation in different time realization.

given by

$$SNR_{cl} = \frac{N}{\sqrt{N}} = \sqrt{N} \tag{4.4}$$

Equation. 4.4 accounts for only the signal-inflicted noise (shot-noise). As one can intuit from the equation. 4.4, by simply increasing the light intensity (hence the number of photons) the SNR can be increased. In real-world situations, there will be noise from the environment where the system is operated. If we make the measurement in a noisy environment, the fluctuation of the noise limits the SNR. A thermal noise present also has a fluctuation at its mean value and if the environmental noise is too high so the noise fluctuation. That will lead to reduced SNR due to environmental conditions. This case can be mathematically formulated as

$$SNR_{CL} = \frac{N}{\sqrt{N + N_b}} \tag{4.5}$$

where N_b is the external noise count. Following equation. 4.5, if environmental noise, N_b is much greater than the signal (i.e., $N_b >> N$), the detection system's SNR would lead to a point that we cannot differentiate signal from noise. In this kind of system where the intensity mean value is used as the system's figure of merit parameter, to improve the SNR, an alternate way would be to use an SPDC-generated temporally correlated source intensity correlated classical systems. The advantage of using SPDC pair photons coming from the generation time scale is that signal and idler photons are being born of the order of femtosecond, which is experimentally shown to be around 100 fs [42]. This short-time scale allows SPDC-pair photons to remove the noise from the detection scenarios. It is fundamentally because high temporal correlation of the signal-idler photons that cannot be seen in a thermal photon. Unlike a signal-idler photon temporal coincidence, the accidental coincidence happens equally at any resolution bin. This temporal coincidence-based detection scenario follows different SNR formulations. Since coincidence detection is also a large number, its fluctuation is also as much as a classical direct detection scheme. Therefore, similar to the equation 4.5, the SNR for coincidence detection is written as:

$$SNR_{QI} = \frac{C_{s,i}}{\sqrt{C_{s,i} + C_{ac}}} \tag{4.6}$$

where $C_{s,i}$ is the number of signal-idler coincidences (i.e., the number of signal-idler photons that come together within an integration time)and C_{ac} stands for noise enacted accidental coincidence count. The accidental coincidence can be quantified by $N_s N_i \tau$, where N_s and N_i are singles values of signal and idler photons, respectively. As shown in the figure 4.3, the quantum SNR has a high resistance to noise compared to the classical direct detection scheme. The quantum coincidence detection scheme is plotted using the equation.4.6 classical direct detection is plotted using equation4.5 against noise value N_b. For both cases, the number of probe photons (N_s in quantum and N in classical cases) is equal for a fair comparison.

4.2.2 Experimental comparison of classical and quantum SNR

A sketch of the experiment conducted for a comparison of the SNR values of classical and quantum systems is shown in figure 4.4. A vertically polarized (V) pump laser field having a central wavelength of 405 nm and bandwidth of 160 MHz is spectrally cleaned by a bandpass filter of 405 ± 5 nm band property (indicated F1 in the figure).

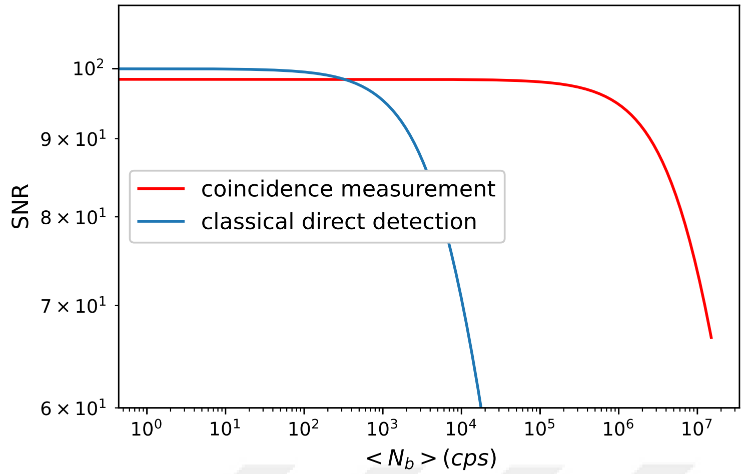

Figure 4.3: The theoretical SNR comparison for coincidence measurement (red solid line) and direct classical system.

The pump is coupled into a single-mode fiber (SMF) for spatial mode cleaning and achieves a Gaussian transverse mode (TM00) pump. The pump is collimated with an aspheric lens (not shown in the figure) and passes normally through a BBO crystal. This type-II BBO crystal has a phasematching angle 28.8°, therefore, a signal and idler having central wavelengths 780 nm and 842 nm are emitted in an SPDC process. The nonlinear crystal is oriented for $V_p \longrightarrow H_s + H_i$. A long pass filter with cut-on wavelength scrapes the pump, thus, only the signal-idler pair photons propagate further from the long pass filter. In a dichroic mirror (DM), the signal and idler are chromatically separated and directly detected by an avalanche single photon detector positioned at each arm separately. Characteristic features of the APDs are given in the table. 3. APD1 is a passively quenched fiber-pigtailed single photon counter and APD2 is an actively quenched single photon detector. External thermal noise is sent only to the APD1 to emulate the detection in a noisy environment. The transistor-transistor logic (TTL) output of each detector is fed into the voltage to digital converted called timestamp unit that records the time of arrival of each photon from each detector. To perform SNR calculation, a noise source is devised to inject into APD1. The noise source is an incandescence lamb having broad spectral bandwidth. When the luminosity of the noise source is high the system is assumed to operate in a large noise environment.

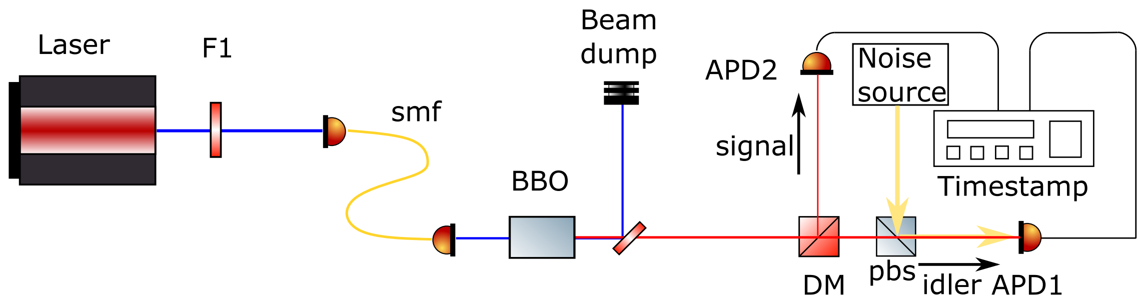

Figure 4.4: Schematic of the experimental setup for comparing classical and quantum SNRs.

Table 3: Characteristic detector parameters of two detectors used in this study.

Parameter	S15	SPCM-AQRH-10
Operating mode	passively quenched	actively quenched
Deadtime	1-2 μs	22 ns
timing jitter	200-600 ps	350 ps
Maximum count rate	450 kHz	17.00 MHz
Efficiency@ 780 nm	60%	59 %
Active area	500 um	160 um

In the experimental settings, the number of photons recorded per 100 ms is monitored in live settings. Since 100 ms time scale is much higher than the coherence time of the photons that is $\sim 70fs$ (linewidth of signal and idler photons are 30 each [74], by following the definition for coherence time, τ_c, $\tau_c = \lambda^2/(c \times \Delta\lambda)$, where c $= 3 \times 10^8$), this is a regime where the shot noise is insignificant. When the signal and idler photons' time of arrival is within the timestamp unit's temporal resolution we consider a coincidence detection ($C_{s,i}$). The timestamp unit has a temporal resolution of $\sim 81ps$. In noise-free settings, the coincidence value is 5.2 k counts per second (cps) when the pump power is $100\mu W$. At the same time, the singles values of the signal arm (take it as channel 1) and the idler arm (take it as channel 2) are about 59 kcps and 120 kcps, respectively. As channel 2 receives intentionally injected noise photons, the average

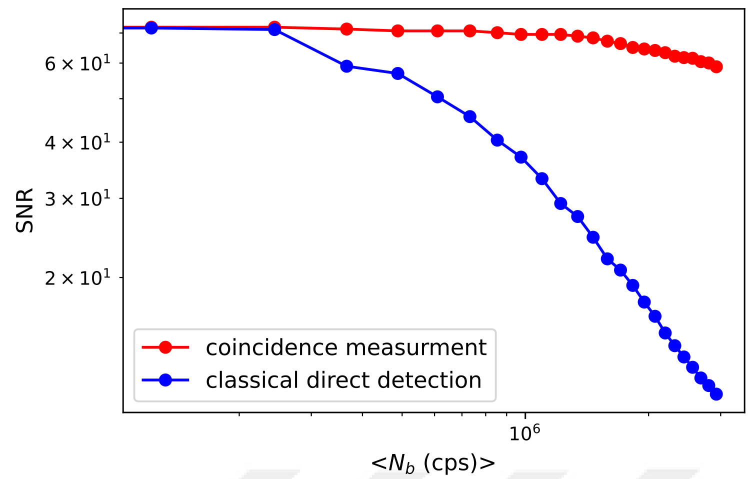

Figure 4.5: Experimental SNR values of classical direct detection and quantum coincidence detection schemes in various noise values.

value of the singles detected by APD2 can be taken as a classical number of photons send to prob a sample and its fluctuation is the noise. The noise is increased in a step-by-step process and recorded both the average photon number and its variance (variance is $\sqrt{N}$ since the system operates in a large photon regime as described in the previous sections) from the mean value. It should be noted that since the value of the single always read greater than the coincidence events count due to detectors efficiencies and other losses in the system, in an external noise-free condition, the SNR values for a classical case are favorable to the classical system. We have normalized the SNR values calculated in both classical and quantum systems using equations 4.4 (classical) and 4.6 (quantum) to have a fair comparison between the two. Then the noise stream increased and tabulated the SNR for all cases. The results are plotted in the figure 4.5. By increasing noise values, both cases were shown to have decreased the SNR. The rate of change of the Quantum SNR (SNR_{QI}) is much smaller than the SNR_{CI}; that is quantum system is more immune to noise. In the noise-free case the SNR was calculated to be 72±4 each. Subsequently, we see $SNR_{QI} >> SNR_{CI}$ case when the noise value goes above 2.9 million cps. Absolute values of SNRs are 11.00±2 and 58.87±3 for classical and quantum cases, respectively. It concludes that at extreme noise conditions, the quantum system showed improved performance with an enhancement factor of 5.35 (7.28 dB).

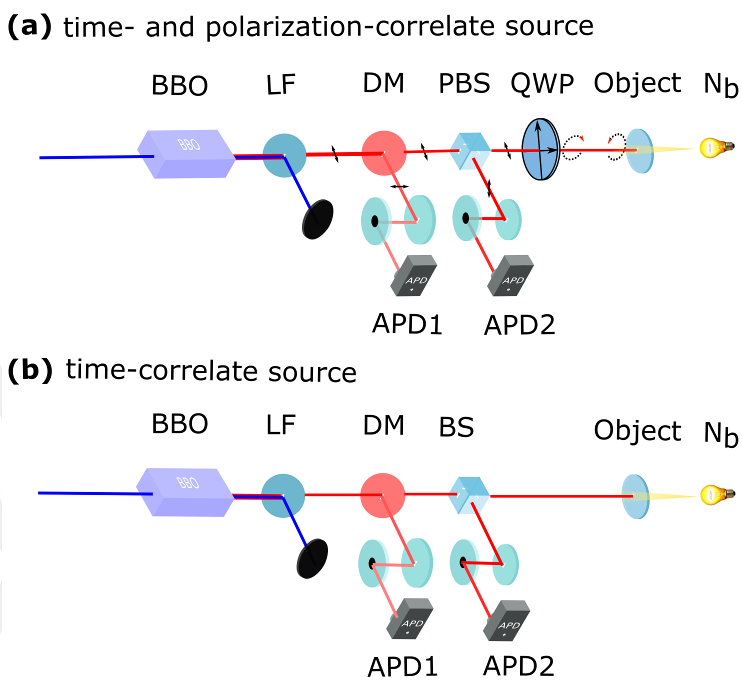

Figure 4.6: The experimental arrangement used for testing the detection schemes that use (a) time and polarization correlations and (b) only time correlations. BBO: beta barium borate, LF: long-pass filter, DM: dichroic mirror, PBS: polarizing beam splitter, QWP: quarter wave plate, BS: beam splitter, APD1-2: avalanche photo-detector 1-2.

4.3 Polarization correlation for SNR enhancement

4.3.1 Experimental setup

In the previous section, we used only a time-bin correlation of the SPDC source for comparing the SNRs of the quantum and classical systems. In this section, the readily available polarization correlation of the signal and idler photons is used for further improvement of the SNR. For a comparison of an only time-correlated (TC) quantum system with a time and polarization correlated (TPC), I have used two different experimental schemes. A schematic of the experimental setups used for this study is shown in figure 4.6. Refer to figure 4.6 (a) for TPC settings and figure

4.6 (b) for TC. Every pump parameters and nonlinear crystal features are the same in this experiment with the section 4.2.2. The signal photons are directly measured with the first avalanche photo-detector (APD1) while the idler photons pass through a polarizing beam splitter (PBS) and a quarter-wave plate (QWP) before it reflect back from the mirror (see in figure 4.6 (a)). The horizontally polarized signal photons become right-hand circularly (RHC) polarized at QWP in the forward path and return by left-hand circularly (LHC) polarized after being reflected back by the mirror. In the return path, the LHC signal photons become vertically polarized after the QWP consequently reflects at the PBS and is detected by the APD2. In the only time-correlated case, which is shown in figure 4.6 (b), the signal photons are transmitted from the dichroic mirror and then half of the photons pass through a beam splitter. Half of the back-reflected signal photons are reflected towards the APD at the beam splitter (BS). However, for a fair comparison, the source intensity in the TC case is increased to obtain the same number of pair sources for both the TC and the TPC cases. The outputs of two APDs are fed into a timestamp unit (not shown in figure 4.6) where the timing information of signals is recorded. An unpolarized incandescent lamp with a broad spectral band serves as a source of noise (N_b), injecting N_b into the system allowing us to study its performance in the presence of background noise. In our settings, the quantum state of polarization of the signal and reference photons are $|H_s\rangle$ and $|H_i\rangle$, where H indicates the horizontal polarization. The polarization of the signal photons is flipped 90° in figure 4.6 (a) before detection at APD2, and turn the combined state of polarization into $|V_s\rangle$ and $|H_i\rangle$, where V refers to the vertical polarization. First, we used an anodized aluminum (reflectance is 0.13 ± 0.03 [91]) as a target object to test if the detection is possible and the polarization correlation of the source is maintained after scattering from a rough surface. Therefore, some amount of polarization state will be sacrificed even in specular reflection [123, 124]. As a result, the probability of detection of returned signal photons is extremely low. However, we have detected a signal-idler coincidence of 200 ± 10 cps when the target is positioned closer (10 cm) to the transmitter (distance between the PBS and the object that is shown in figure 4.6 when the pump power is 128 µW). The anodized aluminium is later replaced with a semitransparent mirror as a target object to allow the injection of noise photons externally. An incandescent lamp was used as a power-tunable broadband unpolarized thermal source to inject noise. Using a broadband source device to replicate a more realistic case where spectral filtering cannot extinguish the noise. Moreover, such a thermal light source acts as a proper noise model in a correlation-based detection scheme since it shows high classical correlations [36]. The noise is unpolarized, which makes it a difficult scenario to filter out the noise from the signal not only in the presence of only temporal correlations between the signal and reference photons but even in the presence of polarization correlations. Here, the temporal correlation refers to the fact that both the signal and reference photons are generated almost simultaneously.

4.3.2 Second order correlation function

In the experimental setup, we use only phase-insensitive quantum correlation, where the idler arm has an extra delay with respect to the signal arm. The SNR enhancement in a quantum system comes from the classically unachievable correlation of the quantum system. Therefore, it is meaningful to compare the correlation of the TC and TPC with an appropriate correlation parameter. The second-order correlation function denoted by $g^{(2)}(\tau)$ can quantify the correlation of two photons. For instance, the maximum value that can be achieved by a classical system is shown by Brown, R. Hanbury and Twiss (HBT) [125, 126]. The HBT experiment showed that the maximum $g^{(2)}(\tau)$ can be achieved by using a bunched light source is $g^{(2)}(\tau) = 2$. The single-photon level quantum correlation of the signal-idler photons can show $g^{(2)}(\tau) > 2$. Therefore, the first aim is to show how the second-order correlation changes with respect to noise in the environment.

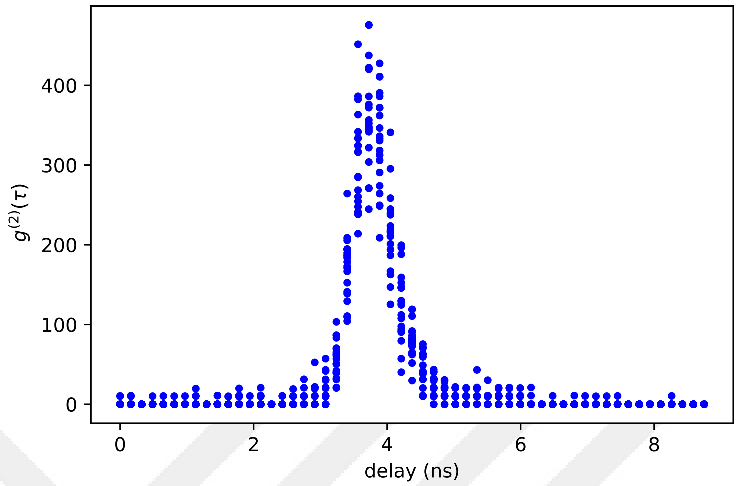

Figure 4.7: The $g^{(2)}$ distribution over a range of temporal displacement for 63 ms data for each with no noise scenario.

In the experiment described in the section. 4.2.2, the timestamp unit is configured to search for the joint arrival of photons from both APDs. If the signal and reference photons statistically coincide at a certain delay between them, it appears on the cross-correlogram. The coherence time of the SPDC photons is approximately 1.5 ps. In our settings, the idler photons travel approximately 1.2 m extra path, so a coincidence is not expected even though both photon pairs are created together within the 81 ps (timestamp unit's resolution). To obtain a coincidence in this case, we scan the bin width until an avalanche of coincidence is observed (due to this reason temporal correlation is called time-bin entanglement). We observe a coincidence peak when the bin width is 21 (which is equivalent to 3880 ps coincidence window). Figure 4.7 shows the $g^{(2)}$ distribution for a range of temporal delays, and from this, the peak at the 3880 ps delay line can be observed. The coincidence value in the $g^{(2)}$ plot is maximum at $\tau = 3880$ ps and $g^{(2)} \rightarrow 1$ when $\tau \rightarrow \infty$. In our experimental configuration, the maximum coincidence value observed, when the pump power is set to 126 µW, is 5300 ± 100 pairs per second with noise-free settings. We lose some pairs due to the losses in the system and the non-unitary reflection coefficient of the object.

The coincidence values are set approximately the same for both TC and TPC (figure 4.6) by adjusting the pump power to make a reasonable comparison. To quantify the quantum correlation exploited by the experimental setup, we estimate $g^{(2)}$ value from the observed coincidence and singles values of the signal and reference. The suitable definition of $g^{(2)}$ for our type of system is identified to be [92, 127, 128, 129]

$$g^{(2)}(\tau) = \frac{C(\tau)}{N_s N_i \Delta t T} \tag{4.7}$$

where $C(\tau)$ is the coincidence events of signal and reference photons (no accidental coincidence) as a function of time delay τ between the signal and reference photons per temporal resolution Δt of the timestamp unit, T the time duration of the measurements ($T = 1$ s), and N_s and N_i are the detection events per second for the signal and reference photons, respectively. The maximum $g^{(2)}$ value for the case of TC and TPC in a noise-free condition is calculated, from our measurements, to be 260 ± 16.1 and 261 ± 16.2, respectively. In the noise-free settings, singles values are $N_i = 99$ k counts/s and $N_s = 53$ k counts/s for TC and those are $N_i = 100.5$ k counts/s and $N_s = 52$ k counts/s for TPC settings. The noise-free values are obtained by blocking the signal photons before PBS and recording the noise values (singles and coincidence events) and subtracting these when the signal photons are sent to the target with the recorded coincidence and singles events. The Δt value is 3880 ps for both cases. By increasing the noise level, a dramatic reduction in the $g^{(2)}$ value for both cases is observed. However, in the TPC case, the reduction is two times less.

4.3.3 SNR comparison for TC and TPC systems

The factor $N_s N_i \Delta t T$ in equation 4.7 is a direct measure of the accidental coincidence (the accidental coincidence is linearly proportional to the noise). In our experiments, the accidental coincidences are measured by looking at the coincidence values of APD1 and APD2 when the signal arm is blocked effectively allowing only the noise photons to be detected by APD2. To incorporate the noise parameter, the equation 4.7 can

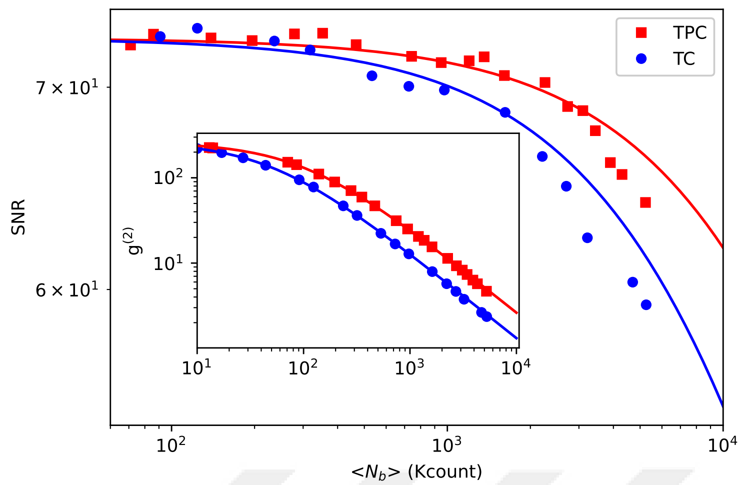

Figure 4.8: The measured signal-to-noise ratio (SNR) versus the injected noise N_b is plotted for time correlation (TC) (blue dots) and time and polarization correlation (TPC) (red dots) schemes. The theoretical fit (solid lines) is made by using equation 2. The $g^{(2)}$ trend for different noise conditions for both TPC and TC are shown in the inset.

be modified to

$$g^{(2)} = \begin{cases} \frac{C(\tau)}{N_s(N_i+N_b)\Delta t T} & \text{for TPC setting} \\ \\ \frac{C(\tau)}{N_s(N_i+2N_b)\Delta t T} & \text{for the TC setting} \end{cases} \tag{4.8}$$

where N_b is the noise count. Theoretically, the $g^{(2)}$ enhancement due to additional polarization correlation is limited to 2. Because the total noise sent to the system is divided into two at PBS (since noise is unpolarized) in the case of TPC. Thus, only 50% of the noise arrives at the detector. In the case of TC, 100% of the noise reaches the detector (in our case APD2). This shows theoretically it is possible to improve the $g^{(2)}$ by a factor of 2 by adding polarization correlation in addition to the temporal ones. Experimentally, the TPC enhancement (the ratio of the $g^{(2)}$ in TPC case to TC cases) is found to be fixed and it is approximately 1.99 ± 0.08 when detectors are operating in the linear region.

The absolute value of SNR is related to but not equal to $g^{(2)}$ values. Therefore, we have tested the SNR of the system by following the previous work [130]. We can formulate the SNR by considering the fluctuations of the signal and noise (imposed by the shot noise limit). In normal intensity-based detection, the shot noise limited SNR is SNR $= \sqrt{N}$, where N is the number of photons. In a coincidence-based detection scheme, the SNR can be simplified into $\sqrt{C}$. This means the fluctuation of the coincidence value will reduce the SNR. This effect can be observed in figure 4.7. In our case, we are sending an external noise to test the system behaviour in a different noise condition. Hence, we formulate the SNR as following

$$\mathrm{SNR} = \begin{cases} \frac{C(\tau)}{\sqrt{C(\tau)+N_r(N_s+N_b)\Delta t T}} & \text{for TPC setting} \\ \\ \frac{C(\tau)}{\sqrt{C(\tau)+N_r(N_s+2N_b)\Delta t T}} & \text{for TC setting} \end{cases} \tag{4.9}$$

By consistently increasing the amount of injected noise, we calculated the SNR values. Figure 4.8 shows theoretical and experimental SNR trend for both TC and TPC values. With noise, a proportional drop in the SNR values are observed for both TC and TPC settings, with TPC having less decrease compared to TC. An enhancement of approximately 3 dB (SNR of TPC/ SNR of TC) is observed when the noise is 1 million counts/s. This is intuitive as the TPC system reduces the noise by half.

4.4 Detector characteristics

4.4.1 Count rate dependent detector efficiency

APD's characteristics play an important role in the performance of the quantum detection scheme. Mainly because the measured real photon coincidences (signal-idler coincidences) are reduced by the photon count-dependent efficiency of the detectors. A most popular detector manufactured by Exceltis.inc with model number SPCM-AQRH-10 is used as a testing detector to characterize count-rate dependent SNR values of the quantum detection scheme. The salient features of this detector are given in the table. 3. Figure 4.9 shows the APD's output (as photon counts in the

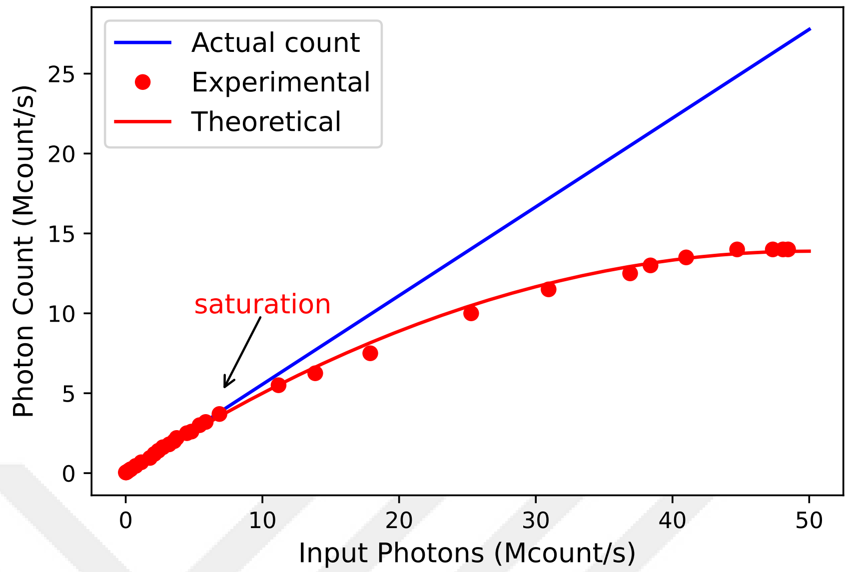

Figure 4.9: Photon count rate versus the input photon rate. Red dots are experimentally-obtained photon count rate at the detector. A power meter value converted into photon number gives rise to the input photons count.

figure) for the various input photons. The experimental results (doted points) show a linear trend when less number of photons are sent and it started detecting fewer photons at the onset of saturation (indicated saturation in Figure 4.9). The number of photons detected is getting reduced until the maximum count rate is achieved. After the maximum count rate, there is no photons are detected (not sown in the figure). The solid line (blue) is an estimated plot considering APD behaves the same regardless of the input value (called actual count). This characteristic feature of the detector is rooted in the electronic circuitry of the detector mechanism and mainly the dead time of the detector resetting in detector dynamics. This behaviour can be modeled by correction factor given by

$$\mu = 1/(1 - AV \times t_d) \tag{4.10}$$

where μ is the detector correction factor, AV is observed photon count rate and t_d is the dead time of the detector. This is consistent with previous work [131], and we observe that the correction factor is the inverse of the effective duty cycle as described by [131]. We have calibrated the APD and its correction factor for various input photon counts is given in 4.10. The figure shows that if the noise level (input photons in the figure)is high, the detector gives an imprecise value defined by the correction factors. That means if we do not account for the detector's characteristics, the actual visibility will be miscalculated. It should be reminded that by multiplying the observed value with the correction factor one can see the actual count rate as seen in the actual count rate given in the figure 4.10. The figure clearly accounts for count rate-dependent efficiency.

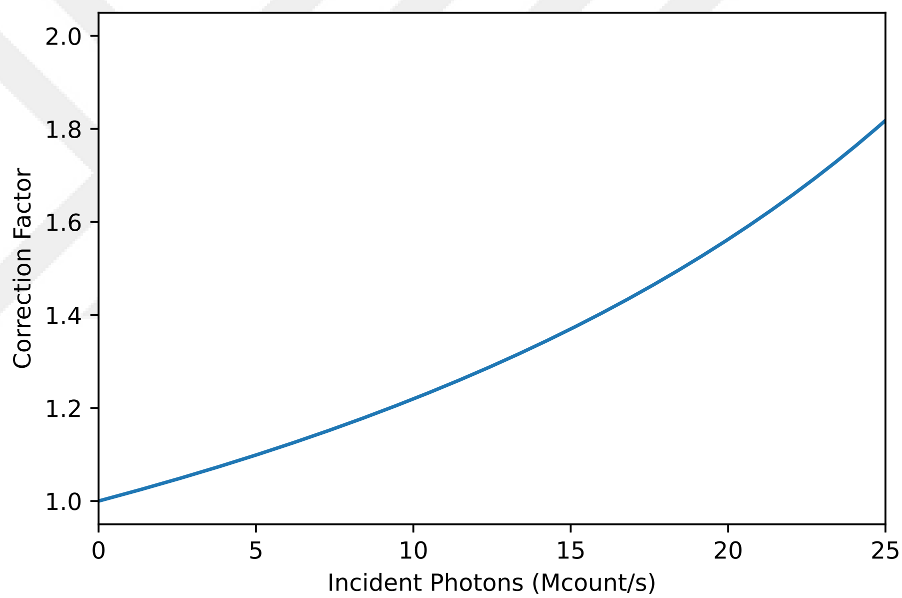

Figure 4.10: The correction factor versus the incident photon rate.

4.4.2 Correcting detector deficiency

The count rate-dependent detector efficiency can influence the sensing system when it operates in a noisy background. In the experiment for TPC (figure 4.2.2 (b)), the intensity of the transmitted signal is constant and the noise is increased to test for the system's behavior in different noise (N_b) conditions. Since the accidental coincidence is a function of the noise, defined by $C_{\mathrm{ac}} = (N+N_b)N_i\tau$, it also follows the trend of N_b. Therefore, one can assume that this high noise can affect the SNR of the measurement

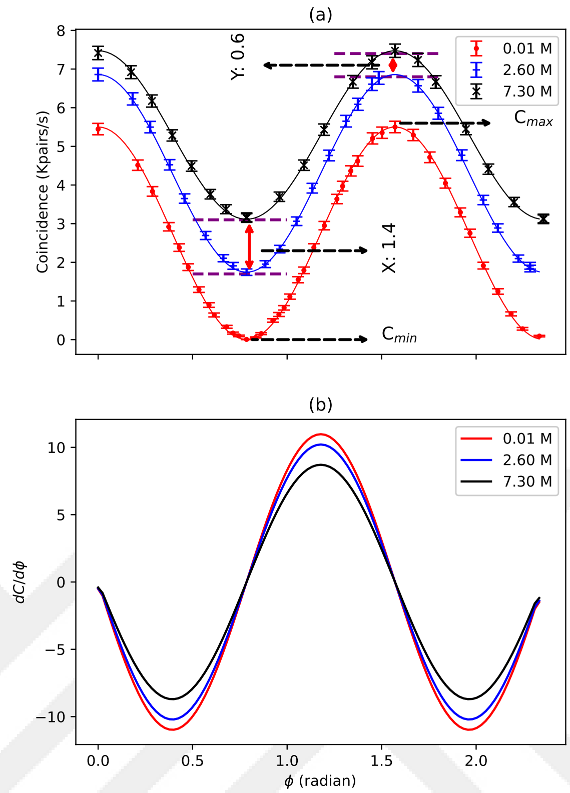

Figure 4.11: (a) Coincidence value showing a sinusoidal trend while rotating the quarter wave plate, which effectively controls the amount of detected signal that is reflected from the object. This behavior is observed only from the polarized signal photons (since the noise is unpolarized). The increased level of noise rises the floor height of the sinusoidal plots (minimum coincidence value is not zero). Therefore, floor height gives rise to the estimation of accidental coincidence. The error bars are obtained by assuming the photon fluctuates by $\sqrt{N}$. Solid lines represent theoretical fit. (b) Derivative of (a) with respect to ϕ.

system. The polarization correlation between the signal and the idler arm, in addition to the temporal correlations, provides distinguishability of signal-idler photons and idler-noise photons coincidences (separating actual and accidental coincidence). Also, it allows estimating how much reduction in the detection of signal-reference photons correlation when detectors are operating in the saturation region. Thus, the TPC scenario is used for investigating count rate-influenced performance degradation of the system. Figure 4.11 shows a sinusoidal behavior of the reflected light from the object due to the polarization correlations between the signal and idler photons.

The plot shifts upward in accordance with the increasing noise. This is realized by rotating the quarter-wave plate in the TPC experiment. A combination of PBS and the QWP (see figure 4.6) ensures that only 90°-rotated vertical linearly polarized light is detected with the APD2. In this regard, rotating the QWP in the optical axis and evaluating the change in the coincidence detection allow differentiating the signal from the noise (hence the accidental coincidence). The magnitude of the sinusoidal plots is $C_{\max} - C_{\min}$, where $C_{\max}$ and $C_{\min}$ are the measure of the coincidence when both the signal and the reference photons are present and only the noise is present cases, respectively (see figure 4.11 (a)). The magnitude reduces as the level of photons detected is reaching the saturation region of the detectors. This behavior is attributed to the APDs' functional limitations when they operate near the saturation region. To be specific, the detectors will not sense correlated photons efficiently due to their inability to reset themselves fast enough when more photons are present [131]. Therefore, the value of signal-idler photons coincidence reduces when the system is operating in the saturation region. Using the polarization correlation allows us to estimate the reduction in the signal-reference photon correlation. From figure 4.11 (a), when the system shifted operating from 2.60 million noise levels to 7.3 million photons, the reduction of signal-reference photons is 0.8 k coincidences/s (difference of "X" and "Y" values in figure 4.11 (a)). Figure 4.11 (b) shows the derivative of the coincidence with respect to the angle of the QWP. Ideally (without detector saturation effect) three plots in figure 4.11 (b) should overlap.

The control of the number of signal photons in the TPC system opens up a new way of estimating the presence of noise, leading to the possibility of further noise rejection. In this context, we introduce a figure of merit parameter called visibility that can be defined as

$$V = \frac{C_{\max} - C_{\min}}{C_{\max} + C_{\min}} \tag{4.11}$$

In the absence of background noise, $C_{\min}$ becomes zero leading to the visibility

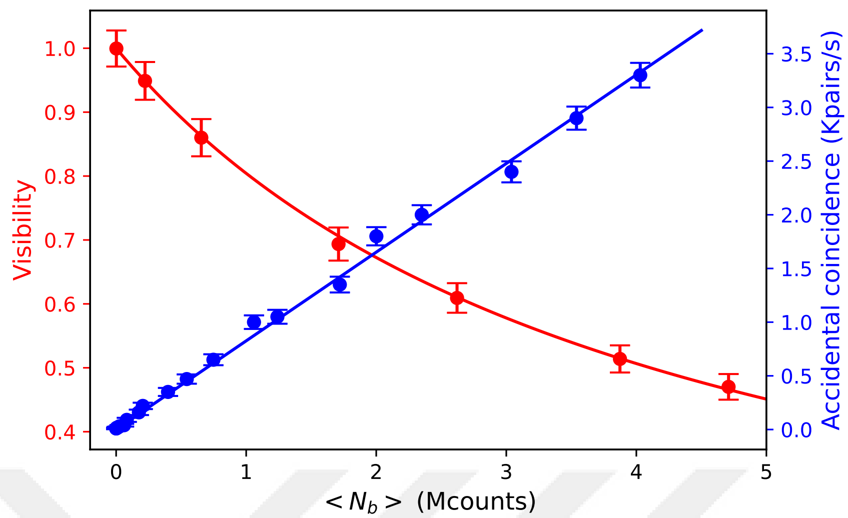

Figure 4.12: Demonstrating the variation of visibility with respect to the average noise (red). The accidental coincidence increases linearly with the external noise (blue). Points represent the experimental data and the solid lines represent the theoretical fit using the equation 4.11. Error bars in the accidental coincidence are the order of $\sqrt{N}$. The error in the visibility is calculated by following the standard error propagation method.

value being unity. An estimation of visibility over accidental coincidence is plotted in figure 4.12. In practical settings, the C_{max} is the summation of the coincidence between the signal and idler and the accidental coincidence. Therefore, the maximum observed coincidence value can be rewritten as $C_{\text{max}} = C + C_{\text{ac}}$, where C_{ac} is the accidental coincidence. C_{min} can be equate to the accidental coincidence. After incorporating this information, equation 4.11 can be rewritten as

$$V = \frac{C + C_{\text{ac}} - C_{\text{ac}}}{C + C_{\text{ac}} + C_{\text{ac}}} \tag{4.12}$$

which turns into,

$$V = \frac{C}{C + 2C_{\text{ac}}}. \tag{4.13}$$

From the previous section 4.4.1, we learned that APDs do not give actual photon count it encounters above the threshold. The relation between visibility and accidental coincidence can be estimated by following the relation:

$$V = \frac{C}{C + 2C_{\mathrm{ac}}\mu} \tag{4.14}$$

where C_{ac} is the accidental coincidence and μ the detector's correction factor. The μ parameter is substituted to the equation to address the change in visibility value due to the detector's operational change in detection rates close to its saturation. The deduced equation fits with experimental data as shown in figure 4.12. The derived expression is suitable and useful for finding the visibility value irrespective of the detectors' characteristic limitations. Previous study shows that the visibility of the single photon detector is highly dependent on the detector saturation [131] i.e. if the detectors are operating in near or deep saturation region the actual visibility will be miscalculated. The derived expression for the visibility is applicable in any situation. Because the saturation of the detector is guided by the dead time of the detector. In the given expression dead time of the detector is normalized. This calculation will prevent misleading conclusions based on constraints from the detector's internal electronics circuitry in QI detection schemes.

CHAPTER V

CORRELATION BASED 2D QUANTUM IMAGING

Simultaneous quantum correlation of position (due to momentum correlation) and time offer a versatile imaging system that is impossible by conventional methods. As SPDC-generated signal-idler photons exhibit time-position correlation, it is a suitable candidate for the practical demonstration of a time-position correlation-based imaging scheme. In practical settings, this kind of imaging system means a knowledge of the position of one particle at a certain time allows one to determine the position of its entangled pair at that time. Therefore, it allows illuminating the sample under investigation by one type of particle and detection by other. Compared to conventional imaging, quantum imaging benefits from improved signal-to-noise ratio in large noise backgrounds, sub-SNL imaging, image reconstruction by a minimal amount of photons, and illumination by one frequency of light and detection by a different frequency thereby allowing efficient covert imaging. This chapter discusses a quantum imaging scheme that is constructed by nondegenerate SPDC photon pairs as a driving source. An experimental setting is demonstrated and a theoretical model is rigorously treated to test suitable conditions for the quantum imaging system.

5.1 *Experimental setup and data processing*

A schematic of the experimental setup used for this study is shown in figure 5.1. A vertically polarized pump laser having a wavelength 405 $\pm$0.0000875 nm and spatial profile of TM00 and waist size of 610 $\pm$ 10 um interacts with a 4 mm long BBO crystal that is cut at 28.80°. As a result, in an SPDC process, nondegenerate and horizontally polarized signal and idler photons of central wavelengths 780 nm and

842 nm, respectively are generated. The pump field is removed from the system by using a long-pass filter having a cut-on wavelength at 750 nm (not shown in the figure). A lens of focal length 50 mm collimates the signal and idler and subsequently, they are separated by a dichroic mirror which has a cut-on wavelength at 800 nm. The subsequent choice of lens configurations was chosen to maintain an equal optical travel distance for the signal and idler photons (600 mm) between the BBO crystal and the ICCD camera (PI-Max3), thus providing an efficient system for near-field imaging. Values of focal lengths of the lenses are given in the appropriate places in figure 5.1. The signal's spatial mode is projected on the sample located at the image plane. Then, the image plane is projected on the ICCD camera with a 4f lens arrangement. In the signal arm, there is only one lens with a focal length of f = 250 mm. A half waveplate (HWP) is positioned at the idler arm such that horizontally polarized light becomes vertical one for directing them to the ICCD camera via PBS. Two different bandpass filters, which have central wavelengths of 780 ± 10 nm and 840 ± 10 nm in the signal and idler path respectively, are placed in each arm to filter out the noise. Here, the object is a tweezer that was readily available at the lab. A tweezer does not make a suitable object to learn the system's resolution- this choice of object is purely driven by the best possible object available at the lab.

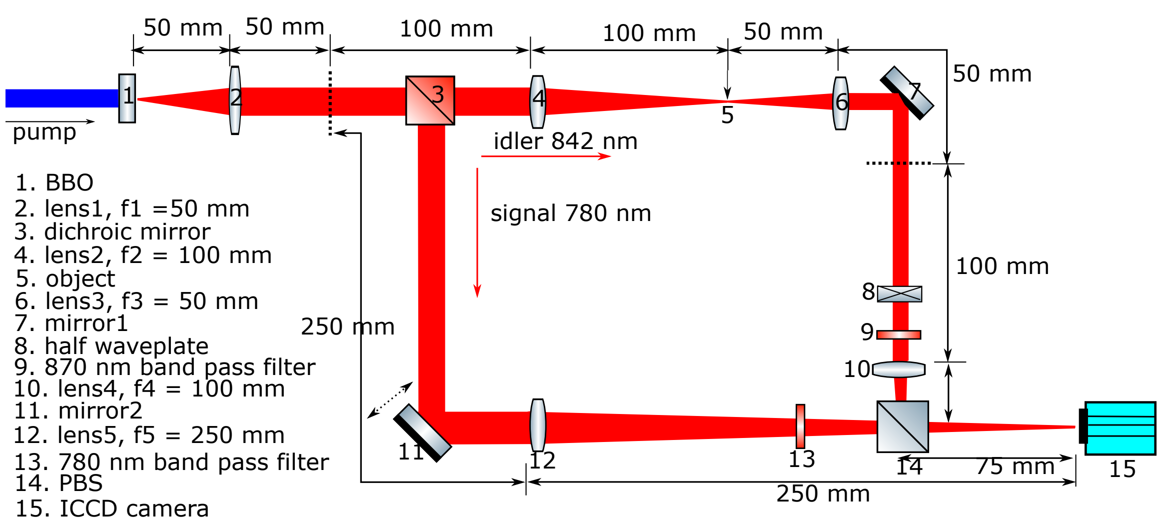

Figure 5.1: Experimental setup used for correlation-based quantum imaging.

In the experimental setup shown in figure 5.1, the signal arm never interacts with the object understudy. The idler arm transmits its spatial structure through the object and projects it on the ICCD camera. If the signal arm is blocked we can observe a clear almost no external noise contained images as shown in figure 5.3 (a). Figure 5.3 (a) is our reference for the structure of the object. The signal photons, which never interacted with the object, act as noise in classical imaging settings (classical imaging setup where intensity value on each pixel location is combined to form an image). With both signal and idler projected on the camera, the system can be assumed as a classical imaging system operating in a noisy environment. The observed image in this setting can be seen in figure 5.3 (b). To perform a quantum imaging scheme, there are some conditions to be satisfied. Firstly, Since our ICCD's pixel resolution is 26 um X 26 um, but the correlation calculated for 4 mm BBO is $\sim$ 10.8 um, we need to shift the camera away from the imaging plane to make a case at which the spatial correlation factor $\sigma(z) > 26um$. This requirement conditions the number of spatial modes should be larger than the total number of pixels used for imaging. With 4 mm BBO crystal used the spatial correlation is $\sim$ 10.8 um, therefore the number of spatial modes equals 2670 (the procedure to calculate the number of spatial modes and spatial correlation is given in the upcoming sections). We have selected 59 horizontal and 50 vertical pixels in ICCD which can accommodate the full 2950 spatial modes. As our ICCD camera is not designed for intensity correlation-based (due to number correlation) imaging, we have to record the data for a longer time to follow the position correlation detection algorithm that will be discussed in the upcoming part. Readers can see the important specifications of the ICCD camera used for this study from table 4.

As seen from table 4 and figure 5.2, the quantum efficiency of our ICCD camera at 842 nm wavelength is very low ($\sim$ 2). Therefore, to see some spatial correlation it is important to take millions of frames and process them. Therefore, the post-processing

Table 4: Features of Pi-Max3 camera.

Feature	Value
Efficiency@840	2%
Internal timing frequency	1 MHz
Spatial resolution (pixel size)	26um X 26um
Spatial resolution	26um X 26um
Dark current @ -25°C (typical)	4 e-/p/sec
Full-field	1024 x 255 pixels
Frame rate at full frame	6.21 fps

will take computational time as each pixel from each frame should be individually analyzed and processed. Fortunately, the area of SPDC mode is low and it takes only 59x 50 pixel arrays. Thus, the frame rate can be improved substantially compared to the full frame operation of the ICCD. With the above-mentioned number of pixels selected, the ICCD camera offers a frame rate of 18 fps.

As we aim to record $\sim$ 1 million frames, the system ran for about 16 hours for data collection. The full recorded data takes the memory of $\sim$ 300GB. We have followed a standard correlation finding algorithm [99, 31, 132] in a noisy to observe the spatial correlation of the signal and idler pairs, that is

$$< I_s(x,y)I_i(x,y) >= \frac{1}{N}\Sigma_{n=1}^{N}(I_n(c) \times I_n - I_n(c) \times I_{n+1}), \tag{5.1}$$

where $< I_s(x,y)I_i(x,y) >$ is the intensity correlation of the signal and idler photons, N is the total number of frames, n represents the index value of each frame and c indicates a specific pixel on the camera we chose to look for its correlated counterpart. To implement the algorithm given by equation 5.1, it is easier to convert each fame

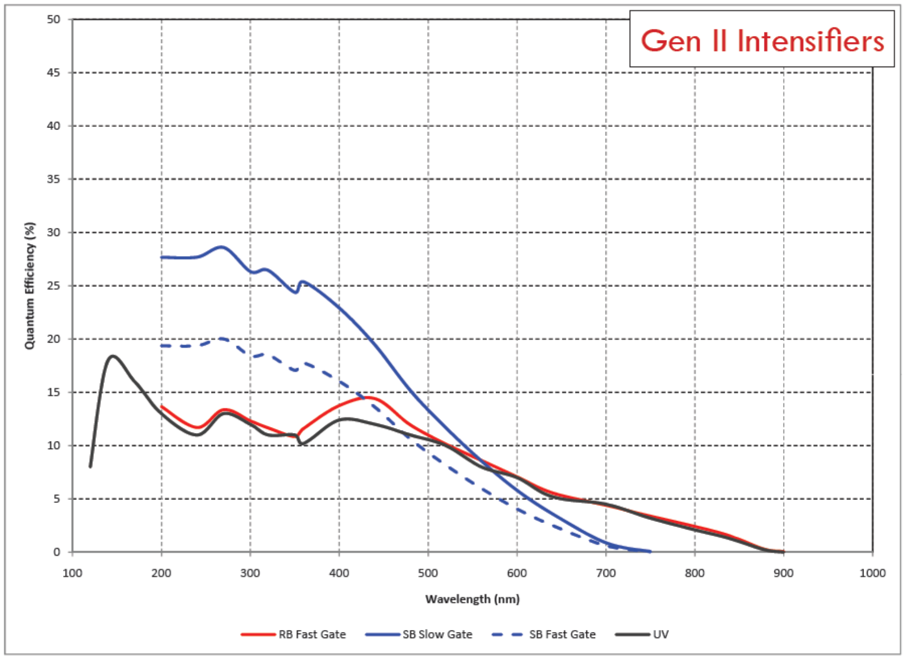

Figure 5.2: Quantum efficiency of the ICCD camera used for this study. The ICCD camera is designed for RB fast gated operation.

in a matrix format such as

$$I_n = \begin{pmatrix} a_{1,1} & a_{1,2} & a_{1,3} & . & . & . & a_{1,j} \\ a_{2,1} & a_{2,2} & a_{2,3} & . & . & . & a_{2,j} \\ a_{3,1} & a_{3,2} & a_{3,3} & . & . & . & a_{3,j} \\ . & . & . & . & . & . & . \\ . & . & . & . & . & . & . \\ . & . & . & . & . & . & . \\ a_{i,1} & a_{i,2} & a_{i,3} & . & . & . & a_{i,j} \end{pmatrix}_n \tag{5.2}$$

Each element in the matrix 5.2 equates to each pixel on the ICCD. We have taken index i as vertical pixel arrays and j as a horizontal one. Therefore, we can realize the array of pixels recorded has a matrix shape $i \times j = 59 \times 50$ and remember $i \neq j$. In equation 5.1, $I(c)_n$ can be any specific single pixel at the n-th frame, let's pick pixel index for c as $c = l, m$, where l and m are specific pixel position in the camera. To implement the first part of the equation 5.1 ie., $I(c) \times I_n$, we can perform $a_{l,m} \times I_n$

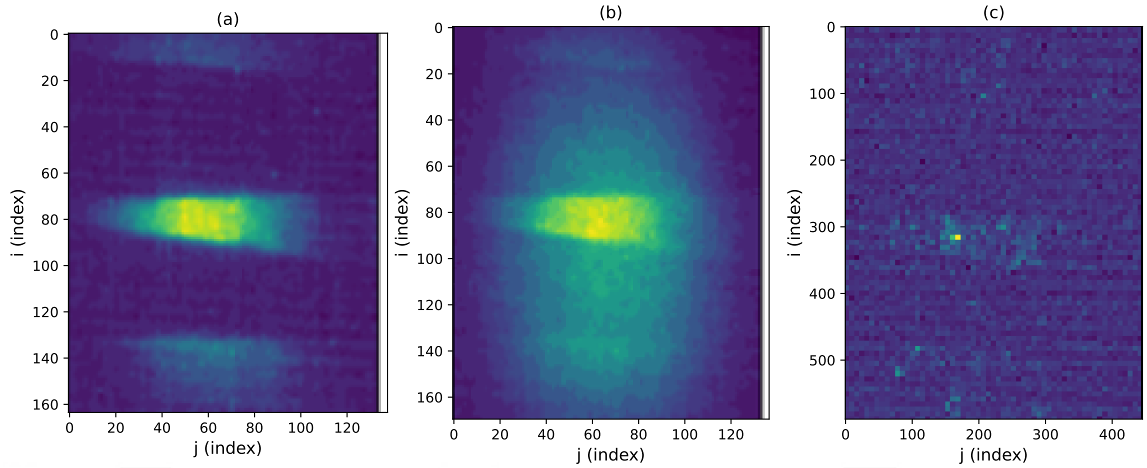

Figure 5.3: The image of the sample under (a) noise-free classical imaging (b) noisy classical imaging (c) noisy imaging with quantum correlation method for the same sample.

and obtain a new matrix of the same dimension. Note that by doing $a_{l,m} \times I_n$, if our system operates in a noise-free condition and the camera frame rate is of the order of SPDC emission rate, we can observe a signal photon and its correlated pair in a single frame (two photons detected symmetrically opposite pixel position). Therefore, the first part of equation 5.1 represents the real coincidence (signal and idler coincidence detection). As even advanced ICCD or EMCCD cameras do not have the capability of the frame rate of the order of photon rate, we need to perform the algorithm given by equation 5.1. The second part of the equation 5.1 helps us to subtract the noise. When we inspect, one can understand that the second part of the equation represents the accidental coincidence as by doing $I_n(c) \times I_{n+1}$ we are actually multiplying a pixel value from a frame with the adjacent next frame values. To summarise, equation 5.1 gives rise to actual coincidence with noise coincidences subtracted. As our frame rate is only 18 fps, we notice that the explained procedure has to be done several times to observe a meaningful result.

By applying this correlation detection algorithm to the recorded data, we have obtained a quantum image as seen in figure 5.3 (c). The result shows an image of a tweezer object used for our experiment- confirming our experimental setup is feasible for producing a correlation-based image reconstruction. However, the quality of the image produced by our quantum method is very poor. We assume the camera's undesirable specification, specifically the efficiency of $\sim 2\%$, is the reason for this. Typically, in this kind of imaging, EMCCD is recommended as it provides high quantum efficiencies ($\sim 95\%$) compared to the ICCD camera. However, ICCD cameras in general benefit from a reduced dark count rate in addition to the opportunity to operate in a gated mode for efficient noise subtraction. Also, if the system is modified with a pulsed laser pump and ICCD is set for gated mode operation, we assume the system will yield a better image. when it comes to CW pump-driven SPDC-based quantum imaging the EMCCD would be the best choice as they have $> 95\%$ quantum efficiency. Therefore, figure 5.3 (c) gives us only a proof of concept result. However, one can realize by comparing the noisy classical and quantum correlation-based imaging schemes (figure 5.3 (b) and (c)), the latter has the better contrast. For better results and experimental analysis, we need to have an ICCD/EMCCD camera with relatively high quantum efficiency. To analyze the presented experimental method, we perform a simulation of the exact experimental method hoping that will be useful to study the experimental method further and analyze its important features.

5.2 Analytical discussion of quantum imaging experiment

This section discusses the procedure of simulating the experimental setup discussed in the previous section and the analysis of the achieved results. We have used a 4mm-BBO crystal with a Gaussian pump beam of waist size $0.610 \pm 10\ mm$ have a spatial correlation factor $\sigma_0 = 10.8\ um$ to generate the signal and idler photon pairs. In the experimental settings, the SPDC spatial modes fall on the object under study in a 4f lens configuration. The $1/e^2$ width of the Gaussian SPDC field at the object is 0.540 mm, which has a shape shown in figure 5.4. The width value of the SPDC mode highly depends upon the length of the nonlinear crystal and the position of the collimation and focussing lenses used in the setup (lens1 and lens2 in figure 5.1). We have followed the theory explained in section 3.3 to find the beam's radial size. To find the SPDC profile's size at the object we used the standard propagation equation- $\omega_0 = 4\lambda f/2\pi D$, where λ is the wavelength of the illuminating light, f is the focal length of the objective lens and D is the beam diameter.

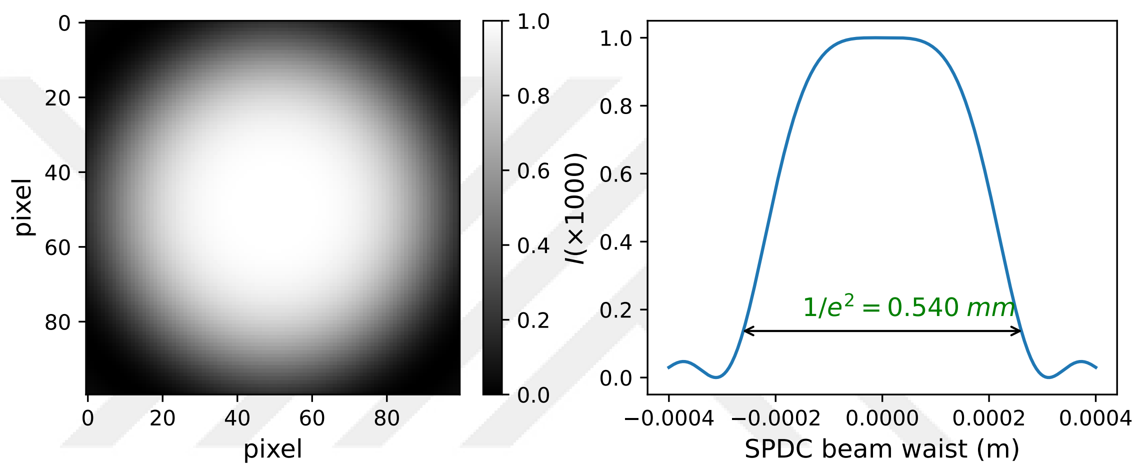

Figure 5.4: (a) SPDC profile at the object location the width and height are equal and (b) the Gaussian profile of the SPDC with $1/e^2$ value of 0.540 mm.

5.2.1 Simulating an object

The creation of an object, for the simulation purpose, is conveniently formed by the matrix method. In the experimental section, we have seen that camera pixels are processed in a matrix format. Therefore, representing an object in matrix form is more convenient. The principle of image formation is depending upon illuminating light's transmission and absorption/reflection characteristics with the object. Therefore, a 2D object placed in the path of light rays can be mathematically represented in transmission and reflection coefficients as

$$t^2(x, y) + r^2(x, y) = 1 \tag{5.3}$$

where t is the transmission coefficient, r is the absorption/reflection coefficient and x and y are transverse position values in a Cartesian plane. Let us take $t^2 = T$ and $r^2 = R$ and T and R are in matrix form. The transmission and reflection/absorption matrix have binary values such as 0 or 1 depending on the transmissive or absorptive/reflective object. Since the SPDC field has a specific intensity profile, the SPDC field falls on the object, depending upon the characteristics of the object, the outgoing (from the object) SPDC beam will take a shape by following the mathematical process which is given by,

$$T_{m\times n} \odot \mathcal{I}_{m\times n} + R_{m\times n} \odot \mathcal{I}_{m\times n} = 1 \odot \mathcal{I}_{m\times n} \tag{5.4}$$

where $\mathcal{I}$ is the intensity profile (in matrix form) of the SPDC field and $\odot$ indicates the Hadamard operation. $m \times n$ in equation 5.5 indicates all the matrix has the same dimensions. We will drop indicating this henceforth for simplicity. To measure the resolution of an imaging system, we will choose an object that has standard parameters. We can obtain any object by playing with equation 5.5. At this time we have chosen evenly spaced 3-slits having width and spacing equal to 25 um as an object. Using an evenly separated 3-slit as an object has several advantages. Firstly, With line sets of three, these targets offer the advantage of an increased ability to recognize spurious resolution. Spurious resolution occurs when a set of lines is sufficiently blurred such that the overlap appears to form inverted, more distinct lines. This can cause a misreading of the resolution of the optical system- since it will appear that the lines are distinguishable. The spurious resolution also results in the appearance of one less line than exists in the line set. Since the difference between three lines and two is more easily noticed than the difference between five lines and four, for example, it is easier to recognize the occurrence of spurious resolution in targets with sets of only three lines. Secondly, the standard method uses line pairs per mm (lp/mm) as a resolution testing unit with one bright line and one dark line considered as one line pair (we will use this technique in the later section to understand the performance of the imaging systems). By choosing an even number of slits, we will have a case when more pairs an imaging system can recognize have high resolution: a higher value in lp/mm means the distance between each pair of lines is smaller. In this kind of object, the bright lines are transmissive to the entering light and the dark lines are absorptive/reflective. So to form an object, we can rewrite the equation 5.5 as follows

$$\begin{aligned}\mathcal{O} &= T \odot \mathcal{I} \\ &= 1 \odot \mathcal{I} - R \odot \mathcal{I} \quad \textbf{positive target} \end{aligned} \tag{5.5}$$

$$\begin{aligned}\mathcal{O} &= R \odot \mathcal{I} \\ &= 1 \odot \mathcal{I} - T \odot \mathcal{I} \quad \textbf{negative target} \end{aligned} \tag{5.6}$$

We will simulate a negative target as a negative target provide more visual contrast. In a negative target, the transmissive part will be binary 1 and the reflective/absorptive one will have the binary value zero. In equation 5.6 for the object we perform $R \odot \mathcal{I}$ then form a negative object, with the SPDC illuminated on top of it, as shown in figure 5.5. Since the $1/e^2$ width of the SPDC beam is 0.540 mm the slit width can accordingly be created. The formed target slit's width of the dark and bright line is 25 um.

In our experiment, the classical field takes a direct single path that goes through the object (in the experimental setup it is the idler path). In the quantum correlation-based experimental settings, the idler goes through the object and its reference pair (signal photons) takes a different path. Here, the signal photons act as a reference to idler photons in such a way that once we know the transverse position of the idler we can predict the location of the signal photons and vice versa. We have seen that the quantum settings immunity to the noise is due to the reference photon's assistance to remove the noise from the system. To understand this in case of experimental settings, the upcoming sections theoretically analyze signal-idler pairs' spatial and

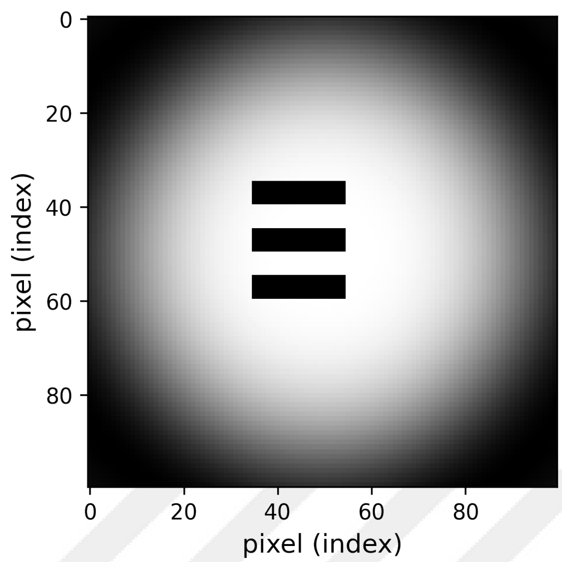

Figure 5.5: Negative evenly spaced 3-slit target. The width of the dark line and the bright line is 25 um.

temporal correlation.

5.2.2 Spatio-temporal correlation

Phasematching is an essential condition for the SPDC process to happen. As the phasematching is rooted in momentum conservation, we can expect SPDC's signal and idler photons to have a spatial correlation. This means that, similar to classical momentum correlation, a knowledge of one particle's position can reveal its momentum-correlated pair's position. Contrarily, the momentum distribution is random in the case of SPDC process and there is a time correlation associated with it. We have seen longitudinal phase matching and its mathematical treatment in chapter III. Referring SPDC photons vector propagation fields shown in figure 5.6, we can write each vector in split form as $k_s = \sqrt{k_{sz}^2 + q_{sx}^2 + q_{sy}^2}$. The letter 'q' refers to the transverse vectors. For transverse momentum conservation, the condition $q_{sy} = -q_{iy}$ (this goes the same for 'x' coordinates, not shown in the figure for brevity). With this, transverse phase-matching of an SPDC source can be generally formulated as

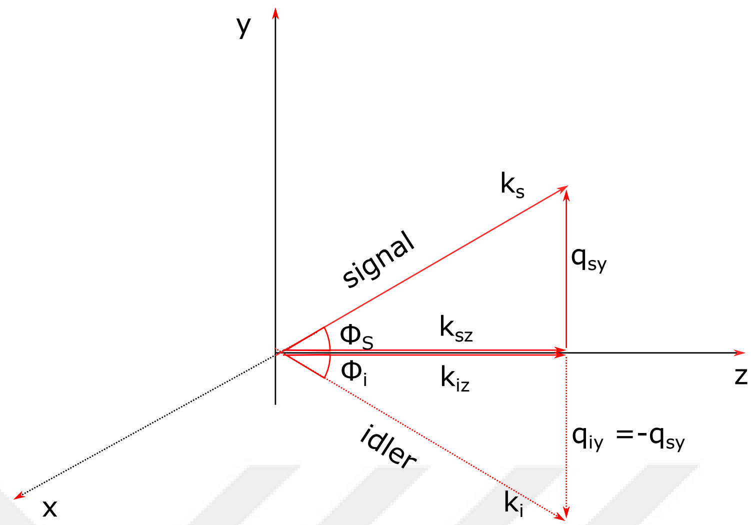

Figure 5.6: Longitudinal and transverse propagation vectors of signal and idler photons.

(refer to chapter III for more details about phasematching)

$$\Delta_q(\lambda_s, \lambda_i; \phi_s, \phi_i) = k_s sin(\phi_s) + k_i sin(\phi_i) \tag{5.7}$$

$$\Delta_q(\lambda_s, \lambda_i; q_s, q_i) = q_s(\lambda_s) + q_i(\lambda_i) \tag{5.8}$$

where $\phi_{s(i)}$ is the emission angle and the propagation vector $k = \frac{2\pi n(\lambda)}{\lambda}$. Details of each parameter and calculation of polarization and wavelength-dependent index of refraction for each signal are given in chapter-III. Reminded that we operate in the collinear geometry and our $\theta_c = 28.80°$ and pump, signal, and idler wavelengths are 405 nm, 780 nm, and 842 nm, respectively. As we have seen in previous sections, SPDC phasematching function (explained in section 3.3.1) allows us to have various wavelengths around central wavelengths. This also means that we can expect various emission angles even in a collinear geometry, hence, we will see a distribution of q-vectors in the spatial field. To simulate this, we fixed the pump to the above-mentioned value and varied the signal and idler wavelengths. Here, equation. 5.8 can be rewritten in a suitable form as

$$\Delta_q(\Omega;\phi_s,\phi_i) = \frac{2\pi n_s^o(\lambda_{s0}+\Omega)}{\lambda_{s0}+\Omega} sin(\phi_s) + \frac{2\pi n_i^o(\lambda_{i0}+\Omega)}{\lambda_{i0}+\Omega} sin(\phi_i) \tag{5.9}$$

$$\Delta_q(\Omega;q_s,q_i) = q_s(\Omega) + q_i(\Omega) \tag{5.10}$$

Where Ω is the detuning wavelength, λ_{s0} and λ_{i0} are the central wavelength of the signal and idler photons, respectively. The transverse emission profile (emission angle versus wavelengths) of the signal and idler can be understood from a phasematching function which can be expressed as

$$S(\Omega;q_s,q_i) = sinc(\Delta_q(\Omega;q_s,q_i)L/2)^2 \tag{5.11}$$

where L is the length of nonlinear crystal and $sinc(x) = sin(x)/x$. The length of the crystal used for this study is 4 mm. By varying detuning wavelength(with fixed $\lambda_{s0} = 780nm$ and $\lambda_{i0} = 842nm$), Ω in equation 5.11, we can understand the signal-idler spectral correlation. The SPDC spectral correlation is shown in 5.7. The figure

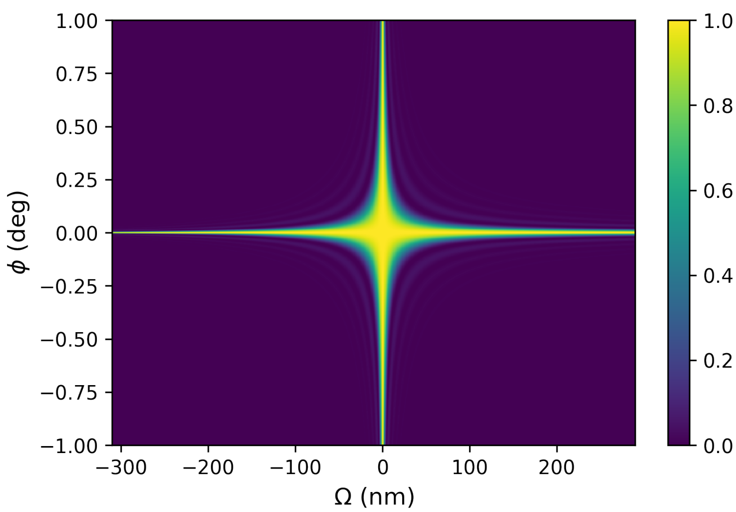

Figure 5.7: Spectral correlation of signal and idler photons in the transverse plane.

shows that the condition of being the signal photon is at 780 nm and the idler at 842.4 nm has a high probability (frequency correlation) as maximum emission intensity is shown when $\Omega = 0$. The frequency entanglement follows in any wavelength value only condition is momentum and energy conservation should be respected. This is a strong spectral correlation with angular distribution as a deciding parameter. At the same time, the figure also concludes that each wavelength value has an associated emission angle and there exists a small amount of uncertainty in the SPDC emission wavelength. In simple language, the wavelength and emission angle have features that depend on each other. We will later see this basic property of the SPDC will lead to spatio-temporal correlation. Since the emission angle corresponds to transverse momentum correlation, we can convert the emission angle to a transverse momentum component i.e. $q_{s(i)} = k_{s(i)} sin(\phi_{s(i)})$. Also, since transverse momentum should be conserved, we can write $|q_s| = |-q_i| = q$. We are more interested in position-time correlation of the SPDC. Therefore, we need to convert the momentum and spectrum parameters to position and time domains. As momentum-position and frequency-time are canonically conjugated parameters, applying a Fourier transform to the equation 5.11 can turn momentum-frequency to spatio-temporal correlation ie.,

$$G^{(1)}(x,\tau) = \int\int dq d\Omega S(q,\Omega) e^{i(q.x + \frac{2\pi c}{\Omega}.\tau)} \tag{5.12}$$

Equation.5.12 gives the first-order Spatio-temporal correlation. Therefore, second-order correlation function $G^{(2)}$ of position time can be given by

$$G^{(2)}(x,\tau) = \left| \int\int dq d\Omega F(q,\Omega) e^{i(q.x + \frac{2\pi c}{\Omega}.\tau)} \right|^2 \tag{5.13}$$

where

$$F(q,\Omega) = sinc(\Delta_q(\phi,\Omega)L/2) \times Exp(i\Delta_q(\phi,\Omega)L/2) \tag{5.14}$$

Simulation of the equation 5.13 will give a spatio-temporal correlation of the signal and idler photons. Figure 5.8 shows spatial and temporal correlation with a specific correlation width. In practical scenarios, this means that we can expect a transverse spatial correlation only within a time scale. Reversely, if we want to see a spatial correlation we need to make a measurement for the momentum correlation within the timescale defined by figure 5.8. The spatial and temporal correlation individually can be observed in figure 5.9. From the figure, we can see that the temporal correlation width is 3.2 ps, and for the spatial one, it is 80 nm. Later in this chapter, we will see how the spatial and temporal correlations between signal and idler photons can be utilized to demonstrate an imaging scheme. In our experimental scheme, this means that when an idler photon is observed at a position say "x_i" the signal photon associated with it will be observed at "$x_s = -x_i$" within a time scale of 3.2 ps and with an uncertainty of 80 nm.

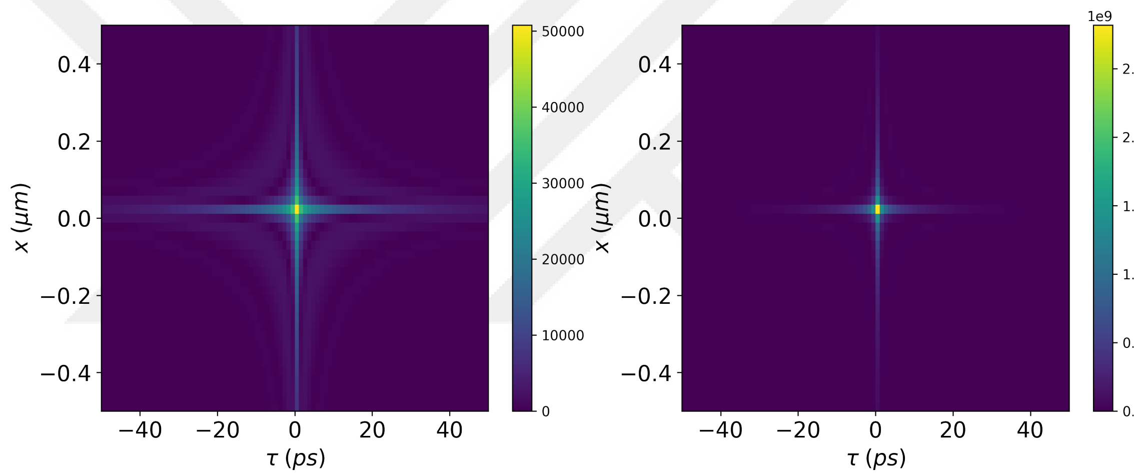

Figure 5.8: Nonnormalized spatio-temporal first-order correlation (left) and nonnormalized spatio-temporal second-order correlation (right).

5.2.3 Input parameters on spatio-temporal correlation

5.2.3.1 Effect of the Pump beam waist on spatial correlation

Although we theoretically find an exceptional spatio-temporal correlation in the SPDC photons, the pump beam characteristics, nonlinear crystal length, and locations of objects and imaging systems can influence the spatial and temporal correlations. These three parameters are collectively referred to as input parameters. In the imaging scheme, we need to characterize the input parameters. Let's consider the SPDC produced by a Gaussian pump. A Gaussian pump laser produced SPDC's

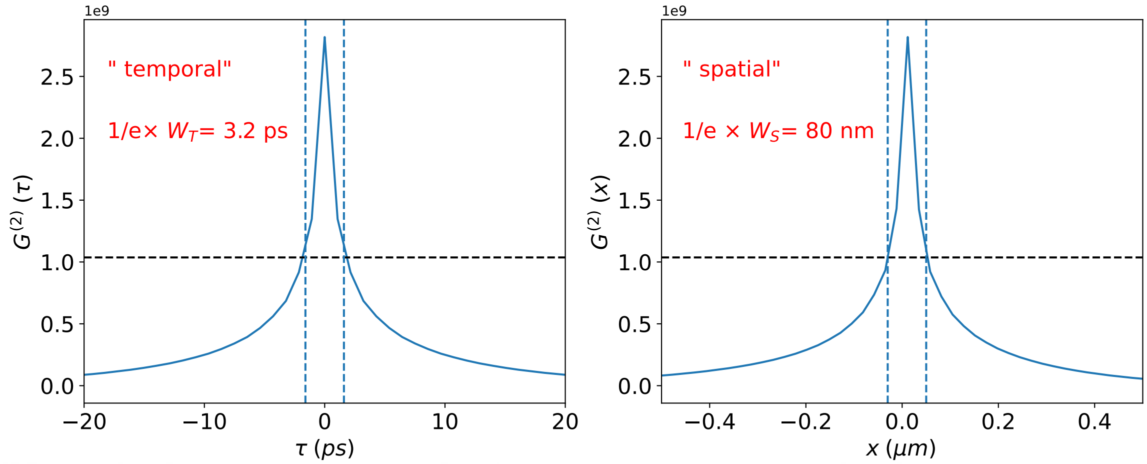

Figure 5.9: The temporal (left) and spatial (right) correlations profile of signal and idler photons. The 1/e width of each are indicated on the plot.

two-photon wavefunction can be defined by [133, 134]

$$\psi(\rho_s, \rho_i; z) = AExp\left(\frac{-|\rho_s + \rho_i|^2}{4w_0^2(1 + (\frac{z}{kw_0^2})^2)}\right) Exp\left(\frac{-|\rho_s - \rho_i|^2}{4\sigma_0^2(1 + (\frac{z}{k\sigma_0^2})^2)}\right) e^{i\phi(\rho_s,\rho_i)} \tag{5.15}$$

where $\rho_{s(i)}$ is the radial transverse position defined by $\rho = \{x, y\}$, w_0 is the longitudinal minimum pump beam waist size, and σ_0 is the transverse beam waist size the value of which can be learned by [98, 132]

$$\sigma_0 = \sqrt{\frac{\alpha L \lambda_p}{2\pi}} \tag{5.16}$$

where α is a constant equals to 0.455 [135] and $k = 2\pi n/\lambda_p$. In our system, the σ_0 is a constant as we fix the nonlinear crystal length and pump wavelength. Therefore, the correlation will be influenced by the pump beam waist size, w_0 and the location of the object and imaging systems. The axial location variable 'z' in equation 5.16 can strongly influence on transverse momentum correlation. For the sake of simplicity at present, we take z = 0 and study the pump beam waist size effect on spatial profile of the SPDC. Towards it, in equation 5.18, we can give $\rho_i = 0$ and study the idler transverse field distribution. That tells us the probability of finding signal photons given the idler observed at $\rho_i = \{x, y\} = 0$. With these conditions inserted, equation 5.18 simplified into

$$P(\rho_s|\rho_i;0) = AExp\left(\frac{-|\rho_s|^2}{4\omega_0^2}\right) Exp\left(\frac{-|\rho_s|^2}{4\sigma_0^2}\right) \tag{5.17}$$

equation 5.17 is called conditional probability. Descriptively, in our example, equation 5.17 tells us the probability of detecting a signal photon given the position of the idler photons is determined. As we expected, figure 5.10 shows the conditional probability of observing signal photons maximum at $\rho_s = 0$. It should be noted that if $\rho_i = 1$, we will expect signal photons around $\rho_s = -1$. We have used two pump beam waist sizes to study their effect on conditional probability. From figure 5.10, when the beam waist size is smaller the conditional probability (position uncertainty) gets smaller. The absolute value of position uncertainty can be extracted from

$$\Delta(\rho_s|\rho_i; z = 0) = \sqrt{\frac{1}{\frac{1}{\omega_0^2} + \frac{1}{\sigma_0^2}}} \tag{5.18}$$

With this description, the transverse position uncertainties are calculated to be $\Delta =$ 4.6 μm and $\Delta = 10.5$ μm when pump beam waist sizes are 1 um and 500 um, respectively. It shows that the small pump beam waist size is desirable as that lower transverse position uncertainty. Although the small beam waist size benefit from higher correlation (so lower transverse position uncertainty) it will be only possible at a cost of the number of spatial modes- which is critical in quantum spatial resolved imaging. If we use a small beam waist with less than transverse uncertainty the number of spatial modes goes less than 1. That is not desirable for achieving many transverse spatial modes that will be needed for demonstrating efficient transverse momentum correlation based quantum imaging scheme. For instance, if the beam waist size is 1 um the number of spatial modes is estimated by using $N = (\omega_0/\sigma_0)^2$ to be 1 μm/10.8 $\mu m \sim 0.0085$ (σ_0 is calculated using 5.16 with L = 4 mm) the same calculation gives N = 2150 when the beam waist is 0.50 mm. With N = 0.0085 as in the case of when $\omega_0 = 1$ μm, the SPDC efficiency becomes poor. By following spatial uncertainty definition, we can approximate the position uncertainty as equals

σ_0 when the beam waist size is high and z = 0. That is the uncertainty definition in equation 5.18 indicate that when the pump beam waist size ranges 0.5 mm to 0.050 mm there is no significant reduction in the uncertainty value. Therefore, we can conclude that a high beam waist size is desirable as the high number of spatial modes can provide better field coherence in quantum imaging. Since the short crystals give more room for having a high value of N defined by equation 5.16. We also conclude that short nonlinear crystals and large beam waist size regime are the best for quantum imaging experiment. Also, analysis of the input parameter effect on spatial profile shows although the fundamental values of spatial correlation of the SPDC are extremely high as seen in section 5.2.2 the input parameters reduce the spatial correlation in a practical setting.

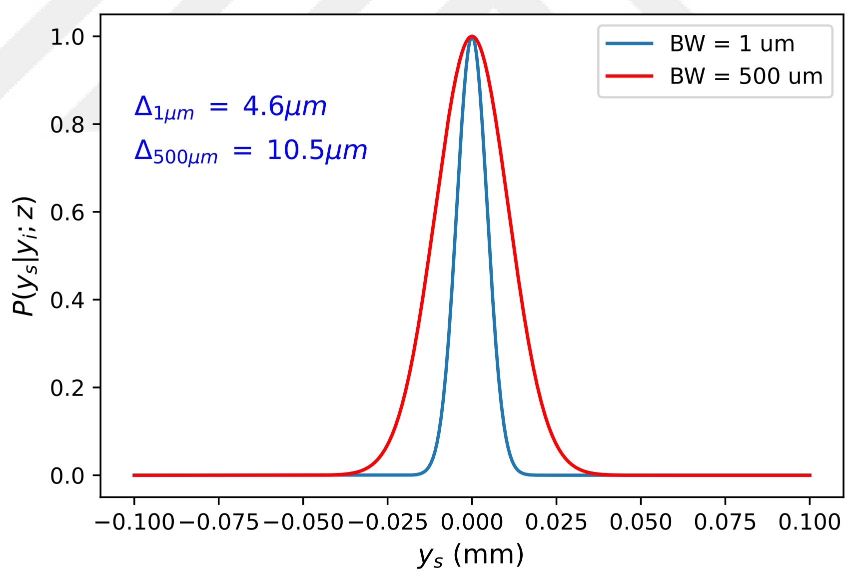

Figure 5.10: Conditional probability of finding the signal photons provided $\rho_i = 0$. Two sets of pump beam values are used in plotting equation 5.17.

5.2.3.2 *Effect of the axial position on spatial correlation*

The optics used in the experiment can also influence the spatial correlation. Specifically, the lens used in the imaging system controls the conditional probability uncertainty in the longitudinal and transverse field distribution. When we use an imaging

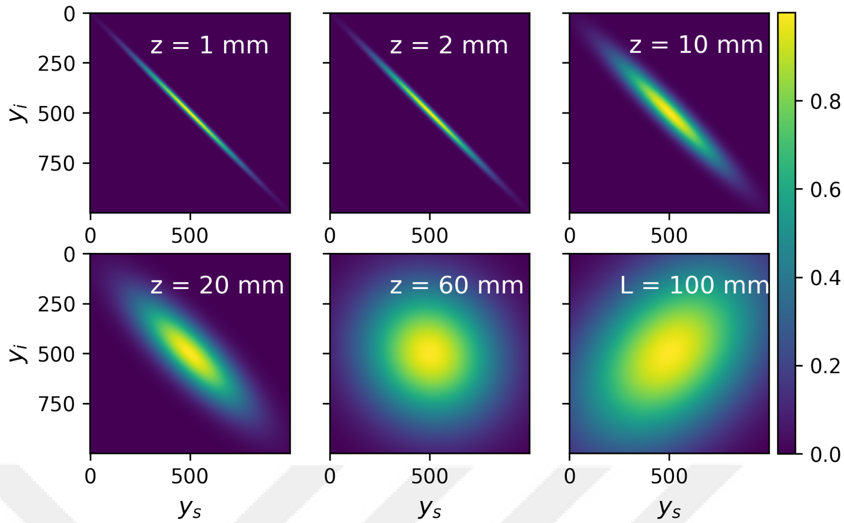

Figure 5.11: Position correlation of the signal and idler at the y coordinate. The left to right takes different z values in increasing order as indicated in each figure. The dotted circle indicates the region where SPDC photons will fall on. The horizontal and vertical intersecting point is the center of the circle.

system in near-field optical configuration, the lens project the transverse modes of the SPDC to the image plane. Therefore, the transverse correlation at the image plane will be identical to that of the z = 0 (SPDC mode generating site at the crystal)plane provided there is no magnification. Meaning, in a standard 4f lens imaging configuration, at the image plane, we can assume that z = 0 and analyze the transverse correlation using equation 5.18 as it is a general equation that takes beam waist size crystal length and axial position, z, as input and give rise to the correlation. As $\rho = \{x, y\}$ in the equation, to simplify further we can take only the y-axis component. By giving various z values in the equation 5.18 with fixed $\omega_0 = 500\ \mu m$ and $\sigma_0 = 10.8\ \mu m$ I have simulated correlation depends on the axial position of the imaging plane. the results show that at the focal position of the 4f lens system (i.e. z = 0), the correlation is maximum and as the imaging plane goes away from the focal plane the correlation is reduced as shown in figure 5.11. This concludes the importance of strict positioning of the object and detection systems. The figure 5.12 shows the decrease of transverse correlation as the axial position goes away from z = 0. Due to this uncertainty of the transverse momentum vectors, there exists a field distribution similar to the point spread function observed in any imaging schemes. This image correlation uncertainty will be seen at the plane perpendicular to the z-axis in a single event will be observed as shown in figure 5.13. As shown in the figure, the signal and idler will be in a symmetrically opposite position i.e. if ρ_s then the idler will be at $-\rho_s$. By incorporating equations 5.18 and 5.11, The event of symmetrically opposite positions can mathematically be written as

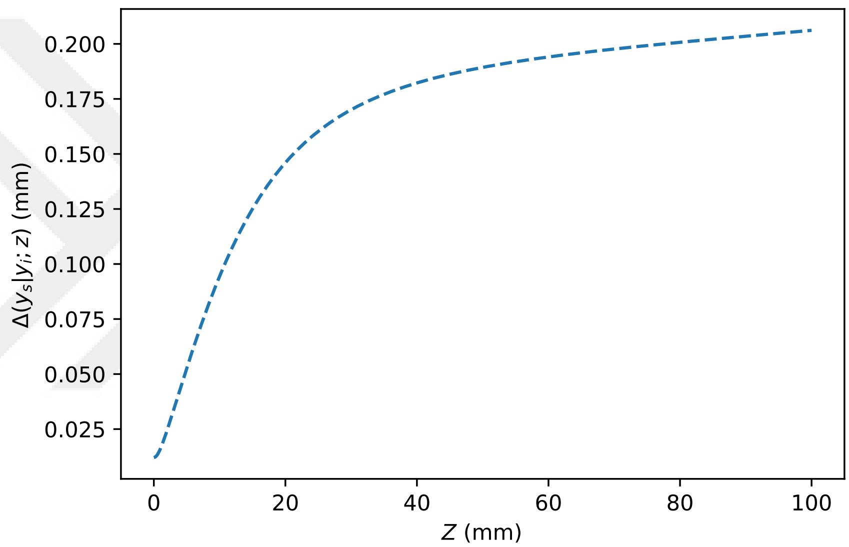

Figure 5.12: The position uncertainty as z goes from 0 $\rightarrow\infty$.

$$\psi(\rho_s, \rho_i, \lambda_s, \lambda_i; z) \propto AExp\left(\frac{-|\rho_s + \rho_i|^2}{4\omega_0^2(1 + (\frac{z}{k\omega_0^2})^2)}\right) Exp\left(\frac{-|\rho_s - \rho_i|^2}{4\sigma_0^2(1 + (\frac{z}{k\sigma_0^2})^2)}\right)$$
$$\times\, sinc\left(\frac{\Delta k(\rho_s, \rho_i, \lambda_s, \lambda_i)L}{2}\right)^2 \tag{5.19}$$

$$\psi(\rho_s, \rho_i, \lambda_s, \lambda_i; z) \propto \int\int\int\int d\rho_s d\rho_i d\lambda_s d\lambda_i Exp\left(\frac{-|\rho_s + \rho_i|^2}{4\omega_0^2(1 + (\frac{z}{k\omega_0^2})^2)}\right)$$
$$\times\, Exp\left(\frac{-|\rho_s - \rho_i|^2}{4\sigma_0^2(1 + (\frac{z}{k\sigma_0^2})^2)}\right)$$
$$\times\, sinc\left(\frac{\Delta k(\rho_s, \rho_i, \lambda_s, \lambda_i)L}{2}\right)^2 \tag{5.20}$$

Equation 5.19 is the emission profile in a single generation of the SPDC signal and idler photons. Here, I write $\Delta k(q_s, q_i, \lambda_s, \lambda_i) \rightarrow \Delta k(\rho_s, \rho_i, \lambda_s, \lambda_i)$ as one can relate

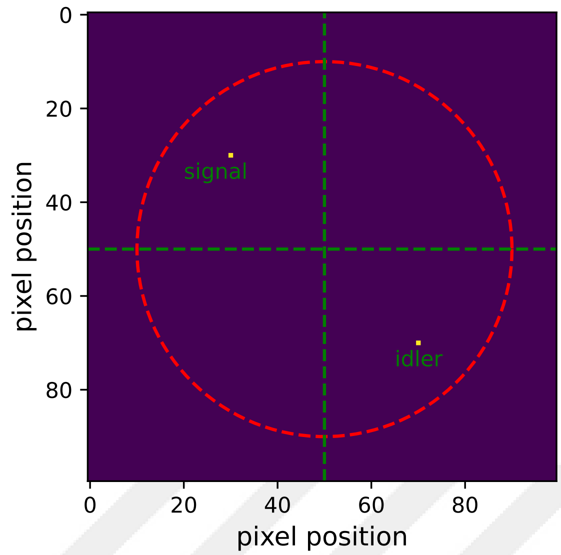

Figure 5.13: The signal and idler field at the momentum anticorrelation (which means when the signal is at (x_s, y_s) idler is at $(-x_i, -y_i)$ in a complex plane) positions seen at the image plane (z = 0) when crystal length is 4 mm and corresponding $\sigma_0 = 10.8\ \mu m$ at a single event.

$q \propto \rho$. When this event happens multiple times, the SPDC process, described by equation 5.20, probabilistically emits signal and idler photons in all directions. In a coincidence event analysis like explained in chapter IV, when we do symmetric spatial positions coincidence measurement in all the events we can observe a 2D intensity correlation measurement plot like experimentally demonstrated in reference [98] as shown in figure 5.14. This 2D plot coincidence plot of signal and idler photons describes SPDC's two-photon transverse correlation observed on the camera.

Figure 5.13 illustrates that the signal and idler photons are spatially correlated, with the signal photons falling on the camera sensor at positions symmetrically opposite to the idler photons. This means when we set the experiment such that idler photons illuminate the object and the signal photons act as a reference to it, we cannot see two photons fall on the camera frame on occasions when the object blocks the idler photons. It's important to note that the temporal correlation between the signal and idler photons, which was theoretically found to be 3.2 ps, is much lower

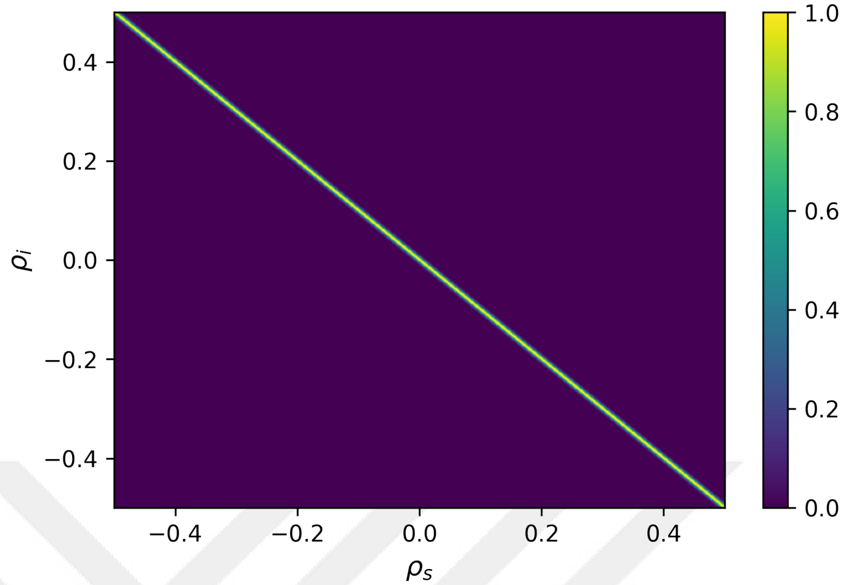

Figure 5.14: 2D coincidence plot where the heat map shows high density for maximum signal idler coincidence. This depicts the fact that observing the idler photons at the anti-momentum correlation location of the signal photons. This plot is referred to as the intensity correlation matrix.

than the camera frame separation time and timing jitters. Therefore, if the object is not present in the path of the idler rays in the experimental setup, ideally we should see two photons appear in all recorded frames. However, when an object is placed at the idler arm (as is the case in our experiment), if the object's transverse feature blocks the idler, we will only see the signal at the camera sensor. Thus, we should discard any frames where only one photon appears at the camera sensor, as this indicates that the detected photon is from a noise source. By doing so, we can eliminate noise in the system and reconstruct an accurate image of the sample under study.

5.2.4 Image system's resolution

The primary factor that affects the resolving power in an imaging system is the optical diffraction phenomenon. To demonstrate the resolving power of a diffraction-limited imaging system, we can examine the two-pin hole diffraction phenomenon as a simple example. When light passes through two small pinholes that are closely spaced and similar in size to the wavelength of the light, the rays at the edge of the pinhole bent and form a circular interference pattern (airy disc). When the separation between the two pinholes gets smaller it becomes increasingly difficult to distinguish the two pinholes separately at the image plane due to the overlapping of the interference pattern. In 1879, Raleigh [136] proposed a minimum condition for resolving two objects. Raleigh's condition for resolving two objects is mathematically written as

$$r = \frac{1.66\lambda}{2NA} \tag{5.21}$$

where NA is the numerical aperture of the lens system defined by $NA = n \times sin(tan^{-1}(D/2f)) \sim D/2f$ where n is the refractive index of the objective lens system, D is the diameter of the light source and f is the focal length of the objective lens. Clearly, apart from the wavelength of the source, λ, which is mostly a fixed parameter, the lens parameters influence the resolving power of the system. Therefore, to achieve high resolution the microscopes utilized objective lenses having high NA. The highest value of NA of the objective lenses available in the market is ~ 1.3. With simple lenses, we can only achieve small NA values- the NA of our system is ~ 0.06. To have a high NA value, the objective lens is usually immersed in oil of having a high refractive index. Since we have used idler photons having wavelength 842 nm, using equation 5.21, we calculated the resolving power of our imaging system to be 11.6 um. To analyze and form an image that is produced by a diffraction-limited imaging system, we can consider the calculated resolution value to be the radius of the airy disc pattern formed due to the diffraction effect [136]. The full airy disc pattern can be simulated by following the definition of the point spread function (PSF)

$$PSF = \frac{1}{2\pi r^2} exp\left(-\frac{x^2+y^2}{2r^2}\right) \tag{5.22}$$

The radius of the PSF function defines the quality of the imaging system. The radius of the PSF pattern monotonically increases with the r-value (equation 5.21). Therefore, the larger the PSF radius (Airy disc's radius) the poorer the quality of the image can get. Mathematically, the actual image is formed by convolving the PSF function with the object. This is done by doing a convolution operation of the object ($\mathcal{O}$) structure and the PSF ie.,

$$Image = \mathcal{O} * PSF \tag{5.23}$$

After performing the convolution operation with the object and the PSF, we can see an image as shown in figure 5.15. Simply, figure 5.15 shows the diffraction-limited image of the 3-slit object with resolution value $r = 11.6$. We can resolve the 3-slit object with the imaging system of resolving power 11.6 um. It is logical to think that the slit separated by 25 um can be resolved by an imaging system with a resolving power of 11.6 um. However, we can see that the contrast of the image is reduced

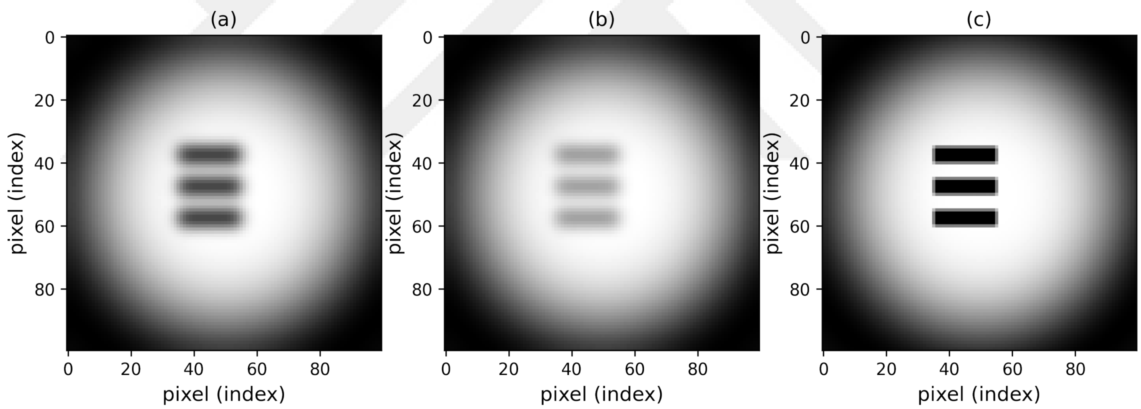

Figure 5.15: The direct detection classical image appeared on the imaging system when the resolution is 11.6 um and noise is null(b) the image of classical noise system seen on the camera. analytically we can think SNR = 1. (c) The direct detection classical image appeared on the imaging system when the resolution is 0.5 um and noise is null.

after convolution with diffraction-imposed PSF. The relation between contrast and the resolution of the imaging system is studied in the final section of this thesis. The appeared image shown in figure 5.15 is an expected image in a simple (diffraction limited) microscope system. In our experiment, we used idler rays to illuminate the object and obtained a direct image of it. To compare the classical and quantum systems in a noisy environment, we channeled the signal photons such that they overlap with the idler beam at the ICCD camera. Thus, the noisy image will appear as shown in figure 5.15 (b). Figure 5.15 (b) is obtained by adding the clean SPDC spatial shape with a diffraction-limited directly observed image (see figure 5.15 (a)). Since the signal and idler always generate together we can conclude the empirical SNR value in the classical noisy imaging settings will be equal to one. The forming image in the quantum method is quite different. In the quantum imaging experimental scheme, we compare the transverse spatial distribution of the signal and idler photons at the image plane. In the comparison procedure, we look at each frame and see if signal and idler photons are present in the individual frame. If we do not see signal and idler photons in a single frame we discard that frame as explained in the previous section. Therefore, the noise will be discarded efficiently and, therefore, we observe an image free from noise as seen in figure 5.15 (a). Notice that in practical cases, we cannot see two photons in a single frame easily as the noise is uncontrollable. Therefore, we have performed an averaging algorithm by taking several frames (in our experimental case we have taken sim 1 million frames).

Although the quantum imaging scheme introduced here has high immunity to noise, the absolute resolution value will be compromised if we do not take care of the input parameters. That is because transverse correlation uncertainty (caused by input parameters) can negatively affect the resolution of the quantum imaging scheme. For instance, we have used optics systems that give NA = 0.06 and calculated the resolution of our system to be 11.6 um. This resolution value is greater than the transverse correlation uncertainty of the system we discussed until now. In a typical microscopy arrangement, the NA value can be as high as 1.3 with an oil-immersed objective lens arrangement. In that case, a classical microscopy arrangement can achieve a resolution value as low as 0.5 um (with illuminating light source wavelength is 840 nm). At the same time, the SPDC's transverse correlation uncertainty is σ_0 10.8 um (when 4mm-BBO and pump wavelength $\lambda = 405$ nm are used). Which is a regime where $\sigma_0 > r$. Reducing the transverse correlation uncertainty (σ_0) is a difficult task as we have seen in the section 5.2.3. In a regime where $\sigma_0 > r$, the classical system can resolve two objects that are spaced as small as 0.5 um. In the case of quantum imaging based on spatial correlation, the correlation uncertainty is $\sigma_0 = 10.6um$. This means when we try to extract the image via correlation measurement, the spread of the edges of the object is about 10.6 um. Since the classical scheme does not rely on correlation for image reconstruction, this does not affect that system. But for the quantum case, the PSF takes a new definition of PSF as the spread now is dictated by the spatial correlation uncertainty (σ_0) i.e.,

$$PSF_{\sigma_0>r} = \frac{1}{2\pi\sigma_0^2} exp\left(-\frac{x^2+y^2}{2\sigma_0^2}\right) \tag{5.24}$$

$$Image = \mathcal{O} * PSF_{\sigma_0>r}. \tag{5.25}$$

When this fact is incorporated into the image formation process as done by the equation 5.23, we can see the classical image formation process always follows the equation 5.23 and 5.22. However, in a case where $\sigma_0 > r$, the quantum imaging system follows equations and . This means, regardless of the optical resolving power of the system, if the transverse correlation uncertainty is greater than the absolute resolution value ($\sigma_0 > r$), a quantum system cannot achieve a resolution as good as the classical one in the same experimental settings. That summarises, in a quantum imaging system of our kind the resolving power will highly depend on transverse momentum correlation, i.e., in the regime $r < \sigma_0$ the imaging system's resolution would be σ_0 and if $r > \sigma_0$ the resolution would be "r".

5.2.5 Camera resolution and image quality

The spatial resolution of the digital camera (ICCD camera in our case) can also play an important role in forming a quality digital image. A standard requirement of the camera system for transferring the resolution of the imaging systems is the Nyquist condition [137]. Nyquist theorem requires us to have the camera resolution

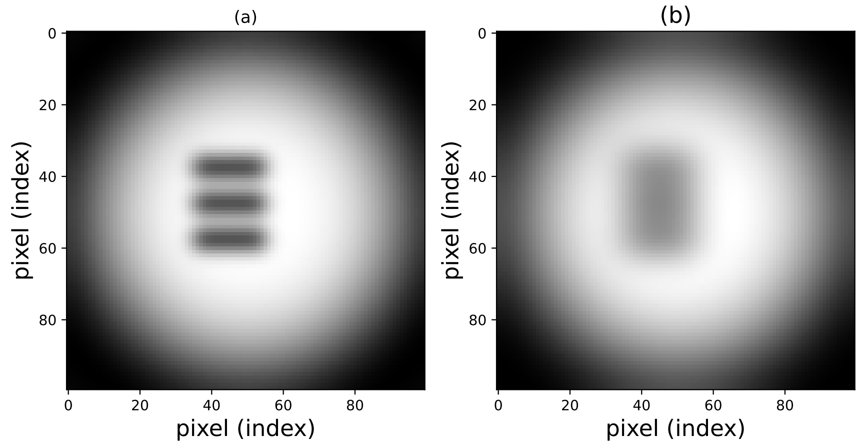

Figure 5.16: Images from the microscopy system where the camera resolutions are (a) 13 um and (b) 26 um. Again, the width of bright and dark lines is 25 um each. Therefore, the camera with 26 um spatial resolution cannot resolve the 25 um samples according to the Nysguist theorem (see text).

double the optical resolution, i.e R = r/2, where R is the camera's spatial resolution. At first glance, this requirement seems impossible to achieve in an imaging system that provides high optical resolution. By the definition of the Nyquist condition, if the resolution of the microscopy system is 1 um the camera system should have a spatial resolution of 0.5 um. There is no EMCCD or ICCD camera available in the market that provided 0.5 um spatial resolution. To solve this problem, we can rely on magnification lenses and which in effect expand the few micro meter scale object features into a large size defined by the magnification factor (M). That effectively turns Nyquist's condition to

$$R = M\frac{r}{2} \tag{5.26}$$

where M is the magnification of the imaging lenses. For instance, if the camera spatial resolution is 13 um (that is a typical CCD-based camera resolution) then one needs to magnify the image by 26 times to resolve a 1 um point object separation. Figure 5.16 shows two images of our 25 um separated object of 3-slits when imaged with a 13 um resolution camera (figure 5.16 (a)) and 26 um resolution (figure 5.16 (b) - remember the ICCD camera used in this study has a spatial resolution of 26 um) cameras. Clearly, the second system has not followed the Nysguist requirement, therefore, even though the optical resolution of both systems is the same since the $R \sim 25um$ we cannot resolve the slits as expected.

5.2.6 Modulation Transfer Function analysis

To evaluate the imaging system's performance, a common approach is to conduct a Modulation Transfer Function (MTF) analysis, which assesses the system's ability to transfer contrast from the object plane to the image plane. The MTF is mathematically defined as the ratio of the image's contrast to the object's contrast at a given spatial frequency. In this study, until now we have used a sample object consisting of three slits, each separated by 25 um with a width of 25 um. To obtain a comprehensive understanding of the imaging system's quality and to perform MTF analysis, the width of the slit was varied, and calculated the MTF. As we have used a sinusoidal object to analyze the system's performance, the contrast (or modulation) of the image can be learned by scanning the pixel position in the three-slit object and recording the intensity values in each pixel location. In figure 5.17, the dark region means lower intensity and the bright one is a high-intensity region. As we scan through objects horizontally, we can record the intensity values at each pixel position. We observe a step function (see figure 5.17) when the object is clean from any quality degrading factors such as diffraction, aberration, noise, etc. In order to find the empirical value of contrast, we followed the definition of contrast for a sinusoidal object, i.e.,

$$C = \frac{I_{max} - I_{min}}{I_{max} + I_{min}}, \tag{5.27}$$

where C is the contrast factor, I_{max} is the maximum intensity value of the step or sine function, and I_{min} is the minimum value of it. From the equation 5.17, we find that the contrast of the object is 100%. As MTF's definition suggests, the ratio of image contrast to object contrast will give us the MTF value. Since the object's contrast is always 100%, the observed image's MTF is simply the contrast of the image, which

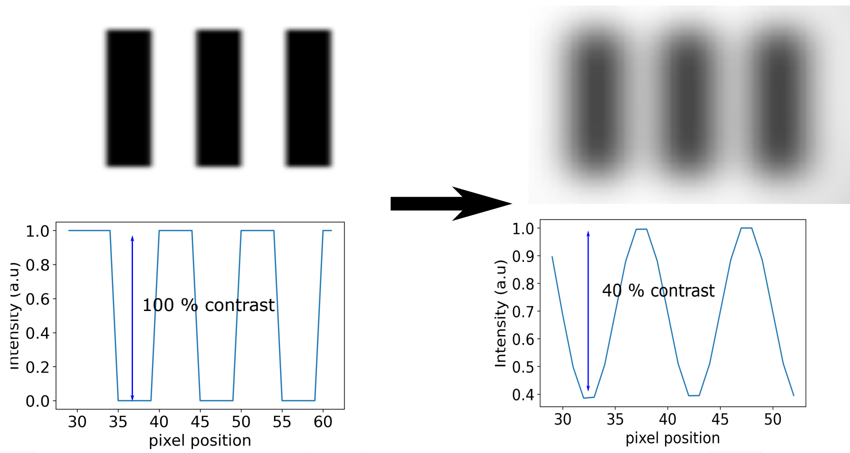

Figure 5.17: The contrast comparison at object and image planes.

can be determined using equation 5.27. In order to comprehend the MTF of the imaging system at different resolution values, it is necessary to convert the resolution values into spatial frequencies (spatial resolution in the frequency domain). To do so, we need to find the number of line pairs that can be present in one millimeter (lp/mm) in an equispaced object like ours. As an example, a continuous series of black and white line pairs with a spatial period measuring 25 um dark and 25 um bright line would repeat 20 times every millimeter and therefore have a corresponding spatial frequency of 20 lp/mm. To show spatial frequency versus contrast factor relation, the spatial frequency is varied by adjusting the slit width. We have measured the contrast of imaging systems at different spatial frequency values in the unit of lp/mm and the result is plotted as shown in figure 5.18. Remember that our Raleigh resolution value is 11.6 um. Figure 5.18 shows the contrast values for various spatial resolutions in a unit of lp/mm in both classical and quantum imaging experimental setups. As we discussed, classical and quantum imaging schemes were performed in the noise background and as the noise is strong in the case of the classical scheme compared to the quantum one the contrast of the classical system (therefore MTF value) is observed to be very poor (see figure 5.18). We find that the MTF values for the quantum case are about 3 times greater than the classical counterparts in

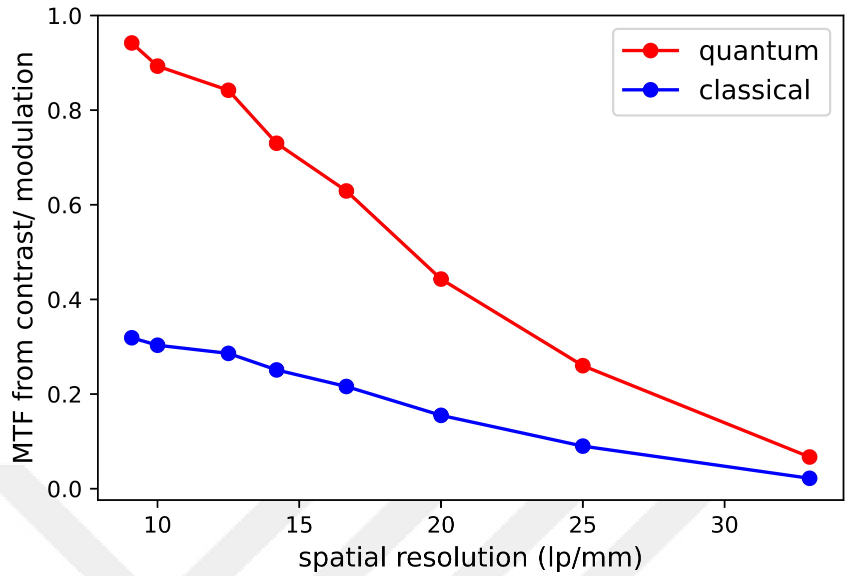

Figure 5.18: MTF of the classical and quantum imaging systems in a noisy environment.

the given noise condition. We can observe that as the spatial frequency increases the contrast of the image gets lower for both classical and quantum cases. The MTF value goes to zero as the spatial resolution approaches the reciprocal of 2 times the absolute resolution (1/2r, r is the absolute resolution- in our system's settings, r = 11.6 um). This is expected because when the slits are separated less than the resolution of the system we cannot resolve the two objects as two entities, hence MTF = 0. The position where contrast reads zero is referred to as the cut-off frequency as we cannot extract information after that point due to the diffraction limit. From figure 5.18, we can see that the MTF of the quantum system is higher than the classical one in all spatial resolution values. Therefore, we can conclude the quality of the image produced by using the quantum scheme presented here is high compared to the classical counterparts when operated in a noisy environment.

CHAPTER VI

CONCLUSIONS AND OUTLOOK

This thesis investigated the capability and implementation procedure of a quantum mechanics-based imaging scheme called quantum imaging. To attain this objective, the thesis is divided into three major topics. Firstly, a theoretical modeling of the technique used for driving the quantum imaging system is presented. Secondly, an investigation for learning the quantum behavior of the presented quantum source and its capability to reduce the noise from the system is analyzed. Finally, the thesis discussed a quantum mechanics-based imaging scheme where the spatio-temporal correlation of the driving source is used to achieve a 2D spatial structure of a sample.

Modeling the quantum source: Because the quantum mechanical features are sensitive, it needs a sophisticated instrument for demonstrating the practical quantum sources. Therefore, the evolution of a quantum source has grown along with technological advancement. One technique that is robust and well-known for demonstrating photonic quantum features is based on a nonlinear process called the spontaneous parametric downconversion process. We showed that the conditions to happen SPDC can only be satisfied by using appropriately designed birefringent crystals. The two major ways of designing birefringence crystals for this application are critically phasematched and noncritically phasematched configurations. This work showed how critically phasematched nonlinear crystals can be designed for SPDC pair production. This is done by selecting BBO crystals that exhibit high birefringence and tuning the optical angle appropriate to our application. As fundamentals of SPDC pairs generation have a quantum mechanical root, the SPDC photon pairs exhibit quantum correlations in multiple degrees of freedom. The comprehensive theoretical analysis of the engineered SPDC source is shown to have violated many classical bounds, assuring that the signal and idler pair generated in the SPDC process is a true quantum source.

Quantum source for noise suppression task: The capabilities of the quantum source are realized after the inception of the SPDC-driven quantum source. The initial time witnessed using temporal correlation of the signal and idler pairs for testing many fundamental principles in quantum mechanics. This includes the quantum-based technique to target detection problems. This technique comes under the category of LIDAR/RADAR technology which aims to learn the details about an object present in a noisy environment. By utilizing quantum temporal correlation with the assistance of advanced detection technologies, an improved LIDAR/RADAR model called quantum illumination can be developed. Chapter IV presented a comparative study of classical direct detection and quantum coincidence detection in a LIDAR/RADAR setting demonstrating that the quantum detection scheme enhances the signal-to-noise ratio (SNR) by a factor of 5.35 (7.28 dB) compared to its classical counterpart. The high SNR of the quantum lidar system has implications for quantum imaging systems. Because the quantum imaging scheme presented here uses temporal and transverse spatial correlations for achieving a 2D imaging scheme and the noise immunity of the quantum imaging system is coming from the temporal correlation of the SPDC source.

Quantum spatial correlation and imaging: The SPDC field's spatial properties are unique to quantum systems. When photon pairs are born in an SPDC process the individual photon share deterministic spatial and temporal information. Meaning if we know the position of an SPDC photon, we can calculate the position of its twin pair within a small time scale (spatio-temporal correlation). However, knowing beforehand where the photon will be detected in the transverse spatial plane is truly indeterministic. This feature of the quantum source gives an opportunity to efficiently obtain the image of an object that is placed under study in imaging systems. As we have a reference of the photon that illuminated the object under study, the quantum source makes it possible to efficiently remove the noise photons from the system. This reference photon-assisted imaging is popular for demonstrating sub-SNL limited imaging systems, quantum ghost imaging, and various others. This special property of the SPDC is used in this thesis to demonstrate a quantum imaging scheme. A proof of concept quantum imaging experimental scheme is successfully demonstrated that can extract the spatial features of the object with high resistance to noise.

Our investigation reveals that the presented quantum imaging experimental scheme is limited by the diffraction phenomenon, and the study highlights the importance of considering input parameters before embarking on a quantum imaging experiment based on spatial correlation of the SPDC process. The detailed theoretical analysis shows that the input pump beam waist size, nonlinear crystal length, and the location of the object and imaging instrument are essential parameters that affect the imaging system's performance. The study demonstrates that a thin nonlinear crystal and large pump beam waist size are desirable for a quantum imaging system. As classical systems do not demonstrate a positional correlation as in the SPDC, this is unique to the quantum system. After emulating a standard object and characterizing the input parameters, the simulation shows an image that is strongly immune to the present noise, making the system more suitable for applications where noise suppression is important. Additionally, we encountered a regime where the quantum system's performance will be poor. We find that when the input parameters induced correlation uncertainty is higher than the resolution value the classical system has an upper hand. This is because the correlation uncertainty influences the point spread function of the imaging system.

CHAPTER VII

ANCILLARY MATERIALS

7.1 Python codes

Some of the important python codes written to realize this work is given below as sections.

7.1.1 Crystal cut angle calculation

Calculation of the crystal cut angle (phasematching angle) corresponding to pump signal and idler wavelengths to be 405 nm, 780 nm, and 842 nm respectively for BBO type-1 crystal configuration. The result will show the cut angle to be 28.80°.

```
#code 1
#import libraries
import numpy as np
import math
import matplotlib.pyplot as plt
# Sellmier equations
def nord(a): # Selmier refreactive index of ordinery beam
    s = 2.7359 + (0.01878 / (a**2 - 0.01822)) -(0.01354 * a**2)
    ↪  #Sellmier equation is for wavelength in micrometer
    ori = np.sqrt(s)
    return ori

# Selmier equations for BBO crystals
def next(a):
```

```
    eri = np.sqrt(2.3753 + 0.01224/(a**2 - 0.01667) - (0.01516 * a**2))
    return eri

def airIndex(a):
    cc = 1.000287566 + 1.3412/((10**18*(a**2))/10**12)
    return cc # Sellmier equation for air

def calcWL(p, s): # Here we calculate the wavelength of idler beam for given signal and pump beam (non-degenarate case)
    i = (s * p) / (s - p)
    return i

#Crystal angle calculation when the pump is 450 nm signal is 780 nm
p = 0.405
s = 0.780
i = (s * p) / (s - p)
nop = nord(p)
nep = next(p)
nos = nord(s)
nes = next(s)
noi = nord(i)
nei = next(i)

a = math.pi # defining pi value
e = 180/3.14 # defining in radian from degree
l = nep**2 * nop**2
m = nos/s + noi/i
n = nep**2 - nop**2
```

```python

d = math.sqrt(((1/(m**2*p**2))-nop**2)/n)
theta = math.acos(d)*180/a
print(theta)
```

7.1.2 SPDC mode and object creation

The python program that creates the SPDC mode and its subsequent fall on the object of 3-slits is shown in the code provided below. The code used brute force to achieve the positive and negative objects. I have used negative objects for analytical study. Following equations 5.5 and 5.6 are used to achieve the positive and negative objects.

```python
#code 1
from numpy import * # importing numpy library
import matplotlib.pyplot as plt # importing matplotlib library
m = 10e+6
mm = 10e-3
nord = lambda Lambd: sqrt(2.7359 + (0.01878 / ((Lambd*m)**2 - 0.01822)) -(0.01354 * (Lambd*m)**2)) # lambd is wavelength in meter, Selmier refreactive index of ordinery beam

next = lambda Lambd: sqrt(2.3753 + 0.01224/((Lambd*m)**2 - 0.01667) - (0.01516 * (Lambd*m)**2))  # Selmier refreactive index of extra-ordinery beam

i = lambda p, s: (s * p) / (s - p) # calculating idler from known pump and signal wavelength

```

```
Phasematching = lambda lambd1, lambd2, lambd3, theta, phi: 2*pi*(ne(lambd1*nm, theta)/(lambd1*nm) - nord(lambd2*nm)/(lambd2*nm) *cos(phi)- nord(lambd3*nm)/(lambd3*nm) *cos(phi)) # gives the SPDC beam profile

L = 4*mm # length of the crystal
k = 0.000  #variying crystal cutangle from phasematching angle, k =0 if collinear geometry
theta1 = ((28.7965+k)*pi/180) # crystal cut angle
phi = linspace(-1, 1, 10000) # plar and azimuthal angle of spdc
funcNoncollinear = lambda lambd, thet, phi,  : sinc(phase_mismatch_gen(405, lambd, i(405, lambd), thet, phi)*L/2)**2
plt.plot(phi*pi/180, funcNoncollinear(780, theta1, phi*pi/180)) #efficiency vs emission angle plot
plt.xlabel('emission angle ($\phi$ (deg))')
plt.ylabel('efficiency')

plt.show()

#code 2
# creates spatial mode of SPDC
d = 50*mm # crystal to camera separation
x = linspace(-0.25, 0.25, 100) #x axis of the plane at d distance far from the crystal plane
y = linspace(-0.25, 0.25, 100) #y axis of the plane at d distance far from the crystal plane
x = [i*mm for i in x] # converting to millimeter to meter
```

```python
y = [i*mm for i in y] # converting to millimeter to meter

x, y = np.meshgrid(x,y)
cartesian = [funcNoncollinear(780, theta1,
↪ arccos(d/sqrt(X**2+Y**2+d**2))) for X,Y in zip(x,y)] #polar to
↪ cartisian conversion
I = np.array(cartesian)

ax = sb.heatmap(cartesian,   vmin=0, vmax=1) #heatmap showing the
↪ spatial structure seen from the z-direction
plt.axis('equal')
ax.set(xlabel='pixel', ylabel='pixel')
plt.show()
#code3
#applying brute force to create 3 slit image
k = 5 # resolution, we have array resolutionm of 5um
for i in arange(35, 35+4*k): #first slit
    for j in arange(35, 35+k):
        I[j][i] = 0*I[j][i]
 # resolution
for i in arange(35, 35+4*k): #second slit
    for j in np.arange(35+2*k, 35+2*k+k):
        I[j][i] = 0*I[j][i]
for i in np.arange(35, 35+4*k): #third slit
    for j in np.arange(35+4*k, 35+4*k+k):
        I[j][i] = 0*I[j][i]
plt.imshow(I) # This will show the object
plt.show()
```

```
#Code4
Negative_object= np.multiply(cartesian,R) # applying Hadamard operation and cartesion--> SPDC spatial mode, R--> reflective matrix
Positive_Object = cartesian - mixR # obtaining positive object
plt.imshow(Positive_Object, cmap = 'gray') # displaying positive object
plt.show()
```

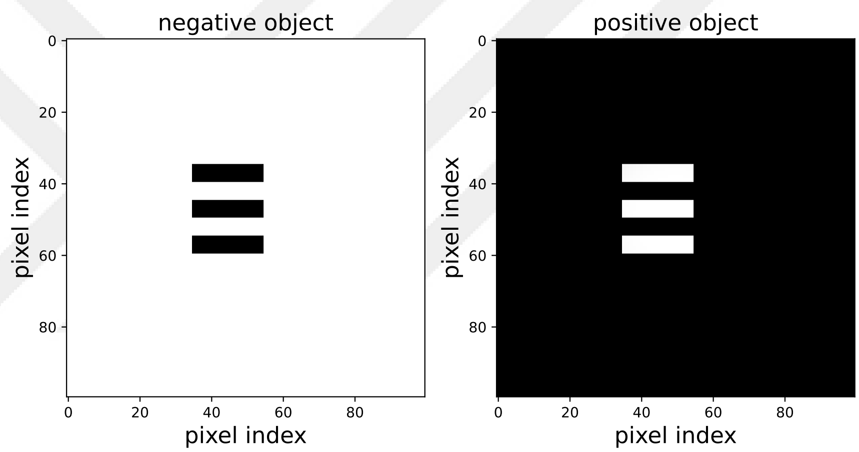

Figure 7.1: Negative and positive evenly spaced objects

7.1.3 Processing ICCD data

Primitives of codes used to post-process the ICCD data are given below.

```
#code1
# importing libraries
import pandas as pd
import numpy as np
import matplotlib.pyplot as plt

```

```python
filename = "E:/QuantumImaging/ICCDData/newData/t8.csv" # the recorded file and saved path
data = pd.read_csv(filename) # file loading

#input for creating 3D array
row = data["Row"]
column = data["Column"]
Frame = data["Frame"]
Intensity = data["Intensity"]
array = np.zeros((max(Frame), max(row)+1, max(column)+1))

R = np.arange(0, max(row)+1)
C = np.arange(0, max(column)+1)
D = np.arange(0, max(Frame))

#array[0][0][0] = data.iat[0,3]
i = 0
for j in D:
    for k in R:
        for l in C:

            array[j][k][l] = Intensity[i]
            i += 1

sum =  np.zeros((100, 59))
for x in range(len(C)):
    for z in range(len(R)):
        for i in range(len(array)-1):
```

```
            current = array[i][z][x]*array[i] - array[i][z][x]*array[i+1]
            sum = sum + current
plt.imshow(sum)
plt.show()
```

7.2 Photographs

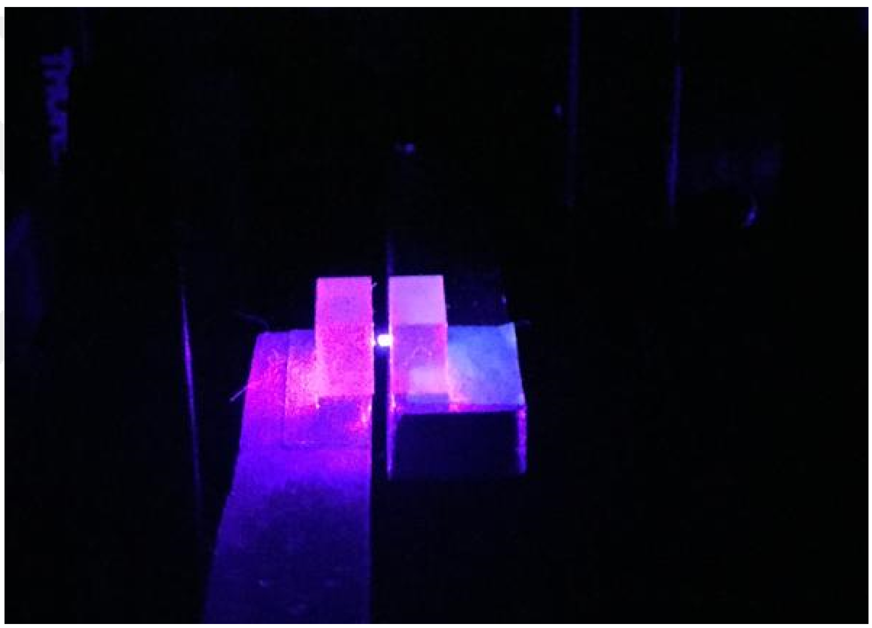

Figure 7.2: A 405 nm pump photon illuminating two BBO crystals.

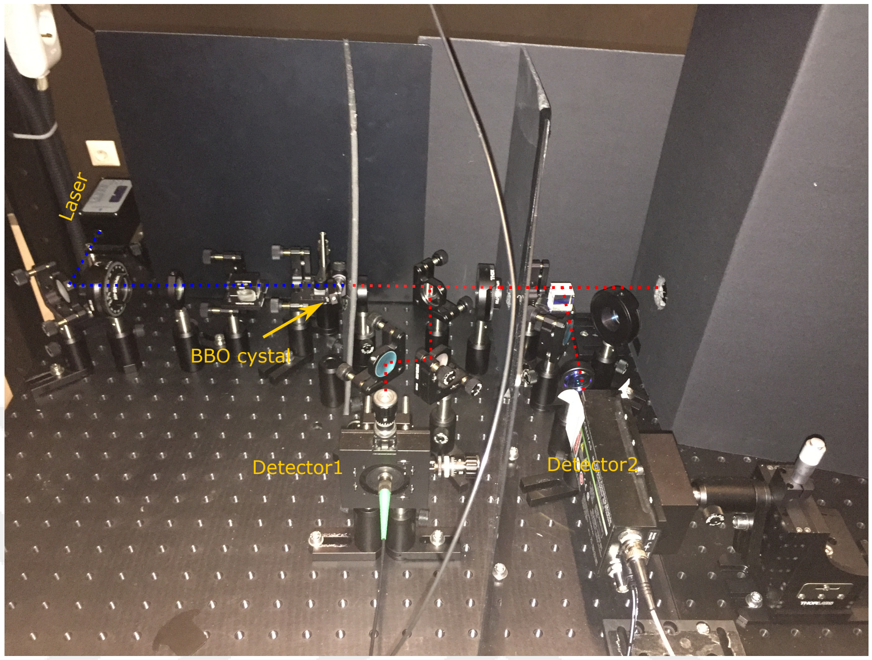

Figure 7.3: Experimental setup for noise to investigate the noise-embedded object detection.

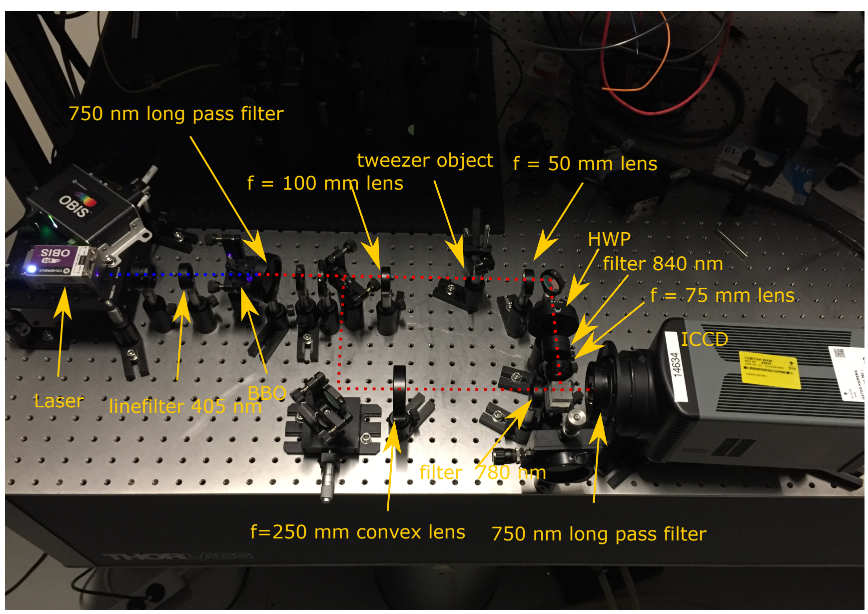

Figure 7.4: Experimental setup for quantum imaging.

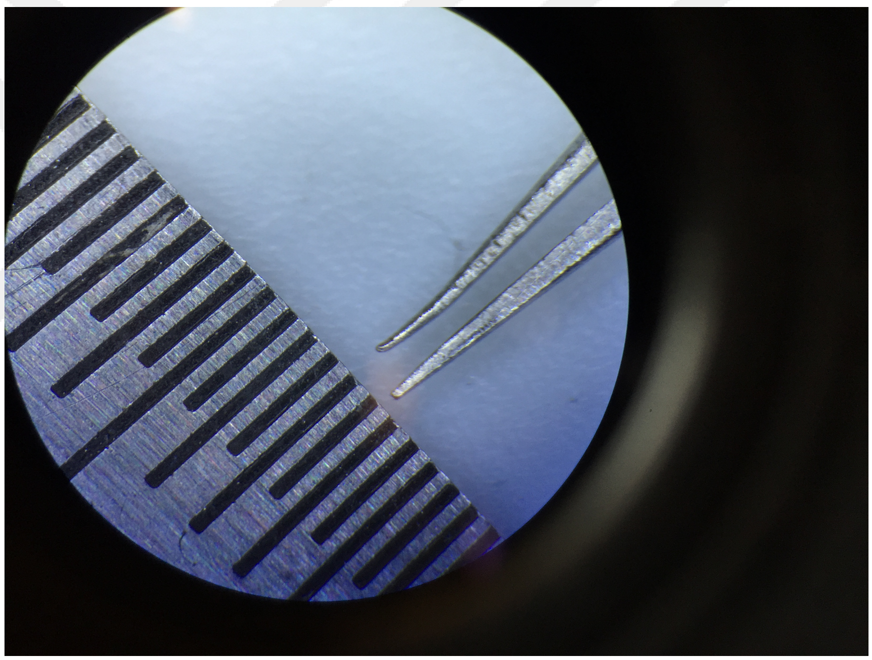

Figure 7.5: Image of a tweezer object seen under the microscope.

REFERENCES

[1] G. I. Taylor, "Interference fringes with feeble light," in *Proceedings of the Cambridge Philosophical Society*, vol. 15, pp. 114–115, 1909.

[2] P. Grangier, G. Roger, and A. Aspect, "Experimental evidence for a photon anticorrelation effect on a beam splitter: a new light on single-photon interferences," *EPL (Europhysics Letters)*, vol. 1, no. 4, p. 173, 1986.

[3] A. Zeilinger, R. Gähler, C. Shull, W. Treimer, and W. Mampe, "Single-and double-slit diffraction of neutrons," *Reviews of Modern Physics*, vol. 60, no. 4, p. 1067, 1988.

[4] C. Boyer, A. Einstein, and L. Infeld, "The evolution of physics: The growth of ideas from early concepts to relativity and quanta," Cambridge: Cambridge University Press, 1961.

[5] E. Schrödinger, "An undulatory theory of the mechanics of atoms and molecules," *Physical Review*, vol. 28, no. 6, p. 1049, 1926.

[6] M. Born, "Quantenmechanik der stoßvorgänge," *Zeitschrift für physik*, vol. 38, no. 11, pp. 803–827, 1926.

[7] A. Einstein, B. Podolsky, and N. Rosen, "Can quantum-mechanical description of physical reality be considered complete?," *Physical Review*, vol. 47, no. 10, p. 777, 1935.

[8] J. S. Bell, "On the einstein podolsky rosen paradox," *Physics Physique Fizika*, vol. 1, no. 3, p. 195, 1964.

[9] J. F. Clauser, M. A. Horne, A. Shimony, and R. A. Holt, "Proposed experiment to test local hidden-variable theories," *Physical Review Letters*, vol. 23, no. 15, p. 880, 1969.

[10] A. Aspect, "Proposed experiment to test the nonseparability of quantum mechanics," *Physical Review D*, vol. 14, no. 8, p. 1944, 1976.

[11] J. Faye, "Copenhagen interpretation of quantum mechanics," 2002.

[12] J. D. Hidary and J. D. Hidary, *Quantum computing: an applied approach*, vol. 1. Springer, 2021.

[13] J. Russel, "Ibm quantum update: Q system one launch, new collaborators, and qc center plans," *HPC Write*, vol. 10, 2019.

[14] C. H. Bennett and G. Brassard, "Proceedings of the ieee international conference on computers, systems and signal processing," 1984.

[15] W.-Y. Hwang, "Quantum key distribution with high loss: toward global secure communication," *Physical Review Letters*, vol. 91, no. 5, p. 057901, 2003.

[16] H.-K. Lo, X. Ma, and K. Chen, "Decoy state quantum key distribution," *Physical Review Letters*, vol. 94, no. 23, p. 230504, 2005.

[17] A. K. Ekert, "Quantum cryptography and bell's theorem," in *Quantum Measurements in Optics*, pp. 413–418, Springer, 1992.

[18] H.-K. Lo, M. Curty, and B. Qi, "Measurement-device-independent quantum key distribution," *Physical Review Letters*, vol. 108, no. 13, p. 130503, 2012.

[19] C. H. Bennett, G. Brassard, and N. D. Mermin, "Quantum cryptography without bell's theorem," *Physical Review Letters*, vol. 68, no. 5, p. 557, 1992.

[20] Z.-W. Yu, X.-L. Hu, C. Jiang, H. Xu, and X.-B. Wang, "Sending-or-not-sending twin-field quantum key distribution in practice," *Scientific Reports*, vol. 9, no. 1, pp. 1–8, 2019.

[21] C. L. Degen, F. Reinhard, and P. Cappellaro, "Quantum sensing," *Reviews of Modern Physics*, vol. 89, no. 3, p. 035002, 2017.

[22] S. Pirandola, B. R. Bardhan, T. Gehring, C. Weedbrook, and S. Lloyd, "Advances in photonic quantum sensing," *Nature Photonics*, vol. 12, no. 12, pp. 724–733, 2018.

[23] J. C. Howell, R. S. Bennink, S. J. Bentley, and R. W. Boyd, "Realization of the einstein-podolsky-rosen paradox using momentum-and position-entangled photons from spontaneous parametric down conversion," *Physical Review Letters*, vol. 92, no. 21, p. 210403, 2004.

[24] G. Brida, M. Genovese, and I. Ruo Berchera, "Experimental realization of sub-shot-noise quantum imaging," *Nature Photonics*, vol. 4, no. 4, pp. 227–230, 2010.

[25] R. S. Aspden, N. R. Gemmell, P. A. Morris, D. S. Tasca, L. Mertens, M. G. Tanner, R. A. Kirkwood, A. Ruggeri, A. Tosi, R. W. Boyd, *et al.*, "Photon-sparse microscopy: visible light imaging using infrared illumination," *Optica*, vol. 2, no. 12, pp. 1049–1052, 2015.

[26] P. A. Morris, R. S. Aspden, J. E. Bell, R. W. Boyd, and M. J. Padgett, "Imaging with a small number of photons," *Nature Communications*, vol. 6, no. 1, pp. 1–6, 2015.

[27] O. S. Magana-Loaiza, G. A. Howland, M. Malik, J. C. Howell, and R. W. Boyd, "Compressive object tracking using entangled photons," *Applied Physics Letters*, vol. 102, no. 23, p. 231104, 2013.

[28] E. Brambilla, L. Caspani, O. Jedrkiewicz, L. Lugiato, and A. Gatti, "High-sensitivity imaging with multi-mode twin beams," *Physical Review A*, vol. 77, no. 5, p. 053807, 2008.

[29] P.-A. Moreau, E. Toninelli, T. Gregory, and M. J. Padgett, "Ghost imaging using optical correlations," *Laser & Photonics Reviews*, vol. 12, no. 1, p. 1700143, 2018.

[30] A. V. Paterova, H. Yang, Z. S. Toa, and L. A. Krivitsky, "Quantum imaging for the semiconductor industry," *Applied Physics Letters*, vol. 117, no. 5, p. 054004, 2020.

[31] H. Defienne, M. Reichert, J. W. Fleischer, and D. Faccio, "Quantum image distillation," *Science Advances*, vol. 5, no. 10, p. eaax0307, 2019.

[32] G. B. Lemos, V. Borish, G. D. Cole, S. Ramelow, R. Lapkiewicz, and A. Zeilinger, "Quantum imaging with undetected photons," *Nature*, vol. 512, no. 7515, pp. 409–412, 2014.

[33] M. Lahiri, R. Lapkiewicz, G. B. Lemos, and A. Zeilinger, "Theory of quantum imaging with undetected photons," *Physical Review A*, vol. 92, no. 1, p. 013832, 2015.

[34] S. Lloyd, "Enhanced sensitivity of photodetection via quantum illumination," *Science*, vol. 321, no. 5895, pp. 1463–1465, 2008.

[35] S.-H. Tan, B. I. Erkmen, V. Giovannetti, S. Guha, S. Lloyd, L. Maccone, S. Pirandola, and J. H. Shapiro, "Quantum illumination with gaussian states," *Physical Review Letters*, vol. 101, no. 25, p. 253601, 2008.

[36] E. Lopaeva, I. R. Berchera, I. P. Degiovanni, S. Olivares, G. Brida, and M. Genovese, "Experimental realization of quantum illumination," *Physical Review Letters*, vol. 110, no. 15, p. 153603, 2013.

[37] S. Barzanjeh, S. Guha, C. Weedbrook, D. Vitali, J. H. Shapiro, and S. Pirandola, "Microwave quantum illumination," *Physical Review Letters*, vol. 114, no. 8, p. 080503, 2015.

[38] J. H. Shapiro, "The quantum illumination story," *IEEE Aerospace and Electronic Systems Magazine*, vol. 35, no. 4, pp. 8–20, 2020.

[39] E. Toninelli, P.-A. Moreau, T. Gregory, A. Mihalyi, M. Edgar, N. Radwell, and M. Padgett, "Resolution-enhanced quantum imaging by centroid estimation of biphotons," *Optica*, vol. 6, no. 3, pp. 347–353, 2019.

[40] D. Klyshko, "Coherent photon decay in a nonlinear medium," *ZhETF Pisma Redaktsiiu*, vol. 6, p. 490, 1967.

[41] D. C. Burnham and D. L. Weinberg, "Observation of simultaneity in parametric production of optical photon pairs," *Physical Review Letters*, vol. 25, no. 2, p. 84, 1970.

[42] C. Hong and L. Mandel, "Experimental realization of a localized one-photon state," *Physical Review Letters*, vol. 56, no. 1, p. 58, 1986.

[43] P. G. Kwiat, K. Mattle, H. Weinfurter, A. Zeilinger, A. V. Sergienko, and Y. Shih, "New high-intensity source of polarization-entangled photon pairs," *Physical Review Letters*, vol. 75, no. 24, p. 4337, 1995.

[44] R. W. Boyd, *Nonlinear optics*. Academic Press, 2020.

[45] S. Karan, S. Aarav, H. Bharadhwaj, L. Taneja, A. De, G. Kulkarni, N. Meher, and A. K. Jha, "Phase matching in β-barium borate crystals for spontaneous parametric down-conversion," *Journal of Optics*, vol. 22, no. 8, p. 083501, 2020.

[46] J. Leach, R. E. Warburton, D. G. Ireland, F. Izdebski, S. Barnett, A. Yao, G. S. Buller, and M. Padgett, "Quantum correlations in position, momentum, and intermediate bases for a full optical field of view," *Physical Review A*, vol. 85, no. 1, p. 013827, 2012.

[47] O. Aytür and P. Kumar, "Pulsed twin beams of light," *Physical Review Letters*, vol. 65, no. 13, p. 1551, 1990.

[48] E. Brambilla, A. Gatti, M. Bache, and L. A. Lugiato, "Simultaneous near-field and far-field spatial quantum correlations in the high-gain regime of parametric down-conversion," *Physical Review A*, vol. 69, no. 2, p. 023802, 2004.

[49] J. D. Bierlein and H. Vanherzeele, "Potassium titanyl phosphate: properties and new applications," *JOSA B*, vol. 6, no. 4, pp. 622–633, 1989.

[50] M. Okada, K. Takizawa, and S. Ieiri, "Second harmonic generation by periodic laminar structure of nonlinear optical crystal," *Optics Communications*, vol. 18, no. 3, pp. 331–334, 1976.

[51] D. Nikogosyan, "Beta barium borate (bbo) a review of its properties and applications," *Applied Physics A*, vol. 52, pp. 359–368, 1991.

[52] M. M. Fejer, G. Magel, D. H. Jundt, and R. L. Byer, "Quasi-phase-matched second harmonic generation: tuning and tolerances," *IEEE Journal of Quantum Electronics*, vol. 28, no. 11, pp. 2631–2654, 1992.

[53] M. Fiorentino, S. M. Spillane, R. G. Beausoleil, T. D. Roberts, P. Battle, and M. W. Munro, "Spontaneous parametric down-conversion in periodically poled ktp waveguides and bulk crystals," *Optics Express*, vol. 15, no. 12, pp. 7479–7488, 2007.

[54] P. G. Kwiat, E. Waks, A. G. White, I. Appelbaum, and P. H. Eberhard, "Ultrabright source of polarization-entangled photons," *Physical Review A*, vol. 60, no. 2, p. R773, 1999.

[55] C. Van der Poel, J. Bierlein, J. Brown, and S. Colak, "Efficient type i blue second-harmonic generation in periodically segmented ktiopo4 waveguides," *Applied Physics Letters*, vol. 57, no. 20, pp. 2074–2076, 1990.

[56] P. G. Kwiat, K. Mattle, H. Weinfurter, A. Zeilinger, A. V. Sergienko, and Y. Shih, "New high-intensity source of polarization-entangled photon pairs," *Physical Review Letters*, vol. 75, no. 24, p. 4337, 1995.

[57] O. Kuzucu, M. Fiorentino, M. A. Albota, F. N. Wong, and F. X. Kärtner, "Two-photon coincident-frequency entanglement via extended phase matching," *Physical Review Letters*, vol. 94, no. 8, p. 083601, 2005.

[58] Q. Zhang, F. Xu, Y.-A. Chen, C.-Z. Peng, and J.-W. Pan, "Large scale quantum key distribution: challenges and solutions," *Optics Express*, vol. 26, no. 18, pp. 24260–24273, 2018.

[59] X. Ma, C.-H. F. Fung, and H.-K. Lo, "Quantum key distribution with entangled photon sources," *Physical Review A*, vol. 76, no. 1, p. 012307, 2007.

[60] C. H. Bennett, G. Brassard, C. Crépeau, R. Jozsa, A. Peres, and W. K. Wootters, "Teleporting an unknown quantum state via dual classical and einstein-podolsky-rosen channels," *Physical Review Letters*, vol. 70, no. 13, p. 1895, 1993.

[61] R. Raussendorf and H. J. Briegel, "A one-way quantum computer," *Physical Review Letters*, vol. 86, no. 22, p. 5188, 2001.

[62] D. Bouwmeester, J.-W. Pan, K. Mattle, M. Eibl, H. Weinfurter, and A. Zeilinger, "Experimental quantum teleportation," *Nature*, vol. 390, no. 6660, p. 575, 1997.

[63] S.-K. Liao, W.-Q. Cai, W.-Y. Liu, L. Zhang, Y. Li, J.-G. Ren, J. Yin, Q. Shen, Y. Cao, Z.-P. Li, *et al.*, "Satellite-to-ground quantum key distribution," *Nature*, vol. 549, no. 7670, p. 43, 2017.

[64] L. Ji, J. Gao, A.-L. Yang, Z. Feng, X.-F. Lin, Z.-G. Li, and X.-M. Jin, "Towards quantum communications in free-space seawater," *Optics Express*, vol. 25, no. 17, pp. 19795–19806, 2017.

[65] D. K. Oi, A. Ling, G. Vallone, P. Villoresi, S. Greenland, E. Kerr, M. Macdonald, H. Weinfurter, H. Kuiper, E. Charbon, *et al.*, "Cubesat quantum communications mission," *EPJ Quantum Technology*, vol. 4, no. 1, p. 6, 2017.

[66] Z. Tang, R. Chandrasekara, Y. C. Tan, C. Cheng, K. Durak, and A. Ling, "The photon pair source that survived a rocket explosion," *Scientific Reports*, vol. 6, p. 25603, 2016.

[67] K. Durak, A. Villar, B. Septriani, Z. Tang, R. Chandrasekara, R. Bedington, and A. Ling, "The next iteration of the small photon entangling quantum system (speqs-2.0)," in *Advances in Photonics of Quantum Computing, Memory, and Communication IX*, vol. 9762, p. 976209, International Society for Optics and Photonics, 2016.

[68] A. Lohrmann, A. Villar, A. Stolk, and A. Ling, "High fidelity field stop collection for polarization-entangled photon pair sources," *Applied Physics Letters*, vol. 113, no. 17, p. 171109, 2018.

[69] A. Anwar, P. Chithrabhanu, S. G. Reddy, N. Lal, and R. Singh, "Selecting the pre-detection characteristics for fiber coupling of parametric down-converted biphoton modes," *Optics Communications*, vol. 382, pp. 219–224, 2017.

[70] D. Kleinman, "Theory of optical parametric noise," *Physical Review*, vol. 174, no. 3, p. 1027, 1968.

[71] D. Ljunggren and M. Tengner, "Optimal focusing for maximal collection of entangled narrow-band photon pairs into single-mode fibers," *Physical Review A*, vol. 72, no. 6, p. 062301, 2005.

[72] H. D. L. Pires, F. Coppens, and M. Van Exter, "Type-i spontaneous parametric down-conversion with a strongly focused pump," *Physical Review A*, vol. 83, no. 3, p. 033837, 2011.

[73] R. Ramirez-Alarcon, H. Cruz-Ramirez, and A. B. U'Ren, "Effects of crystal length on the angular spectrum of spontaneous parametric downconversion photon pairs," *Laser Physics*, vol. 23, no. 5, p. 055204, 2013.

[74] B. Septriani, J. A. Grieve, K. Durak, and A. Ling, "Thick-crystal regime in photon pair sources," *Optica*, vol. 3, no. 3, pp. 347–350, 2016.

[75] P. Trojek, *Efficient generation of photonic entanglement and multiparty quantum communication*. PhD thesis, lmu, 2007.

[76] F. Steinlechner, P. Trojek, M. Jofre, H. Weier, D. Perez, T. Jennewein, R. Ursin, J. Rarity, M. W. Mitchell, J. P. Torres, *et al.*, "A high-brightness source of polarization-entangled photons optimized for applications in free space," *Optics Express*, vol. 20, no. 9, pp. 9640–9649, 2012.

[77] H. Kuniyil and K. Durak, "Efficient coupling of down-converted photon pairs into single mode fiber," *Optics Communications*, vol. 493, p. 127038, 2021.

[78] I. R. Berchera and I. P. Degiovanni, "Quantum imaging with sub-poissonian light: challenges and perspectives in optical metrology," *Metrologia*, vol. 56, no. 2, p. 024001, 2019.

[79] J. P. Dowling and G. J. Milburn, "Quantum technology: the second quantum revolution," *Philosophical Transactions of the Royal Society of London. Series A: Mathematical, Physical and Engineering Sciences*, vol. 361, no. 1809, pp. 1655–1674, 2003.

[80] A. Acin, N. Gisin, and L. Masanes, "From bell's theorem to secure quantum key distribution," *Physical Review Letters*, vol. 97, no. 12, p. 120405, 2006.

[81] A. Steane, "Quantum computing," *Reports on Progress in Physics*, vol. 61, no. 2, p. 117, 1998.

[82] J. Preskill, "Quantum computing in the nisq era and beyond," *Quantum*, vol. 2, p. 79, 2018.

[83] S. M. Kolenderska, F. Vanholsbeeck, and P. Kolenderski, "Quantum-inspired detection for spectral domain optical coherence tomography," *Optics Letters*, vol. 45, no. 13, pp. 3443–3446, 2020.

[84] Z. Zhang, S. Mouradian, F. N. Wong, and J. H. Shapiro, "Entanglement-enhanced sensing in a lossy and noisy environment," *Physical Review Letters*, vol. 114, no. 11, p. 110506, 2015.

[85] D. Luong, C. S. Chang, A. Vadiraj, A. Damini, C. M. Wilson, and B. Balaji, "Receiver operating characteristics for a prototype quantum two-mode squeezing radar," *IEEE Transactions on Aerospace and Electronic Systems*, vol. 56, no. 3, pp. 2041–2060, 2019.

[86] A. G. White, J. R. Mitchell, O. Nairz, and P. G. Kwiat, ""interaction-free" imaging," *Physical Review A*, vol. 58, no. 1, p. 605, 1998.

[87] Q. Zhuang, Z. Zhang, and J. H. Shapiro, "Quantum illumination for enhanced detection of rayleigh-fading targets," *Physical Review A*, vol. 96, no. 2, p. 020302, 2017.

[88] D. G. England, B. Balaji, and B. J. Sussman, "Quantum-enhanced standoff detection using correlated photon pairs," *Physical Review A*, vol. 99, no. 2, p. 023828, 2019.

[89] H. Liu, B. Balaji, and A. S. Helmy, "Target detection aided by quantum temporal correlations: Theoretical analysis and experimental validation," *IEEE Transactions on Aerospace and Electronic Systems*, vol. 56, no. 5, pp. 3529–3544, 2020.

[90] H. Kuniyil, N. Jam, and K. Durak, "Object ranging and sensing by temporal cross-correlation measurement," in *SPIE Future Sensing Technologies*, vol. 11525, pp. 150–156, SPIE, 2020.

[91] K. Durak, N. Jam, and C. Dindar, "Object tracking and identification by quantum radar," in *Quantum Technologies and Quantum Information Science V*, vol. 11167, pp. 41–49, SPIE, 2019.

[92] B. Srivathsan, G. K. Gulati, B. Chng, G. Maslennikov, D. Matsukevich, and C. Kurtsiefer, "Narrow band source of transform-limited photon pairs via four-wave mixing in a cold atomic ensemble," *Physical Review Letters*, vol. 111, no. 12, p. 123602, 2013.

[93] D. Tasca, R. Gomes, F. Toscano, P. S. Ribeiro, and S. Walborn, "Continuous-variable quantum computation with spatial degrees of freedom of photons," *Physical Review A*, vol. 83, no. 5, p. 052325, 2011.

[94] J. Leach, B. Jack, J. Romero, A. K. Jha, A. M. Yao, S. Franke-Arnold, D. G. Ireland, R. W. Boyd, S. M. Barnett, and M. J. Padgett, "Quantum correlations in optical angle–orbital angular momentum variables," *Science*, vol. 329, no. 5992, pp. 662–665, 2010.

[95] J. Leach, B. Jack, J. Romero, M. Ritsch-Marte, R. Boyd, A. Jha, S. Barnett, S. Franke-Arnold, and M. Padgett, "Violation of a bell inequality in two-dimensional orbital angular momentum state-spaces," *Optics Express*, vol. 17, no. 10, pp. 8287–8293, 2009.

[96] O. Jedrkiewicz, Y.-K. Jiang, E. Brambilla, A. Gatti, M. Bache, L. Lugiato, and P. Di Trapani, "Detection of sub-shot-noise spatial correlation in high-gain parametric down conversion," *Physical Review Letters*, vol. 93, no. 24, p. 243601, 2004.

[97] M. J. Padgett and R. W. Boyd, "An introduction to ghost imaging: quantum and classical," *Philosophical Transactions of the Royal Society A: Mathematical, Physical and Engineering Sciences*, vol. 375, no. 2099, p. 20160233, 2017.

[98] M. P. Edgar, D. S. Tasca, F. Izdebski, R. E. Warburton, J. Leach, M. Agnew, G. S. Buller, R. W. Boyd, and M. J. Padgett, "Imaging high-dimensional spatial entanglement with a camera," *Nature Communications*, vol. 3, no. 1, pp. 1–6, 2012.

[99] H. Defienne, M. Reichert, and J. W. Fleischer, "General model of photon-pair detection with an image sensor," *Physical Review Letters*, vol. 120, no. 20, p. 203604, 2018.

[100] S. W. Hell and J. Wichmann, "Breaking the diffraction resolution limit by stimulated emission: stimulated-emission-depletion fluorescence microscopy," *Optics Letters*, vol. 19, no. 11, pp. 780–782, 1994.

[101] S. T. Hess, T. P. Girirajan, and M. D. Mason, "Ultra-high resolution imaging by fluorescence photoactivation localization microscopy," *Biophysical Journal*, vol. 91, no. 11, pp. 4258–4272, 2006.

[102] E. Betzig, G. H. Patterson, R. Sougrat, O. W. Lindwasser, S. Olenych, J. S. Bonifacino, M. W. Davidson, J. Lippincott-Schwartz, and H. F. Hess, "Imaging intracellular fluorescent proteins at nanometer resolution," *Science*, vol. 313, no. 5793, pp. 1642–1645, 2006.

[103] M. Tsang, R. Nair, and X.-M. Lu, "Quantum theory of superresolution for two incoherent optical point sources," *Physical Review X*, vol. 6, no. 3, p. 031033, 2016.

[104] W.-K. Tham, H. Ferretti, and A. M. Steinberg, "Beating rayleigh's curse by imaging using phase information," *Physical Review Letters*, vol. 118, no. 7, p. 070801, 2017.

[105] Z. S. Tang, K. Durak, and A. Ling, "Fault-tolerant and finite-error localization for point emitters within the diffraction limit," *Optics Express*, vol. 24, no. 19, pp. 22004–22012, 2016.

[106] V. Giovannetti, S. Lloyd, and L. Maccone, "Quantum-enhanced measurements: beating the standard quantum limit," *Science*, vol. 306, no. 5700, pp. 1330–1336, 2004.

[107] V. Giovannetti, S. Lloyd, and L. Maccone, "Advances in quantum metrology," *Nature Photonics*, vol. 5, no. 4, pp. 222–229, 2011.

[108] M. W. Mitchell, J. S. Lundeen, and A. M. Steinberg, "Super-resolving phase measurements with a multiphoton entangled state," *Nature*, vol. 429, no. 6988, pp. 161–164, 2004.

[109] Z. Ou, "Fundamental quantum limit in precision phase measurement," *Physical Review A*, vol. 55, no. 4, p. 2598, 1997.

[110] M. Unternährer, B. Bessire, L. Gasparini, M. Perenzoni, and A. Stefanov, "Super-resolution quantum imaging at the heisenberg limit," *Optica*, vol. 5, no. 9, pp. 1150–1154, 2018.

[111] C. H. Monken, P. S. Ribeiro, and S. Pádua, "Transfer of angular spectrum and image formation in spontaneous parametric down-conversion," *Physical Review A*, vol. 57, no. 4, p. 3123, 1998.

[112] B. Mollow, "Photon correlations in the parametric frequency splitting of light," *Physical Review A*, vol. 8, no. 5, p. 2684, 1973.

[113] C.-K. Hong, Z.-Y. Ou, and L. Mandel, "Measurement of subpicosecond time intervals between two photons by interference," *Physical Review Letters*, vol. 59, no. 18, p. 2044, 1987.

[114] D. Klyshko, "Use of two-photon light for absolute calibration of photoelectric detectors," *Soviet Journal of Quantum Electronics*, vol. 10, no. 9, p. 1112, 1980.

[115] P. E. Powers and J. W. Haus, *"Fundamentals of Nonlinear Optics"*. CRC Press, 2017.

[116] M. O. Scully and M. S. Zubairy, "Quantum optics," 1999.

[117] L. Mandel and E. Wolf, *Optical coherence and quantum optics*. Cambridge university press, 1995.

[118] W. H. Louisell, *Coupled mode and parametric electronics*. Wiley, 1960.

[119] W. Louisell, A. Yariv, and A. Siegman, "Quantum fluctuations and noise in parametric processes. i.," *Physical Review*, vol. 124, no. 6, p. 1646, 1961.

[120] X. Zou, L. Wang, and L. Mandel, "Violation of classical probability in parametric down-conversion," *Optics Communications*, vol. 84, no. 5-6, pp. 351–354, 1991.

[121] A. Kuzmich, W. Bowen, A. Boozer, A. Boca, C. Chou, L.-M. Duan, and H. Kimble, "Generation of nonclassical photon pairs for scalable quantum communication with atomic ensembles," *Nature*, vol. 423, no. 6941, pp. 731–734, 2003.

[122] Z. Ou, L. Wang, and L. Mandel, "Vacuum effects on interference in two-photon down conversion," *Physical Review A*, vol. 40, no. 3, p. 1428, 1989.

[123] S.-M. F. Nee, "Ellipsometric view on reflection and scattering from optical blacks," *Applied Optics*, vol. 31, no. 10, pp. 1549–1556, 1992.

[124] S.-M. F. Nee, "Polarization of specular reflection and near-specular scattering by a rough surface," *Applied Optics*, vol. 35, no. 19, pp. 3570–3582, 1996.

[125] R. Hanbury and R. Twiss, "A new type of interferometer for use in radio astronomy," *Phil. Mag.*, vol. 45, no. 7, pp. 663–682, 1954.

[126] R. Brown and R. Q. Twiss, "Correlation between photons in two coherent beams of light," *Nature*, vol. 177, no. 4497, pp. 27–29, 1956.

[127] M. Förtsch, G. Schunk, J. U. Fürst, D. Strekalov, T. Gerrits, M. J. Stevens, F. Sedlmeir, H. G. Schwefel, S. W. Nam, G. Leuchs, *et al.*, "Highly efficient generation of single-mode photon pairs from a crystalline whispering-gallery-mode resonator source," *Physical Review A*, vol. 91, no. 2, p. 023812, 2015.

[128] X. Guo, C.-l. Zou, C. Schuck, H. Jung, R. Cheng, and H. X. Tang, "Parametric down-conversion photon-pair source on a nanophotonic chip," *Light: Science & Applications*, vol. 6, no. 5, pp. e16249–e16249, 2017.

[129] Y.-S. Lee, S. M. Lee, H. Kim, and H. S. Moon, "Highly bright photon-pair generation in doppler-broadened ladder-type atomic system," *Optics Express*, vol. 24, no. 24, pp. 28083–28091, 2016.

[130] S. Frick, A. McMillan, and J. Rarity, "Quantum rangefinding," *Optics Express*, vol. 28, no. 25, pp. 37118–37128, 2020.

[131] J. A. Grieve, R. Chandrasekara, Z. Tang, C. Cheng, and A. Ling, "Correcting for accidental correlations in saturated avalanche photodiodes," *Optics Express*, vol. 24, no. 4, pp. 3592–3600, 2016.

[132] A. Bhattacharjee, M. K. Joshi, S. Karan, J. Leach, and A. K. Jha, "Propagation-induced revival of entanglement in the angle-oam bases," *Science Advances*, vol. 8, no. 31, p. eabn7876, 2022.

[133] D. Tasca, S. Walborn, P. S. Ribeiro, F. Toscano, and P. Pellat-Finet, "Propagation of transverse intensity correlations of a two-photon state," *Physical Review A*, vol. 79, no. 3, p. 033801, 2009.

[134] C. Law and J. Eberly, "Analysis and interpretation of high transverse entanglement in optical parametric down conversion," *Physical Review Letters*, vol. 92, no. 12, p. 127903, 2004.

[135] K. Chan, J. Torres, and J. Eberly, "Transverse entanglement migration in hilbert space," *Physical Review A*, vol. 75, no. 5, p. 050101, 2007.

[136] L. Rayleigh, "Xxxi. investigations in optics, with special reference to the spectroscope," *The London, Edinburgh, and Dublin Philosophical Magazine and Journal of Science*, vol. 8, no. 49, pp. 261–274, 1879.

[137] T. L. Sellaro, R. Filkins, C. Hoffman, J. L. Fine, J. Ho, A. V. Parwani, L. Pantanowitz, and M. Montalto, "Relationship between magnification and resolution in digital pathology systems," *Journal of Pathology Informatics*, vol. 4, no. 1, p. 21, 2013.

VITA

Hashir Puthiyapurayil Kuniyil completed his MSc degree in 2013 from Manipal University, Manipal India, and the MSc thesis work was carried out at the Indian Institute of Technology Gandhi Nagar (IITGn), India. His MSc thesis focused on Tunable Diode Laser Absorption Spectroscopy (TDLAS), investigating a gas sample under various environmental conditions in a laboratory setting. Prior to his enrollment at Ozyegin University, Kuniyil contributed to the Defense Research and Development Organization (DRDO) India's project at the Indian Institute of Technology Madras (IITM), Chennai, India, playing a vital role in establishing an Afterburner Combustor for jet engine applications. In September 2018, he began pursuing his PhD at Ozyegin University.